Faculté des bioingénieurs

Soil Moisture Estimation: A Comparative Analysis of Remote Sensing Methods Using Ground Penetrating Radar

Auteur : Yan Cesar Lima Ferro De Paoli

Promoteur : Sébastien Lambot
Co-promoteur : Matthieu Taymans

Lecteurs : Pierre Defourny
Daniel Spengler

Année Académique : 2023 – 2024

Mémoire de fin d'études présenté en vue de l'obtention du diplôme de Master SAIV – MSc Erasmus+ GEM : Geo-information Science and Earth Observation for Environmental Modelling and Management

Acknowledgment

First and foremost, I would like to express my deepest gratitude to my spiritual guides, for their unwavering support, guidance, and encouragement throughout my entire life.

I am profoundly grateful to my supervisor, Professor Sébastien Lambot, and my co-supervisor, Matthieu Taymans, for their invaluable support throughout this thesis. Professor Lambot, your insights and expertise have been instrumental in shaping my research. Matthieu Taymans, as my former boss and now a life-guide and friend, your support and constant encouragement have been indispensable, especially over the last year, and your patience and understanding have been a constant source of reassurance.

I would also like to extend my sincere thanks to Professor Pierre Defourny for hosting and guiding me during my stay at UCLouvain. Your mentorship has greatly enriched my academic experience, and I am deeply appreciative of the opportunities you have provided.

I am immensely grateful to my colleagues and friends, either in person or virtually, who have provided moral support, advice, and motivation during challenging times. Your camaraderie and shared experiences have made this journey much more enjoyable and rewarding.

I would like to thank Erasmus Mundus Joint Masters scholarship for hosting me conducting my master's under the GEM program. I am grateful to my current institution 'UCLouvain' and my former educational institution 'Lund University' for providing the foundation in geo-informatics, including GIS/geospatial analysis, remote sensing, and ecosystem modelling and dynamic process-based spatial models. Additionally, I would like to extend my sincere thanks to constellr for their teachings, the opportunities given, and all the support from the team.

My heartfelt thanks go to my parents and sister for their endless love, patience, and encouragement. Despite not being physically present with me during my studies abroad, their love, understanding, and unwavering support have been my constant motivation.

Finally, to Luiza, my partner. Thank you for your love, patience, and unwavering belief in me. Your support has been my anchor during the most challenging times of this journey, and together I am sure that we can overcome anything.

This thesis is dedicated to all those who have supported me, directly or indirectly, throughout this incredible journey. I am deeply grateful for your presence in my life

Table of Contents

List of Figures i

List of Tables vii

List of Acronyms vii

1 Introduction 1

2 Literature Review 3

2.1 Fundamentals of Soil Moisture Estimation 3

2.2 Soil Moisture Estimation Using Ground Penetrating Radar Data 6

2.3 Soil Moisture Estimation Using SAR Data 8

2.3.1 Synergetic Techniques 9

2.3.2 Polarimetric Scattering Power Decomposition 10

2.3.3 Data-driven 11

2.3.4 Change Detection 13

2.4 Soil Moisture Estimation Using Optical/thermal Data 14

2.4.1 Temperature-Vegetation Dryness Index 16

3 Research Objectives 18

4 Materials 19

4.1 Study Area 19

4.1.1 Geographical Location 19

4.1.2 Land Use and Land Cover 22

4.1.3 Socio-Economic Context 24

4.1.4 Agricultural practices on the field 25

4.2 Data Sources 26

4.2.1 Meteorological field measurements 26

4.2.2 GPR Data 26

4.2.3 Sentinel-1 Ground Range Detected Data 27
4.2.4 Landsat 9 Collection Data 28
5 Methods 29
5.1 Data Preprocessing 30
5.1.1 Meteorological Field Measurements Data Preparation 30
5.1.2 GPR Data Preparation 31
5.1.3 Grid Definition 31
5.1.4 Sentinel-1 Data Preparation 32
5.1.5 Landsat 9 Data Preparation 33
5.2 SAR-based Change Detection 35
5.2.1 Radar Vegetation Index 36
5.2.2 Soil Moisture Estimation 37
5.3 Temperature-Vegetation Dryness Index (TVDI) 40
5.3.1 Standard TVDI 40
5.3.2 Temporal TVDI Modifications 42
5.4 Qualitative Analysis 44
6 Results 45
6.1 Preliminary Results 45
6.1.1 Radar Vegetation index 45
6.1.2 SAR-based change detection - Dry edge 47
6.1.3 SAR-based wet edge definition 48
6.1.4 TVDI: LST-NDVI triangle space 49
6.1.5 Temporal TVDI: LST-NDVI triangle space 52
6.2 Main Results 55
6.2.1 Temporal variability 56

6.2.2 Spatial variability ... 61
7 Discussion ... 67
7.1 Key Findings ... 67
7.2 In-depth Event Analysis ... 70
7.3 Comparison with previous studies ... 72
7.4 Practical implications ... 73
7.5 Limitations ... 75
7.6 Future research directions ... 76
8 Conclusion ... 77
References ... 78
Appendix ... 87

List of Figures

Figure 1: Location of the Grand Villers field within La Bruyère municipality, Belgium. The image highlights the Grand Villers field (solid red area) situated within the La Bruyère municipality (yellow boundary). The inset map provides a broader geographical context, showing the position of La Bruyère municipality within Belgium. 20

Figure 2: Elevation maps of the study area and La Bruyère municipality. (a) Detailed elevation map of the Grand Villers field (indicated by the red rectangle) with elevation values ranging from 174 to 186 meters. (b) Broader elevation map of the municipality with elevation values ranging from 0 to 300 meters.Data obtained from Wallonia Geoportal. 22

Figure 3: Soil maps of the study area and La Bruyère municipality. On the left there is a zoomed in soil map of the Grand Villers field (indicated by the red rectangle) containing loamy soils with different capacity of natural drainage. On the right there is a broader soil map of the municipality (indicated by the yellow boundary) with different types of soil. Data obtained from Wallonia Geoportal.. 24

Figure 4: AOI mean temperature over time from December 2021 to January 2024. The graph shows daily mean temperature measurements (°C). The data points are marked in red, indicating the fluctuation in temperatures over time. Data obtained from Senscrop. 30

Figure 5: Precipitation over time from December 2021 to January 2024. The bar chart illustrates daily precipitation (mm). The data points, represented as vertical blue bars, show variability in precipitation levels. Data obtained from Senscrop. 31

Figure 6: Sentinel-1 Data Preparation Workflow. The figure illustrates the main steps involved in preparing Sentinel-1 GRD time-series data for analysis. The process includes setting the date range, selecting IW mode, choosing specific bands, masking invalid pixels, applying a speckle filter, and calculating indices. 32

Figure 7: Landsat 8/9 Data Preparation Workflow. This figure outlines the primary steps in processing Landsat 8/9 time-series data. The process includes setting the date range, applying

cloud masking, selecting bands, masking invalid pixels, applying a sharpening algorithm, and calculating indices. 33

Figure 8: SAR-based Soil Moisture Estimation Workflow. The flowchart illustrates the steps used to generate soil moisture maps, beginning with the calculation of σ°VV, σ°VH, cross-ratio, and DpRVIc. The process involves defining dry and wet edges, applying inverse modeling, and validating DpRVIc using the cross-ratio as an auxiliary step. 36

Figure 9: Relationship Between Vegetation Index and Changes in Co-Pol Backscatter. This diagram illustrates the relationship between the vegetation index and changes in co-polarized (co-pol) backscatter (Δσ°vv) for different ground conditions. The triangle is divided into three zones: Bare Soil, Partial Cover, and Full Cover. The vertical axis represents changes in co-pol backscatter, ranging from the wilting point to field capacity, while the horizontal axis represents the vegetation index, from the dry reference (low vegetation index) to the wet reference (high vegetation index). The gradient shading from brown to green indicates increasing vegetation cover, with corresponding changes in backscatter values. Adapted from Bhogapurapu et al. (2022). 39

Figure 10: Relationship Between NDVI and LST with Evaporation and Transpiration Extremes. This diagram shows the relationship between the Normalized Difference Vegetation Index (NDVI) and Land Surface Temperature (LST) for different vegetation covers. The triangular area is divided into three zones: Bare Soil, Partial Cover, and Full Cover. The vertical axis represents LST, with the left side indicating evaporation (from no evaporation to maximum evaporation), while the horizontal axis represents NDVI, indicating transpiration (from maximum transpiration to no transpiration). The dry reference is indicated by a red dashed line, and the wet reference by a blue dashed line. The gradient shading illustrates changes in cover and associated evapotranspiration processes. Adapted from Sandholt et al., 2002. 41

Figure 11: TVDI Methodology Workflow. The workflow begins with NDVI and LST time-series data, followed by the construction of the LST-NDVI triangle. It then defines the wet and dry edges, extracts the LST minimum value and the a,b parameters, and culminates in the calculation of TVDI to produce TVDI maps. 42

Figure 12: Cross-ratio visualization in comparison to backscatter signals from 2019 to 2023, mean representation for all pixels in the AOI. 46

Figure 13: Cross-Ratio visualization in comparison to $DpRVI_c$ from 2019 to 2023, mean representation for all pixels in the AOI. 46

Figure 14: Mean representation of the dry signal from 2019 to 2023 for all pixels within the AOI. 47

Figure 15: Relationship Between Differential Polarimetric Vegetation Index (DpRVIc) and Changes in Co-Pol Backscatter (Δσ°vv). The scatter plot shows the relationship between DpRVIc and changes in co-polarized (co-pol) backscatter (Δσ°vv). Blue dots represent the general dataset, while red dots highlight the upper 2% of the data points. The black curve represents the quadratic regression model fitted to the red dots. 48

Figure 16:LST-NDVI triangle space for four different dates. Data points are represented by grey circles. The maximum values used to create the dry edge are represented by red small triangles. 50

Figure 17: Relationship Between NDVI and Temperature Difference (LST - Air Temperature) Over Time. This scatter plot illustrates the relationship between the Normalized Difference Vegetation Index (NDVI) and the temperature difference (Land Surface Temperature (LST) minus Air Temperature) across various months from February 2022 to September 2023. Each color represents data from a different month, as indicated in the legend. The data points show seasonal variations, with higher NDVI values generally associated with lower temperature differences, indicating the influence of vegetation cover on temperature regulation. 52

Figure 18: Relationship Between NDVI and Temperature Difference (LST - Air Temperature) with Dry and Wet Edges. This scatter plot depicts the relationship between the NDVI and the temperature difference in degrees Celsius. The light blue dots represent all data points, while the red and blue dots highlight the upper 2% and lower 2% of the data, respectively. The red dashed line represents the dry edge, showing the upper boundary of the data, and the blue dashed line represents the wet edge, showing the lower boundary. These edges illustrate the extremes of temperature differences associated with varying levels of vegetation cover. 54

Figure 19: Comparative time series of precipitation, SAR-based soil moisture, and tTVDI. This multi-variable time series graph displays field precipitation (mm) in blue, SAR-based soil moisture median estimation (m^3/m^3) in green, and the median tTVDI in orange from January 2022 to January 2024. The precipitation data shows the daily rainfall events, while the SAR estimation indicates

the field-median volumetric soil moisture, and the tTVDI values reflect the dryness of vegetation. The interplay between these variables highlights the impact of precipitation on soil moisture levels and vegetation dryness over time. 56

Figure 20: Comparative time series of irrigation, precipitation, SAR and GPR-based soil moisture, and tTVDI. This multi-variable time series graph displays data from August 17, 2023, to October 2, 2023. The graph includes irrigation events (blue crosses), precipitation (mm) shown as blue bars, field-median soil moisture estimated by GPR for the top 40 cm of soil (m^3/m^3) shown in red, field-median soil moisture estimated by SAR (m^3/m^3) shown in green, and the tTVDI shown in orange. The left y-axis represents precipitation, while the right y-axis represents soil moisture estimations and tTVDI. 59

Figure 21: Comparison of soil moisture estimations between (a) GPR-based results and (b) SAR-based results, at 20-meter spatial resolution on August 25, 2023. Panel (a) shows volumetric soil moisture estimations obtained using GPR after aggregation to a spatial resolution of 20 meters. The color scale ranges from 0.3 to 0.4. Panel (b) shows volumetric soil moisture estimations obtained using SAR data at a spatial resolution of 20 meters. The color scale ranges from 0 (dry) to 1 (saturated). 62

Figure 22: Comparison of soil moisture estimations between (a) GPR-based results and (b) SAR-based results, at 20-meter spatial resolution on September 11, 2023. Panel (a) shows volumetric soil moisture estimations obtained using GPR after aggregation to a spatial resolution of 20 meters. The color scale ranges from 0.15 to 0.3. Panel (b) shows volumetric soil moisture estimations obtained using SAR data at a spatial resolution of 20 meters, with values from 0.2 to 0.8. 63

Figure 23: Comparison of soil moisture estimations assessment (a) GPR-based results and (b) TVDI results, at 30-meter spatial resolution on September 11, 2023. Panel (a) shows volumetric soil moisture estimations obtained using GPR after aggregation to a spatial resolution of 30 meters. The color scale ranges from 0.15 to 0.3. Panel (b) shows TVDI values obtained using optical/thermal data at a spatial resolution of 30 meters, with values from 0 to 1. 65

Figure 24: Comparison of soil moisture estimations assessment (a) SAR-based results and (b) TVDI results, at 30-meter spatial resolution on September 11, 2023. Panel (a) shows volumetric soil moisture estimations obtained using SAR data at a spatial resolution of 30 meters, with values

ranging from 0 to 0.8. Panel (b) shows TVDI values obtained using optical/thermal data at a spatial resolution of 30 meters, with values from 0 to 1. 66

Figure 25: Time series of median NDVI from March 2022 to September 2023. The graph presents the median NDVI values over time, from March 2022 to September 2023. The green line with circular markers shows the temporal variation in NDVI, indicating changes in vegetation health and density. Peaks in the graph correspond to periods of higher vegetation activity, while troughs indicate lower vegetation activity. 87

Figure 26: Time series of SAR-based soil moisture median estimation from May 2023 to September 2023. The graph shows the volumetric field-median soil moisture estimation obtained using SAR from May 2023 to September 2023. The green line indicates the temporal variation in soil moisture levels, highlighting fluctuations and trends over the period. Notable peaks and troughs reflect changes in soil moisture conditions influenced by environmental factors. 88

Figure 27: Time series of median tTVDI from April 2023 to September 2023. The graph presents the median tTVDI values over time, from April 2023 to September 2023. The orange line shows the temporal variation in tTVDI, indicating changes in vegetation dryness. Peaks in the graph correspond to periods of higher dryness, while troughs indicate periods of lower dryness. 89

Figure 28: GPR-based soil moisture estimation obtained with kriging interpolation results and at 1.3-meter spatial resolution on August 22, 2023. The map shows volumetric soil moisture estimations created by UCLouvain GPR team. The color scale ranges from 0 to 0.3................. 90

Figure 29: GPR-based soil moisture estimation obtained with kriging interpolation results and at 1.3-meter spatial resolution on August 25, 2023. The map shows volumetric soil moisture estimations created by UCLouvain GPR team. The color scale ranges from 0 to 0.44................ 91

Figure 30: GPR-based soil moisture estimation obtained with kriging interpolation results and at 1.3-meter spatial resolution on August 29, 2023. The map shows volumetric soil moisture estimations created by UCLouvain GPR team. The color scale ranges from 0 to 0.45................ 92

Figure 31: GPR-based soil moisture estimation obtained with kriging interpolation results and at 1.3-meter spatial resolution on September 05, 2023. The map shows volumetric soil moisture estimations created by UCLouvain GPR team. The color scale ranges from 0 to 0.44................ 93

Figure 32: GPR-based soil moisture estimation obtained with kriging interpolation results and at 1.3-meter spatial resolution on September 08, 2023. The map shows volumetric soil moisture estimations created by UCLouvain GPR team. The color scale ranges from 0 to 0.45................ 94
Figure 33: GPR-based soil moisture estimation obtained with kriging interpolation results and at 1.3-meter spatial resolution on September 11, 2023. The map shows volumetric soil moisture estimations created by UCLouvain GPR team. The color scale ranges from 0 to 0.40................ 95
Figure 34: GPR-based soil moisture estimation obtained with kriging interpolation results and at 1.3-meter spatial resolution on September 15, 2023. The map shows volumetric soil moisture estimations created by UCLouvain GPR team. The color scale ranges from 0 to 0.42................ 96
Figure 35: GPR-based soil moisture estimation obtained with kriging interpolation results and at 1.3-meter spatial resolution on September 20, 2023. The map shows volumetric soil moisture estimations created by UCLouvain GPR team. The color scale ranges from 0 to 0.44................ 97

List of Tables

Table 1: Sentinel-1 GRD data specifications for Interferometric Wide Swath (IW), Extra Wide Swath (EW), and Strip Map (SM) modes, with HH (Horizontal-Horizontal), HV (Horizontal-Vertical), VV (Vertical-Vertical), and VH (Vertical-Horizontal) indicating radar polarization (Source: ESA, 2024) 28

Table 2: Spectral band specifications for Landsat-9, including band edges, center wavelengths, and spatial resolution at nadir (Source: NASA Landsat Science, 2024) 29

List of Acronyms

ANN - Artificial Neural Networks

AOI – Area of Interest

API - Application Programming Interface

BT - Brightness Temperature

CD – Change Detection

CRP - Cross-Ratio Parameter

DEM - Digital Elevation Model

DpRVIc - Dual-pol Radar Vegetation Index

GPR - Ground Penetrating Radar

GRD - Ground Range Detected

GRDSAR - Ground Range Detected SAR

IW - Interferometric Wide Swath

LAS - Large Aperture Scintillometer

LST - Land Surface Temperature

LULC - Land Use/Land Cover

NASA - National Aeronautics and Space Administration

NDVI - Normalized Difference Vegetation Index

NDWI - Normalized Difference Water Index

OFAW - Organisation des Forets et des Aires naturelles de Wallonie

RFR - Random Forest Regression

SAR - Synthetic Aperture Radar

SPW - Service Public de Wallonie

SR - Surface Reflectance

SVAT - Soil-Vegetation-Atmosphere-Transfer

SVR - Support Vector Regression

TOA - Top of Atmosphere

TOAR - Top of Atmosphere Reflectance

TVDI - Temperature-Vegetation Dryness Index

tTVDI – Temporal Temperature-Vegetation Dryness Index

USGS - United States Geological Survey

VH - Vertical Transmit Horizontal Receive

VV - Vertical Transmit Vertical Receive

1 Introduction

Soil moisture is a critical variable in the hydrological cycle, affecting plant growth, weather patterns, and climate systems (Karthikeyan et al., 2017; Pauwels and De Lannoy, 2006; Seneviratne et al., 2010). Soil moisture refers to the amount of water contained within the soil's unsaturated zone, typically measured as a volumetric or gravimetric ratio (Al-Yaari et al., 2014). It plays a pivotal role in determining the soil's ability to support vegetation, manage water resources, and interact with the atmosphere. Accurate soil moisture estimation is essential for optimizing agricultural productivity, managing water resources, and predicting climatic conditions (Karthikeyan et al., 2020; Massari et al., 2018; Scipal et al., 2008).

Traditional in-situ methods of measuring soil moisture, while accurate at small scales, are labor-intensive and limited in spatial coverage (Lekshmi et al., 2014). Consequently, remote sensing technologies have emerged as powerful tools for estimating soil moisture over large areas and varying environmental conditions. In regions like Wallonia in Belgium, where the landscape features a complex mix of soil types with different natural drainage and vegetation cover, the need for reliable and accurate soil moisture data is particularly acute (Wallonie Service Public SPW, 2023). Such variability poses significant challenges for both agricultural management and environmental monitoring, highlighting the importance of advanced remote sensing techniques.

The journey of remote sensing for soil moisture estimation began with satellite missions like National Aeronautics and Space Administration (NASA)'s Landsat in the 1970s, which primarily relied on optical imagery. These early missions provided valuable data but were limited by their dependence on clear skies and daylight conditions. Over the years, advancements in microwave sensing, particularly with the launch of the Soil Moisture and Ocean Salinity (SMOS) satellite in 2009 and NASA's Soil Moisture Active Passive (SMAP) mission in 2015, have revolutionized our ability to measure soil moisture from space. These missions have enabled continuous, global data collection, significantly improving the accuracy and temporal resolution of soil moisture estimates across diverse landscapes (Entekhabi et al., 2010).

Today, a variety of remote sensing techniques have been developed to improve the accuracy and efficiency of soil moisture estimation. These include microwave-based methods, such as Synthetic

Aperture Radar (SAR) (Bauer-Marschallinger et al., 2018) and Ground Penetrating Radar (GPR) (Klotzsche et al., 2018), as well as optical and thermal remote sensing approaches (Zhang and Zhou, 2016). Each of these methods offers unique advantages and faces specific challenges, particularly in accounting for factors like vegetation cover, surface roughness, and atmospheric conditions (Jagdhuber et al., 2012). The integration of data from multiple sensors, including optical and thermal, remains a critical area for improving estimation accuracy across different scales and conditions (Zhao et al., 2021).

Despite their potential, each remote sensing method encounters unique challenges. For instance, SAR is highly sensitive to surface roughness and vegetation cover, which can obscure the true soil moisture signal (Tsang et al., 2022). The presence of dense vegetation can cause signal attenuation, leading to underestimation of soil moisture levels. Optical and thermal methods, while valuable for their ability to capture surface temperature and reflectance, are often hampered by cloud cover and atmospheric interference, which can lead to gaps in data and reduced accuracy (Walker et al., 2004). These challenges necessitate the development of sophisticated algorithms and the integration of multi-sensor data to enhance soil moisture estimation accuracy.

While substantial progress has been made in developing algorithms for soil moisture estimation using remote sensing, there remains a critical need for comprehensive studies that benchmark these methodologies against highly accurate ground-based measurements, such as those obtained from GPR. Previous studies have primarily focused on algorithm development for individual remote sensing technologies, often without rigorous validation against in-situ data (Karthikeyan et al., 2020). This has led to discrepancies in soil moisture estimates, particularly in regions with complex terrain or varying vegetation cover. By comparing remote sensing estimates with ground-based measurements, this research aims to address this critical gap, ensuring that soil moisture monitoring systems can be trusted across different environmental settings (Li et al., 2019).

In this context, this master thesis aims to provide valuable insights into the strengths and limitations of two remote sensing approaches, contributing to the development of more accurate and integrated soil moisture monitoring systems. The findings will have practical applications in agriculture, water management, and environmental monitoring, supporting efforts to mitigate the impacts of climate change and enhance sustainable resource use.

2 Literature Review

This Section provides a comprehensive overview of the current state-of-the-art knowledge in soil moisture estimation techniques using remote sensing methods. Sub-Section 2.1 describes the fundamental aspects of soil moisture estimation. Sub-Section 2.2 delves into the estimation of soil moisture using Ground Penetrating Radar (GPR) data, discussing both the physical principles and practical applications. Sub-Section 2.3 examines soil moisture estimation using Synthetic Aperture Radar (SAR) data, covering synergetic techniques, polarimetric scattering power decomposition, data-driven approaches, and change detection methods. Additionally, Sub-Section 2.4 explores the use of optical and thermal data in soil moisture estimation, with a specific focus on the Temperature-Vegetation Dryness Index.

2.1 Fundamentals of Soil Moisture Estimation

Soil moisture estimation is a crucial aspect in fields such as agriculture, hydrology, and climate science (Robinson et al., 2008). It refers to the moisture contained in the unsaturated soil zone with a volumetric or gravimetric basis (Al-Yaari et al., 2014), which affects plant growth, soil properties, and atmospheric conditions. Accurate estimation of soil moisture is essential for effective water resource management, crop production, and environmental monitoring (Susha Lekshmi et al., 2014). Soil moisture plays a critical role in several processes, including determining irrigation requirements, influencing surface runoff, and affecting land-atmosphere interactions. Understanding and managing soil moisture is essential for optimizing agricultural productivity, managing water resources, and modeling weather and climate.

The increasing importance of soil moisture is highlighted in the context of climate change and drought. As Berg and Sheffield (2018) discuss, soil moisture is a key state variable of the land surface, reflecting complex interactions between the water, energy, and carbon cycles. They emphasize that soil moisture deficits, indicative of drought conditions, are becoming more critical to study due to global warming and its impact on ecosystems. According to Babaeian et al. (2019), soil moisture information is vital for forecasting weather and climate variability, predicting and monitoring drought conditions, managing and allocating water resources, and improving agricultural plant production. The ability to monitor soil moisture dynamics at various spatial and temporal scales has greatly enhanced our understanding of critical zone moisture dynamics, promoting sustainable environmental development and food security.

Soil moisture can be estimated through various methods, broadly classified into direct and indirect techniques (Lekshmi et al., 2014). Direct methods involve measuring soil moisture by extracting and analyzing soil samples, having its most common as the gravimetric and the volumetric methods. Indirect methods estimate soil moisture using sensors and remote sensing technologies, providing continuous and non-destructive measurements (Carlson et al., 1995). Capacitance sensors measure the dielectric constant of the soil, which changes with soil moisture (Gardner et al., 1998). These sensors are placed in the soil and provide continuous data, though they require calibration and can be affected by soil type and temperature variations. Another indirect method is Time Domain Reflectometry (TDR), where sensors send an electromagnetic pulse through the soil and measure the travel time, influenced by soil moisture (Černý, 2009). This method is highly accurate and suitable for various soil types, though it requires technical expertise. However, with the availability of low-cost sensors today, it has become more accessible. Neutron probes are another indirect method, involving a probe emitting fast neutrons into the soil (Franz et al., 2015). The neutrons slow down when they collide with hydrogen atoms, and the probe counts the slow neutrons, providing accurate readings. However, neutron probes are costly, require calibration, and involve handling radioactive materials.

Remote sensing technologies, such as satellite and aerial methods, estimate soil moisture over large areas. Optical and thermal infrared remote sensing methods measure surface reflectance and temperature, which can be related to soil moisture through empirical models (Zhang et al., 2016). However, these methods only provide surface moisture information and are affected by vegetation cover and atmospheric conditions (Lekshmi et al., 2014). Microwave remote sensing, using active (radar) and passive (radiometer) sensors, penetrates the soil surface and provides data on soil moisture, making it suitable for all-weather, day-and-night observations. Despite their advantages, these methods require complex processing and calibration (Das and Paul, 2015).

The significant advancements in microwave satellite soil moisture retrieval over the past four decades, focusing on both passive and active microwave sensors, are highlighted by Karthikeyan et al. (2017). Passive microwave sensors, such as radiometers, measure the naturally emitted energy from the Earth's surface, while active sensors, like radar, transmit microwave signals and measure the backscattered signal. These microwave measurements are sensitive to the soil's dielectric properties, which vary with soil moisture. The development of retrieval algorithms has facilitated the extraction of soil moisture information from these measurements, accounting for factors such as surface roughness, vegetation cover, and atmospheric effects.

The review by Karthikeyan et al. (2017) emphasizes the importance of accurate retrieval algorithms in enhancing the precision of soil moisture estimations. These algorithms use physical models, semi-empirical models, and empirical models to relate the microwave signals to soil moisture. Physical models, such as the Integral Equation Model (IEM), simulate the backscatter coefficients based on the soil dielectric constant, surface roughness, and sensor characteristics. Semi-empirical models simplify these physical models by calibrating roughness effects, while empirical models derive direct relationships between backscatter coefficients and soil moisture based on experimental data. Amongst empirical models, those based on AI, e.g., using Deep Neural Networks, are also proposed.

In recent years, remote sensing technologies have significantly advanced, enhancing the accuracy and applicability of soil moisture estimation (Li et al., 2021). According to Zhao et al. (2021), soil moisture is a critical parameter for understanding interactions and feedback between the atmosphere and the Earth's surface through energy and water cycles. The spatiotemporal distribution of soil moisture has long been a challenge for the remote sensing community, but advancements in electromagnetic spectrum analysis, from optical/thermal to microwave regions, have provided numerous algorithms, models, and products for practical applications. Despite these advancements, issues with retrieval accuracy, spatiotemporal resolution, and data consistency remain.

Li et al. (2021) provides an extensive review of soil moisture retrieval from remote sensing measurements, emphasizing the need for improved accuracy and consistency in soil moisture datasets. They highlight that although significant progress has been made in using optical, thermal, and microwave remote sensing for soil moisture retrieval, challenges such as spatiotemporal resolution gaps and data inconsistencies persist. An identified gap is on developing robust algorithms that can combine multi-sensor data to improve soil moisture estimation across different scales and conditions. As corroborated by Zhao et al. (2021) future research should focus on improving satellite-derived soil moisture products at fine spatial resolutions, while combining passive and active microwave measurements can provide soil moisture estimates with both higher spatial and temporal resolution.

2.2 Soil Moisture Estimation Using Ground Penetrating Radar Data

Ground Penetrating Radar (GPR) has proven to be a valuable tool for non-invasive soil moisture estimation, offering high-resolution subsurface information (Liu et al., 2019b). GPR operates by transmitting high-frequency radar pulses into the ground and measuring the reflected signals from subsurface structures. The reflection of these radar waves is influenced by the soil's dielectric properties, particularly the relative permittivity, which is closely related to soil moisture (Klotzsche et al., 2018). As soil moisture increases, the relative permittivity of the soil also increases because water has a much higher dielectric constant compared to dry soil components. By analyzing the changes in the speed and attenuation of radar waves as they travel through the soil, it is possible to estimate soil moisture (Huisman et al., 2003; Lunt et al., 2005).

There are several methodologies for estimating soil moisture using GPR. Reflection amplitude analysis, for instance, examines the amplitude of the reflected radar waves, which increases with soil moisture due to the higher dielectric constant of wet soil. By calibrating GPR data against known moisture levels, soil moisture can be estimated based on the reflection amplitude (Huisman et al., 2003). Another method is travel time analysis, which measures the time taken for radar waves to travel through the soil. As soil moisture increases, the travel time decreases due to the higher dielectric constant of water. By comparing travel times to calibration data, soil moisture can be inferred (Liu et al., 2019). Inversion techniques use mathematical models to extract soil properties, including soil moisture, from GPR data. These models consider the complex interactions between radar waves and the soil matrix, providing more detailed moisture estimations (Linde and Vrugt, 2013). Full-waveform inversion (FWI) uses the entire GPR waveform, rather than just amplitude or travel time, for more accurate and detailed soil moisture profiles by considering the complex interactions of radar waves with soil properties (Lambot et al., 2004; Minet et al., 2012).

Significant advancements in GPR technology and data processing have improved the accuracy and efficiency of soil moisture estimation. Lambot et al. (2004) introduced the far-field full-wave radar equation, providing a complete full-wave modeling of the radar signal for wave propagation in multilayered media, including antenna interactions with the medium. FWI is then used to estimate the soil electromagnetic properties, from which soil moisture is derived. The modeling framework can be applied to both frequency- and time-domain radar systems. The method was successfully applied for high-resolution mapping of soil moisture at the field scale (Minet et al., 2012), including more recently with drones (Wu et al., 2019). This accurate modeling allows for more precise estimates of soil dielectric properties. Despite the challenges associated with the well-posedness of the inverse problem when solving for multiple unknowns simultaneously, including electrical conductivity, this method is optimal because it allows for the incorporation of all the information contained in the radar data.

Lambot et al. (2006) analyzed the full-wave inverse problem by focusing the inversion on surface reflection when using off-ground GPR. The advantage of this approach is that it reduces the inverse problem to just two unknowns: the antenna height above the medium and the surface permittivity. Consequently, the inverse problem is inherently well-posed, as demonstrated by plots of the objective function under different scenarios. They also showed that the effects of electrical conductivity are negligible for frequencies above approximately 100 MHz, allowing this variable to be omitted from the inversion process. Additionally, the analysis quantified the sensitivity of surface reflection with respect to depth across different frequency ranges.

Lambot and André (2014) generalized the far-field full-wave radar equation to near-field conditions, which is in particular of high interest for on-ground GPR configurations. This method models radar antennas as an equivalent set of infinitesimal electric dipoles, together with frequency-dependent global reflection and transmission coefficients. This allows for accurate characterization of the interaction between the radar signal and soil layers, even in near-field conditions. Validation of this method showed high accuracy in estimating medium properties for different setups, highlighting its potential for digital soil mapping and nondestructive testing of planar materials.

Klotzsche et al. (2018) reviewed a decade of progress in GPR technology, highlighting improvements in hardware and methodologies. They emphasized the importance of considering factors such as soil texture, structure, and water content, which influence the electromagnetic properties measured by GPR. New data acquisition strategies, like vertical radar profiling (VRP), which combines surface and borehole measurements, have enabled detailed permittivity and attenuation profiles, further enhancing soil moisture estimation.

The integration of drone-borne GPR for soil moisture mapping, as demonstrated by Wu et al. (2019), represents a significant advancement. Their system's ability to cover large areas quickly and accurately makes it an invaluable tool for precision agriculture, enabling detailed soil moisture maps that align well with topographical features and aerial orthophotography. This technology holds promise for supporting sustainable agricultural practices by optimizing irrigation and monitoring soil health efficiently.

As demonstrated by this extensive historical evolution, GPR has evolved into a robust tool for soil moisture estimation, with continuous advancements in radar technology, signal processing, and modeling techniques. The integration of sophisticated algorithms and improved hardware configurations has significantly enhanced the accuracy and reliability of soil moisture measurements, making GPR an indispensable method in hydrology and environmental studies.

2.3 Soil Moisture Estimation Using SAR Data

It is well known that SAR data have been largely used to estimate soil moisture at high resolutions. Various studies have demonstrated the effectiveness of synthetic aperture radar (SAR) in monitoring soil moisture under different conditions, showcasing its ability to provide accurate and detailed measurements (Bauer-Marschallinger et al., 2018; Hornáček et al., 2012; Shi et al., 1997). The key lies in understanding and modeling the relationship between the backscatter coefficient and soil moisture. The radar backscatter coefficient is a measure of the fraction of the radar signal that is scattered back to the sensor (Zribi et al., 2008), and it is influenced by soil moisture, surface roughness, and vegetation cover.

The major challenge is to deal with these influences. These factors can alter the backscatter signal, complicating the interpretation of soil moisture levels (Tsang et al., 2022). Multi-incidence angle and multi-polarization SAR data can help mitigate these issues by providing additional information to disentangle the effects of roughness and vegetation from soil moisture effects (Babaeian et al., 2019).

Advanced algorithms and data assimilation techniques have been developed to enhance the accuracy of SAR-based soil moisture retrievals (Karthikeyan et al., 2017), many times merging with optical and thermal data. The following Sub-Sections bring the state-of-the-art approaches, which can be divided into four groups: synergetic techniques, methods using polarimetric scattering power decompositions, data-driven, and change detection.

2.3.1 Synergetic Techniques

Synergetic techniques in soil moisture estimation leverage the integration of SAR with other remote sensing data to enhance the accuracy and reliability of soil moisture retrievals, addressing limitations inherent in using single-source data.

One of the fundamental assumptions of synergetic techniques is that combining data from multiple sensors can mitigate the uncertainties caused by vegetation cover and surface roughness (Zribi et al., 2008). For example, the integration of SAR data with optical remote sensing data can improve the estimation of soil moisture by providing complementary information that helps in distinguishing soil moisture signals from other sources of variability. Optical sensors, such as those on the Sentinel-2 satellites, can provide vegetation indices like Normalized Difference Vegetation Index (NDVI), which are used to quantify vegetation cover and condition (Misra et al., 2020). This information is crucial for correcting the attenuation and scattering effects that vegetation has on SAR backscatter signals.

A practical application of synergetic techniques is demonstrated in the work by Ma et al. (2020), where a combination of Sentinel-1 SAR and Sentinel-2 optical data was used to improve soil moisture retrievals. The study employed a cost function-based algorithm that integrates backscatter models and optical vegetation indices. This approach was validated using ground-based measurements and showed that combining SAR with optical data significantly enhances the accuracy of soil moisture estimates, particularly in vegetated areas.

Another example is provided by Attarzadeh et al. (2018), who developed a retrieval algorithm that integrates single-polarization C-band SAR data with optical data at the plot scale in vegetated areas. By using machine learning regression techniques, specifically support vector regression (SVR), the study demonstrated that the combination of SAR and optical data could reduce the ambiguity caused by vegetation and improve soil moisture estimation accuracy. This method was applied across multiple sites with different vegetation covers, showing its robustness and applicability in various contexts.

Bao et al. (2018) further explored the synergetic use of Sentinel-1 and Landsat 8 data for soil moisture retrieval over partially vegetated areas. By modifying the Water-Cloud Model (WCM) to include vegetation water content derived from optical data, the study achieved significant improvements in soil moisture estimation accuracy. This approach underscores the importance of integrating SAR with optical data to account for the effects of vegetation, which can otherwise introduce significant errors in SAR-only soil moisture retrievals.

One major challenge for this approach is the requirement for accurate and high-resolution ancillary data, such as vegetation indices and surface roughness measurements, which are necessary for calibrating and validating the integrated models (Amazirh et al., 2018). Additionally, the complexity of combining datasets from different sensors and the need for sophisticated algorithms to process and fuse the data can be resource intensive.

2.3.2 Polarimetric Scattering Power Decomposition

Polarimetric scattering power decomposition leverages the different scattering mechanisms inherent in natural surfaces to decompose the backscattered radar signal into its constituent components (Touzi, 2016). Typically, these components include surface scattering, volume scattering, and double-bounce scattering. This decomposition facilitates a more detailed understanding of the observed scene by isolating the contributions from soil and vegetation, thus enhancing the accuracy of soil moisture estimation (Ferguson and Gunn, 2022).

A foundational approach in polarimetric decomposition is the model-based Freeman-Durden decomposition (Chen et al., 2014), which segregates the radar backscatter into three fundamental scattering mechanisms: surface scattering, volume scattering, and double-bounce scattering. This model has been instrumental in interpreting SAR data and has been widely adopted due to its simplicity and effectiveness in a range of environments (Touzi, 2016). Surface scattering is generally associated with bare soils or smooth surfaces, volume scattering with vegetation or rough surfaces, and double bounce scattering with structures such as buildings or tree trunks reflecting off the ground (Hajnsek et al., 2009; Jagdhuber et al., 2012).

However, as stated by Jagdhuber et al. (2012), the traditional Freeman-Durden decomposition faces limitations, especially in complex environments where mixed scattering mechanisms are present. To address these limitations, modifications have been proposed. For instance, the introduction of the extended Bragg (X-Bragg) model incorporates a cross-polarized component generated by surface roughness (Chen et al., 2014). This modification enhances the model's ability to handle more complex scattering scenarios by considering the roughness-induced depolarization effects, thereby improving soil moisture estimation under varied surface conditions (Hajnsek et al., 2009).

Further advancements in polarimetric decomposition involve multi-angular approaches. These methods leverage data acquired at different incidence angles to increase the robustness of soil moisture retrieval (Chen et al., 2014). By combining multi-angular polarimetric data, researchers can mitigate the ambiguities arising from single-angle observations, thus enhancing the reliability of the inversion results. This approach has been shown to improve soil moisture estimation by providing a more comprehensive view of the scattering mechanisms, which is particularly useful in agricultural fields where vegetation cover can vary significantly (Jagdhuber et al., 2012).

2.3.3 Data-driven

The data-driven approach for soil moisture estimation using SAR focuses on leveraging machine learning techniques to derive soil moisture. These approaches bypass the need for explicit physical modeling of the radar backscatter response to soil moisture, instead relying on algorithms to identify patterns and correlations directly from the data. This method is particularly advantageous in complex environments where traditional models may struggle to account for the numerous variables influencing SAR backscatter, such as vegetation cover, soil texture, and surface roughness (Singh et al., 2023).

Machine learning algorithms, including Support Vector Regression (SVR) and Random Forest Regression (RFR), have been increasingly applied to SAR data for soil moisture retrieval (Ali et al., 2015). These algorithms do not require assumptions about the underlying data distribution, making them robust in diverse and complex conditions. For instance, SVR has demonstrated high accuracy in soil moisture estimation by effectively generalizing from limited training data and handling noise robustly. This was highlighted in a study by Chaudhary et al. (2022), where SVR outperformed other models in retrieving soil moisture using SAR and optical data from the Colorado River basin, showcasing its adaptability and accuracy.

Random Forest Regression (RFR) is another prominent machine learning approach used for soil moisture estimation (Datta et al., 2021). Known for its high computational efficiency and robustness, RFR can handle large datasets with numerous features without overfitting, even with relatively few variables (Mantas et al., 2019). This algorithm calculates the importance of each variable, which helps in understanding the contributing factors to soil moisture variability. In a study comparing SVR, RFR, and other models, Adab et al. (2020) found that RFR provided more accurate soil moisture estimates than SVR and Artificial Neural Networks (ANN) when applied to optical and thermal data in semi-arid regions.

The effectiveness of these machine learning models is further enhanced by the integration of multi-temporal SAR data. By incorporating backscatter coefficients from multiple dates, the models can mitigate noise and improve stability in their predictions. Wang et al. (2022) demonstrated that the inclusion of average backscattering coefficients from three neighboring dates significantly improved the accuracy of soil moisture estimation models, including SVR and RFR. This multi-temporal approach helps in stabilizing the SAR signals, which are often affected by transient surface conditions.

Moreover, Sentinel-1A SAR imagery, with its high temporal resolution and weather-independent data acquisition capabilities, is particularly suitable for these data-driven approaches (Pandit et al., 2022). Sentinel-1A's frequent revisit times ensure a consistent data stream, which is critical for monitoring dynamic soil moisture conditions (Filipponi, 2019). Studies have shown that using Sentinel-1A data, SVR and RFR models can effectively map soil moisture over large areas without the need for ancillary data on soil surface roughness or vegetation cover, making them practical for operational applications (Chaudhary et al., 2022).

In practical applications, data-driven models have been implemented successfully in estimating soil moisture for various scopes. Paloscia et al. (2013) demonstrated the use of neural networks combined with SAR data for soil moisture retrieval in agricultural fields, showing that machine learning techniques could effectively handle the complexity of different crop types and growth stages, thus enhancing the reliability of soil moisture estimates. The adaptability of these models to various environmental conditions and their ability to integrate multi-temporal data make them highly effective for soil moisture monitoring, providing accurate and timely information essential for agricultural and hydrological applications (Santi et al., 2019).

2.3.4 Change Detection

Change detection (CD) is a vital approach in the estimation of soil moisture using SAR data. This technique leverages the temporal variations in radar backscatter to infer changes in soil moisture. One of the pioneering works in this domain was introduced by Wagner et al. (1999), who utilized scatterometer data to estimate soil moisture. Their approach relies on the assumption that surface roughness and vegetation cover remain relatively constant over short periods, allowing for the isolation of soil moisture changes from the overall backscatter signal. The CD algorithm developed by Wagner et al. describes backscatter as a function of the local incidence angle, time, and soil moisture, using empirical parameters for dry and wet soil conditions.

A significant advancement in the CD approach was achieved by Zribi et al. (2008), who incorporated the NDVI to correct for vegetation effects on soil backscatter. This correction is crucial for improving the accuracy of soil moisture estimates in areas with variable vegetation cover. The method proposed by Zribi et al. was validated using high-resolution SAR data, demonstrating its effectiveness in semi-arid regions where vegetation effects are prominent.

Following its results, Balenzano et al. (2010) further explored the CD technique by utilizing backscatter ratios of consecutive acquisitions from dense temporal multi-frequency airborne SAR data. This approach enhances the temporal resolution of soil moisture monitoring, making it particularly suitable for agricultural applications. Balenzano et al. highlighted the importance of multi-temporal acquisitions in tracking soil moisture changes under various crop conditions.

More recently, Bauer-Marschallinger et al. (2018) adapted the CD method for Sentinel-1 SAR data. Similarly to previous authors, their algorithm attributes changes in normalized backscatter to variations in soil moisture, using statistical methods to estimate dry and wet reference backscatter coefficients. This enhancement allows for more accurate soil moisture retrievals, even in areas with limited historical data. The Sentinel-1 based approach provides high spatial and temporal resolution, making it suitable for large-scale soil moisture mapping.

Bhogapurapu et al. (2022) introduced a modified change detection approach that utilizes dual-polarimetric SAR data. Their method incorporates a SAR-derived vegetation index to account for vegetation effects on soil backscatter, providing an alternative to traditional optical indices like NDVI. This approach was validated using data from the Texas Soil Observation Network, showing good agreement between estimated and observed soil moisture values. Bhogapurapu et al. emphasized the potential of this method for operational soil moisture monitoring, especially in regions with frequent cloud cover where optical data may be unreliable. This approach stands out for strengthening the positive aspects of SAR, while dealing with its limitations.

Overall, change detection techniques have evolved significantly, incorporating various methods to ensure correction for vegetation and surface roughness effects, thereby enhancing the accuracy of soil moisture estimates derived from SAR data. These advancements underscore the importance of multi-temporal SAR acquisitions and the integration of ancillary data, such as vegetation indices, in improving soil moisture retrievals.

2.4 Soil Moisture Estimation Using Optical/thermal Data

Combining optical and thermal remote sensing data has been successfully applied to soil moisture estimation across various fields (Zhang and Zhou, 2016). In agriculture, this approach is crucial for monitoring soil moisture levels, optimizing irrigation schedules, and predicting soil moisture availability for crops.

Many methods explore the relationship between TIR and optical bands to be able to estimate soil moisture. One of the foundational methods is based on thermal inertia retrieval using thermal infrared remote sensing techniques, as examined by Matsushima et al. (2012). This approach leverages the strong correlation between thermal inertia and soil water content. The method involves retrieving thermal inertia from a surface heat budget model that uses radiative surface temperatures, insolation, and meteorological data observed in field experiments. This model demonstrated the potential to estimate subsurface soil moisture with precision levels of ±4% of the daily volumetric soil moisture at a significance level of 5%, using data from geostationary and multiple polar orbiting satellites, combined with routine meteorological observations.

Further developments in the field of soil moisture retrieval have led to the use of the Thermal-Optical Trapezoid Model (TOTRAM), which integrates both thermal and optical data. This method interprets the relationship between LST and vegetation indices to estimate soil moisture. However, the traditional TOTRAM model faced limitations due to the variability of LST influenced by near-surface temperature, relative humidity, and wind speed. To overcome these challenges, modifications were proposed, such as using shortwave infrared bands instead of thermal bands, enhancing the model's robustness and reducing the need for constant calibration (Ambrosone et al., 2020).

Koley and Jeganathan (2020) explored soil moisture estimation using data from Landsat-8 and Sentinel-2A satellites. Their study area in Jharkhand, India, provided a context for applying multispectral and thermal imagery to estimate soil moisture. The use of Landsat-8, which provides both multispectral and thermal imagery, and Sentinel-2A, known for its high spatial and temporal resolution, demonstrated the practical applications of combining optical and thermal data to improve soil moisture estimation in diverse climatic conditions.

In recent years, advancements in machine learning have further enhanced soil moisture estimation techniques. Luo et al. (2023) developed a neural network model that utilizes optical and thermal data to estimate surface soil moisture in bare land and vegetated areas. This approach addresses the complexity of soil moisture estimation by integrating various data inputs and leveraging the predictive power of neural networks, providing a significant improvement over traditional models in terms of accuracy and adaptability to different environmental conditions.

The continuous improvement and integration of these methods promise to enhance the precision and applicability of soil moisture estimation across diverse landscapes and climatic conditions.

One of the critical methods in this domain is the Temperature-Vegetation Dryness Index (TVDI), which will be discussed in detail in this Sub-Section.

2.4.1 Temperature-Vegetation Dryness Index

The work of Carlson et al. (1994) laid the groundwork for TVDI by developing a method that leveraged thermal infrared temperature and NDVI measurements to infer surface soil water content in the presence of variable vegetation cover, specifically for agricultural lands. By coupling a Soil-Vegetation-Atmosphere-Transfer (SVAT) model with satellite-derived surface radiant temperature and NDVI data, Carlson and colleagues addressed the complexities introduced by vegetation cover. Their study demonstrated how variations in vegetation and soil moisture influence surface temperatures, providing a theoretical framework that has been fundamental for the creation of the index.

An important study developed by Sandholt et al. (2002) introduced a simple interpretation of the surface temperature/vegetation index space for assessing surface moisture status, stating for the first time the TVDI, to delineate wet and dry edges. This method enabled the estimation of soil moisture availability by positioning the LST and NDVI data points within this triangular space. TVDI values closer to 1 indicate dry conditions, whereas values near 0 suggest wet conditions. By comparing its results against soil moisture estimations from hydrological models over Senegal, the authors proved that the spatial variation in TVDI reflected the variation in moisture for the area. However, different authors reported the possibility of finding a trapezoid rather than a triangular relationship when performing the scatterplot between temperature and a vegetation index (Carlson et al., 1994; Han et al., 2006; Liu and Yue, 2018; Tao et al., 2020). Either way, the relationship demonstrates the central role of evapotranspiration in the dynamics between surface temperature and vegetation cover.

Many authors have explored TVDI's methodology and applications. Stisen et al. (2008) enhanced the original TVDI methodology by integrating thermal inertia to estimate regional evapotranspiration. This approach was applied using MSG-SEVIRI data in the Senegal River basin, demonstrating that the combination of TVDI and thermal inertia significantly improved the accuracy of evapotranspiration estimates in heterogeneous landscapes. Their findings emphasized the potential of this combined method for large-scale drought monitoring, addressing some limitations of the original TVDI by accounting for thermal properties of the land surface.

Holzman et al. (2014) explored the relationship between TVDI and crop yield, specifically focusing on soil moisture and its impact on crop production in the Argentine Pampas. They utilized MODIS data to calculate TVDI and examined its correlation with soybean and wheat yields across different agro-climatic zones. Their results showed a strong correlation between TVDI and soil moisture measurements, with R^2 values ranging from 0.61 to 0.83. Furthermore, they found that TVDI could predict crop yields with significant accuracy, making it a valuable tool for pre-harvest yield forecasting in rainfed agricultural systems.

Different authors suggested modifications to TVDI to enhance its accuracy and applicability in various environmental contexts. Tang et al. (2010) further refined the TVDI methodology by developing an algorithm for the precise determination of dry and wet edges within the Ts-VI triangle method. This enhancement was crucial for accurately estimating regional evapotranspiration from MODIS data in arid and semi-arid regions. By validating their method with Large Aperture Scintillometer (LAS) measurements, Tang and colleagues confirmed the reliability and accuracy of the enhanced TVDI approach, marking a significant advancement in its applicability for large-scale environmental monitoring.

In order to improve upon the traditional TVDI, Rahimzadeh-Bajgiran et al. (2011) introduced a modified approach that incorporate air temperature and a Digital Elevation Model (DEM) to develop the improved TVDI (iTVDI). The results demonstrated statistically significant relationships with recent precipitation and soil moisture across different land cover types in the study area. The study concluded that this approach could be successfully used for vegetation and soil water stress monitoring in semi-arid regions, offering a robust tool for environmental monitoring and resource management.

Also addressing modifications, Przeździecki et al. (2023) focused on the temporal variability of TVDI to estimate soil moisture conditions in forested areas. The authors proposed a new approach to the TVDI calculation method in which a time series of scenes is used instead of a daily approach. By examining changes in LST and NDVI over time, their study highlighted how temporal TVDI could effectively monitor soil moisture dynamics. This innovative approach extended TVDI's applicability beyond static measurements, emphasizing its potential for managing forest health and mitigating fire risks through continuous monitoring. Nevertheless, this modification applicability was not tested in different environments.

All this evidence demonstrates the applicability of TVDI and highlights the improvements made to it. However, additional experiments, particularly those involving comparisons with different estimation methods, are necessary to validate its effectiveness across various scenarios.

3 Research Objectives

Despite the significant advancements in soil moisture estimation methods, presented in Section 2, challenges remain in achieving consistent spatiotemporal validation across diverse environmental conditions. The literature underscores the importance of integrating multi-sensor data to mitigate the limitations inherent in single-source approaches, particularly in the presence of variable vegetation cover and surface roughness. However, there is still room to further explore how different data sources perform in comparison to high accurate estimations as the ones based on GPR data.

The overarching objective of this research is to comprehensively evaluate and compare the effectiveness of two distinct methodologies based on—SAR and Optical/Thermal data—in estimating soil moisture. This study aims to integrate satellite remote sensing data with GPR data to assess the spatiotemporal trends and variability in soil moisture estimations.

Specifically, the first objective is to develop a SAR-based methodology, as well as an optical/thermal-based methodology, to achieve reliable soil moisture estimates. The second objective is to investigate the relationship between soil moisture estimations obtained from these methodologies and those measured using GPR. This will include analyzing the correlation and differences between the SAR-based and optical/thermal-based estimations with the GPR measurements, providing insight into the comparative accuracy and reliability of these approaches.

The final objective is to evaluate the performance and limitations of the SAR and Optical/Thermal products. This will involve assessing the ability of each methodology to capture the spatial and temporal variability of soil moisture accurately, thereby determining their suitability for different application scenarios.

These objectives aim to answer the following research question: How do the spatiotemporal trends and variability of soil moisture estimations obtained through SAR and Optical/Thermal based methodologies qualitatively compare with those derived from GPR measurements?

4 Materials

This Section provides background information regarding the study area and the datasets used in this research. Sub-Section 4.1 provides a comprehensive description of the study area with context. Sub-Section 4.2 delves into the data sources utilized and outlines the various data types employed.

4.1 Study Area

This Sub-Section provides a comprehensive overview of the study area, contextualizing the research and understanding the various factors that influence our investigation. By examining the geographical, physical, socio-economic, and infrastructural characteristics, a solid foundation is structured for the analysis and findings that follow.

4.1.1 Geographical Location

The study area, known as the Grand Villers field, is situated in Belgium, specifically within the municipality of La Bruyère. La Bruyère is located in the Wallon region, as shown in Figure 1. The center of the Grand Villers field is at coordinates 4°49’12” E and 50°32’18” N. It falls within the delineated area shown by the red outline on the map, which provides a contextualized view of the local landscape. The field encompasses an area of approximately 6 hectares.

Notably, this field was selected due to its ongoing monitoring by drone-borne GPR as part of the Public Service of Wallonia (SPW) DuraTechFarm project. This project plays a crucial role in assessing the field’s soil characteristics, contributing valuable data for sustainable agricultural practices.

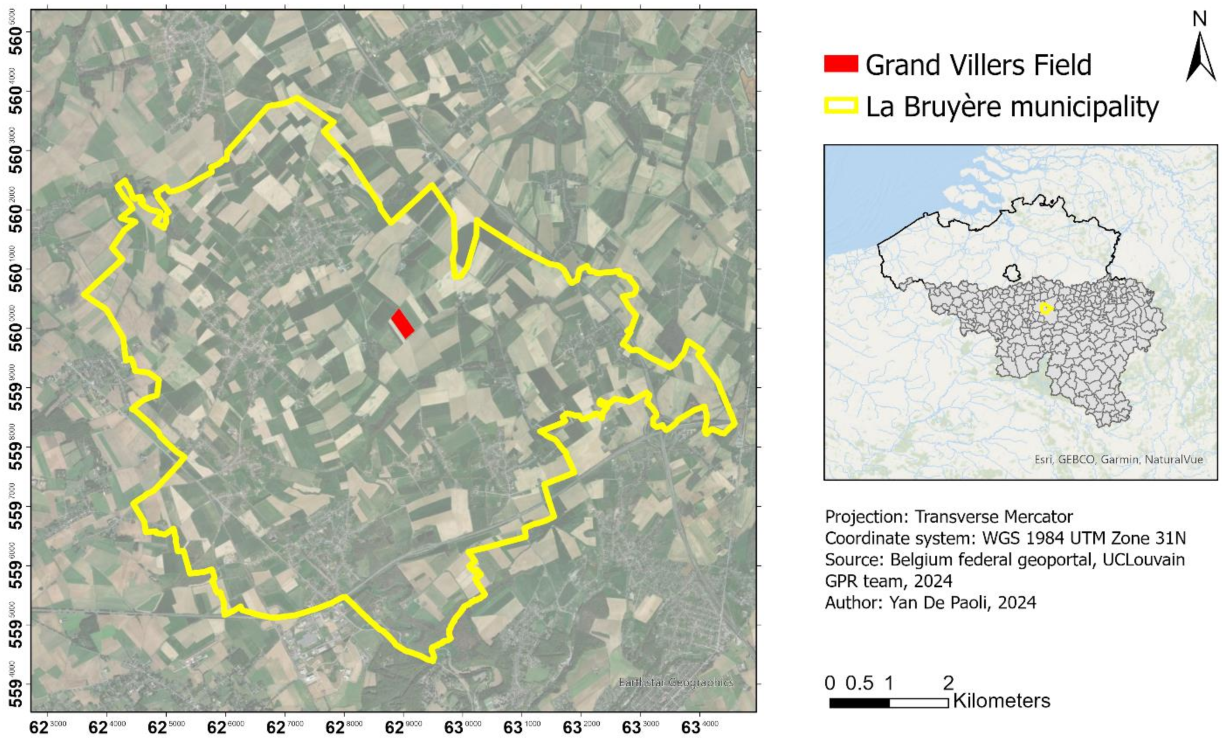

Figure 1: Location of the Grand Villers field within La Bruyère municipality, Belgium. The image highlights the Grand Villers field (solid red area) situated within the La Bruyère municipality (yellow boundary). The inset map provides a broader geographical context, showing the position of La Bruyère municipality within Belgium.

Figure 1 highlights the area of interest (AOI), within the boundary of the La Bruyère municipality. This area is part of a larger agricultural landscape characterized by a patchwork of fields and small woodlands, typical of the Walloon countryside. Additionally, the inset map provides a broader view, situating La Bruyère within the province of Namur, part of the Wallon Region in southern Belgium.

Moving to a broader perspective, Namur exhibits a diverse topography that significantly impacts its ecological and human systems. Its southern part extends into the Ardennes plateau, characterized by dense forests, rolling hills, and deep valleys. This region's rugged terrain includes higher elevations, contributing to varied microclimates and ecological niches. The central part of the province is dominated by the Condroz region, marked by its undulating hills and fertile valleys. This landscape results from the geological formation of alternating bands of limestone and sandstone, creating a pattern of ridges and depressions (Wallonie Service Public SPW, 2023).

Focusing specifically on La Bruyère, this municipality experiences a temperate maritime climate, characterized by mild temperatures and consistent precipitation throughout the year. Average temperatures range from approximately 2°C in January to 18°C in July, providing a moderate climate conducive to a wide range of agricultural and ecological activities. Winters are typically mild with occasional frost, while summers are warm but not excessively hot. The region receives an average annual precipitation of about 800 to 1000 mm, with rainfall evenly distributed throughout the year, though autumn tends to be the wettest season (SPW Agriculture, 2023).

The topography of La Bruyère, as is possible to see in Figure 2 (b), includes gently rolling hills and fertile valleys, as part of the Hesbaye region. The landscape is shaped by underlying geological formations of loess and clay, creating a series of gentle slopes and flat areas. These geological features influence soil composition and agricultural potential, making the area highly suitable for a variety of crops and pasturelands. Minor watercourses contribute to the area's drainage and hydrology, playing a vital role in local agriculture and ecosystem services. The elevation in La Bruyère is relatively moderate, with a mean value of 258 meters, which supports diverse land uses and human settlement patterns (SPW Agriculture, 2023).

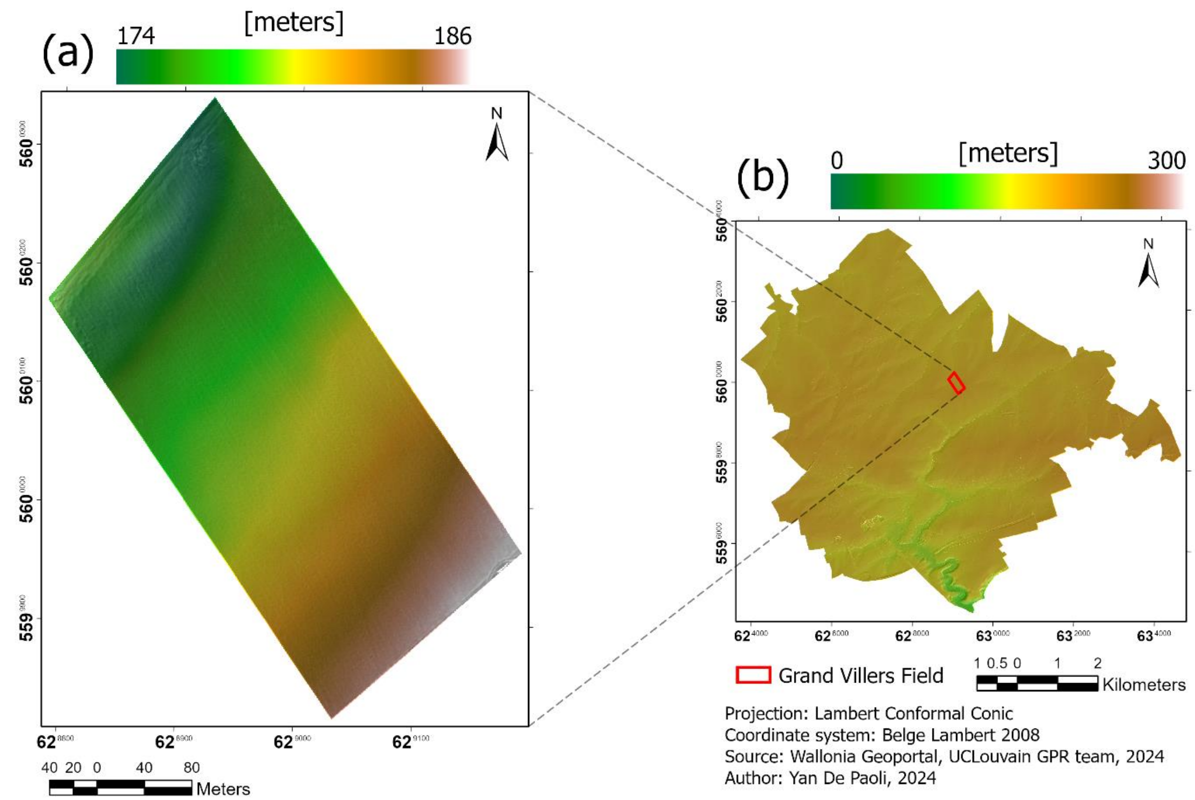

Figure 2: Elevation maps of the study area and La Bruyère municipality. (a) Detailed elevation map of the Grand Villers field (indicated by the red rectangle) with elevation values ranging from 174 to 186 meters. (b) Broader elevation map of the municipality with elevation values ranging from 0 to 300 meters.Data obtained from Wallonia Geoportal.

Moreover, Figure 2 (a) presents the detailed elevation profile of the AOI, which shows a subtle elevation range between 174 and 186 meters, resulting in an elevation difference of 12 meters. The gradient visible across the map suggests slight undulations in the terrain within the field, with the elevation generally increasing from the northwest to the southeast.

4.1.2 Land Use and Land Cover

The municipality of La Bruyère is characterized by diverse land use and land cover (LULC), which has evolved significantly over the years. The region primarily consists of agricultural land, with arable farming being the predominant activity. This is supported by fertile loamy soils, conducive to the cultivation of a variety of crops including cereals, potatoes, and sugar beets (Brogna et al., 2018). In addition to agricultural land, La Bruyère also includes areas of mixed forest, pasture, and built-up regions, reflecting a landscape that balances agricultural productivity with residential and commercial developments (Beckers et al., 2013). These land uses are integral to the socio-economic framework of the municipality, supporting both local economies and lifestyles.

The soil types within La Bruyère significantly influence its land use patterns. Figure 3 presents the soil type distribution for the municipality, and a closer examination of the AOI. Predominantly, the soil present in the municipality, shown in the panel on the right, is loamy with varying degrees of drainage levels. These soils are classified into several categories based on their texture and drainage properties, which include well-drained loamy soils, moderately drained loamy soils, and poorly drained loamy soils (État de l'environnement Wallon, 2018). This classification impacts the suitability of different areas for various types of agricultural practices, such as crop cultivation, which thrives in well-drained soils, versus pasture or forestry that may be more suitable for areas with moderate to poor drainage. The presence of such diverse soil types supports a range of agricultural and silvicultural activities, contributing to the multifunctional landscape of La Bruyère.

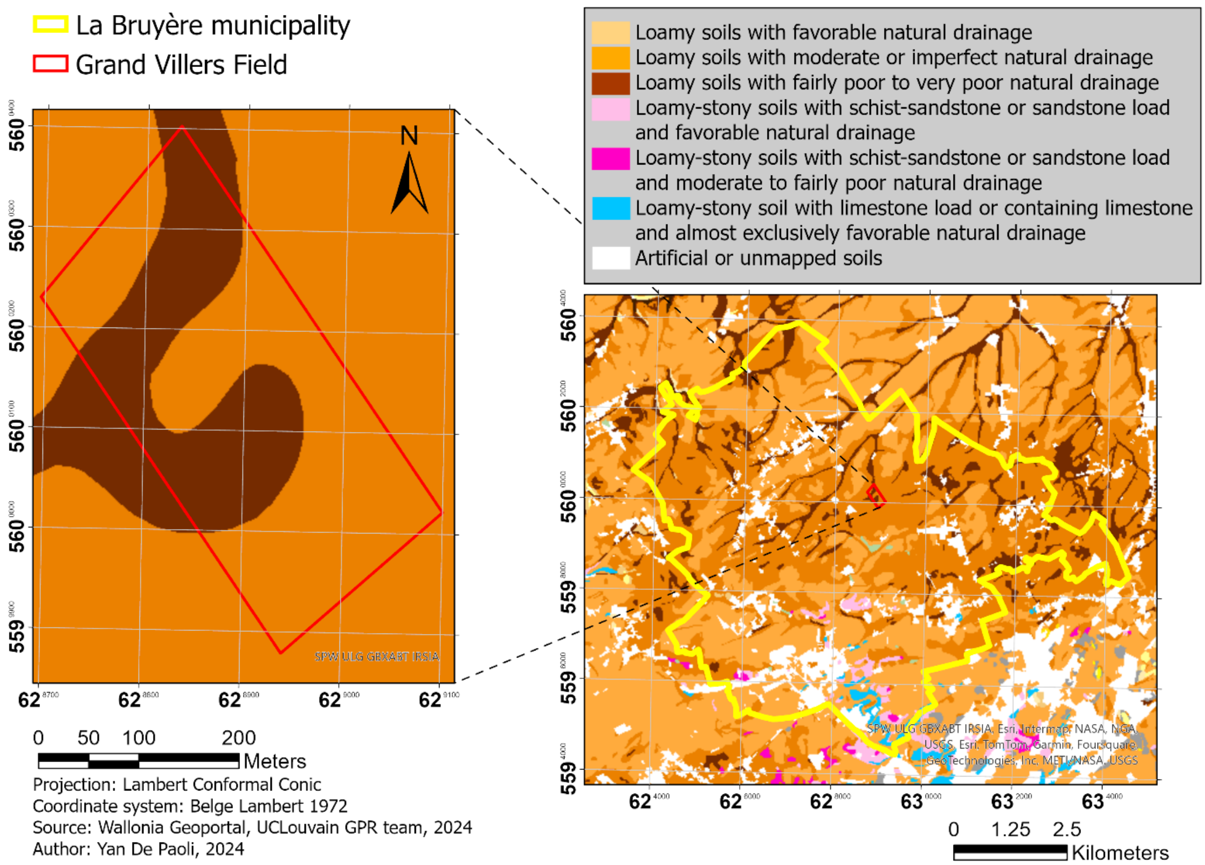

Figure 3: Soil maps of the study area and La Bruyère municipality. On the left there is a zoomed in soil map of the Grand Villers field (indicated by the red rectangle) containing loamy soils with different capacity of natural drainage. On the right there is a broader soil map of the municipality (indicated by the yellow boundary) with different types of soil. Data obtained from Wallonia Geoportal.

The panel on the left provides a detailed view of the soil types within the AOI. Although the area consists solely of loamy soils, two distinct types of natural drainage are present: moderate or imperfect drainage, and fairly poor to very poor natural drainage.

4.1.3 Socio-Economic Context

Changes in LULC within the municipality are also driven by socio-economic factors and environmental policies. Urban expansion has led to an increase in built-up areas, as is possible to see in Figure 3 on the left panel (represented by the white areas), while agricultural practices have adapted to technological advancements and market demands. Furthermore, environmental conservation policies have aimed to preserve natural habitats and promote sustainable land management practices (SPW Agriculture, 2023). The integration of these policies helps mitigate the impacts of land use changes on local ecosystems, ensuring the long-term sustainability of both agricultural and natural landscapes. Consequently, La Bruyère exemplifies a dynamic interaction between natural resources and human activities, shaping its current land use and land cover patterns.

The importance of agriculture in La Bruyère extends beyond economic contributions, shaping the social fabric and cultural heritage of the community. Agricultural practices in the area are intertwined with local traditions and community life, reflecting a long-standing history of land stewardship and rural development. The municipality's commitment to sustainable agricultural practices, such as crop rotation and organic farming, underscores the region's dedication to environmental conservation and resilience against economic fluctuations. These practices not only ensure the sustainability of local agriculture but also enhance biodiversity and soil health, contributing to the overall well-being of the community (Wallonie Service Public SPW, 2023).

4.1.4 Agricultural practices on the field

As a last important aspect to be mentioned in the characterization of the study area, and thanks to the Walloon Agricultural Research Center, detailed records of agricultural practices on the Grand Villers field have been documented. The AOI has been utilized for diverse crop rotations over recent years, reflecting a strategic approach to maintaining soil health and optimizing agricultural productivity.

In 2023, spinach was cultivated in the field with two distinct sowing and harvesting periods. The first sowing took place on 6th May 2023, followed by harvesting on 23rd June 2023. A second sowing occurred on 14th August 2023, with harvesting on 23rd September 2023. This practice of sequential planting allows for maximizing the use of the field throughout the growing season, ensuring efficient land use and crop production.

Historical data from the previous year's indicate a varied crop rotation strategy. In 2022, onions were grown in the field, while in 2021, the crop was spelt, a type of wheat known for its hardiness and nutritional benefits. In 2020, potatoes were cultivated, contributing to the crop diversity essential for preventing soil depletion and pest cycles. Moreover, information regarding irrigation for two specific dates was shared. On September 12, 2023, 3.3 mm was registered and on September 12, 2023, 11.7 mm was registered.

4.2 Data Sources

The current study utilized three different types of data including on-the-field drone borne measurements, on-the-field sensor measurements, and satellite remote sensing. The drone-borne GPR data was acquired by UCLouvain GPR's team. The field sensor measurements data was accessed from Sencrop's database available online. The remote sensing data was taken from Sentinel-1 of the Copernicus program and from Landsat 9, part of the Landsat program which is managed by the United States Geological Survey (USGS) and the National Aeronautics and Space Administration (NASA). The data description is explained below:

4.2.1 Meteorological field measurements

The data was acquired through Senscrop's - Raincrop connected rain gauge equipment, installed in the field, with records available for 2022 and 2023. The variables measured were air temperature and precipitation. This equipment, positioned at 2 meters height, uses a tilting bucket for precise rainfall measurement, and a hygrometer thermometer for air temperature measurement, providing real-time data. The company supplies information with daily time steps on these variables, with the instrument positioned in the field to offer valuable ground truth information.

4.2.2 GPR Data

GPR measurements were conducted by the UCLouvain GPR's team to provide high-resolution data. The GPR system used was the gprSense[1], a prototype developed by Sébastien Lambot. This system integrates lightweight vector network analyzer technology as the radar unit with a 110-120 MHz dipole antenna. It provides soil moisture information with a characterization depth of approximately 35-40 cm and employs full-wave inverse modeling for precise radar data processing. The drone flights were fully automated, maintaining a terrain-following altitude of about 2 meters. The offset between the acquisition lines was approximately 5 meters, with the spacing between measurements along the lines ranging from 0.5 to 1 meter. The measurements

[1] Link to source: www.gprsense.com

were conducted during the end of August until the end of September 2023, more specifically over the 8 following days: August 22nd, 25th, 29th, and September 5th, 8th, 11th, 15th, and 20th.

4.2.3 Sentinel-1 Ground Range Detected Data

The data used in this study comprises radar imagery acquired from the Sentinel-1 satellite. Sentinel-1 is part of the European Space Agency's Copernicus program, which provides critical data for monitoring and managing Earth's surface, delivering key observations for agriculture, forestry, land use planning, and disaster management (Filipponi, 2019). The data utilized in this study was accessed through Google Earth Engine, which offers free and open access to Sentinel-1 products using Java Script. The data extraction was performed for the AOI within the temporal range from January 2019 to December 2023. This period was selected to ensure the temporal relevance and dataset robustness needed for the model (Bhogapurapu et al., 2022).

Sentinel-1 provides Synthetic Aperture Radar (SAR) imagery, which is useful for observing Earth's surface regardless of weather conditions and daylight (Filipponi, 2019). The specific data product used in this study is the Ground Range Detected (GRD) product. To ensure consistency and relevance of the data, only Interferometric Wide Swath mode (IW) was selected. This mode provides co-polarized (VV), cross-polarized (VH), and angle information. The specifications of Sentinel-1 GRD modes are shown in Table 1.

Table 1: Sentinel-1 GRD data specifications for Interferometric Wide Swath (IW), Extra Wide Swath (EW), and Strip Map (SM) modes, with HH (Horizontal-Horizontal), HV (Horizontal-Vertical), VV (Vertical-Vertical), and VH (Vertical-Horizontal) indicating radar polarization (Source: ESA, 2024)

Mode	Polarization	Resolution Range (m)	Resolution Azimuth (m)	Pixel Spacing Range (m)	Pixel Spacing Azimuth (m)
IW	HH+HV, VV+VH	20	22	10	10
EW	HH+HV, VV+VH	40	40	25	25
SM	HH, VV, HH+HV, VV+VH	9	9	4	4

4.2.4 Landsat 9 Collection Data

The data used in this study comprises optical and thermal imagery acquired from the Landsat 9 satellite. The Landsat 9 satellite provides critical data for monitoring and managing Earth's resources, delivering key observations for agriculture, forestry, land use planning, and water management (Masek et al., 2020). The data utilized in this study was accessed via an Application Programming Interface (API) connected to the USGS Earth Explorer portal, which offers free and open access to Landsat products. The data extraction was performed for the AOI within the temporal range from January 2022 to December 2023. This period was selected to ensure the temporal relevance of the study. The specifications of Landsat 9 bands are shown in Table 2.

Table 2: Spectral band specifications for Landsat-9, including band edges, center wavelengths, and spatial resolution at nadir (Source: NASA Landsat Science, 2024)

Band	Minimum Lower Band Edge (nm)	Maximum Upper Band Edge (nm)	Center Wavelength (nm)	Maximum Spatial Resolution at Nadir (m)
Coastal / Aerosol	433	453	443	30
Blue	450	515	482	30
Green	525	600	562	30
Red	630	680	655	30
NIR	845	885	865	30
SWIR 1	1560	1660	1610	30
SWIR 2	2100	2300	2200	30
Panchromatic	500	680	590	15
Cirrus	1360	1390	1375	30
Thermal 1	10300	11300	10800	100
Thermal 2	11500	12500	12000	100

5 Methods

This Section presents a comprehensive overview of the methodology used for soil moisture estimation, benchmarking the SAR-based change detection approach and TVDI. Sub-Section 5.1 describes data preprocessing of all data used. In Sub-Section 5.2 the change detection methodology is described. Then, Sub-Section 5.3 provides a detailed explanation about the TVDI. Finally, Sub-Section 5.4 focuses on the statistical analysis implemented to evaluate and compare the methodologies.

5.1 Data Preprocessing

5.1.1 Meteorological Field Measurements Data Preparation

The meteorological field data, initially provided in excel CSV files, was converted into Python data frames for easier manipulation and analysis. The subsequent figures illustrate the available field measurements, which will be incorporated into the comprehensive analysis.

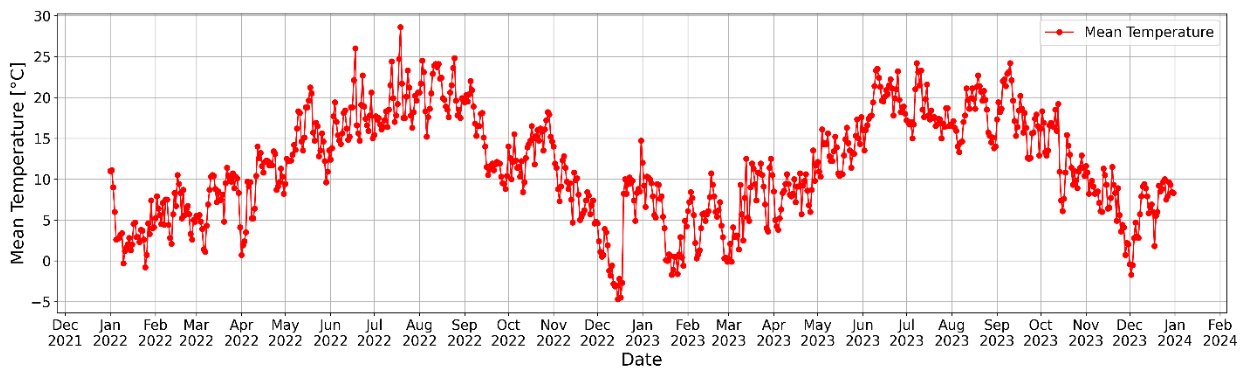

Figure 4: AOI mean temperature over time from December 2021 to January 2024. The graph shows daily mean temperature measurements (°C). The data points are marked in red, indicating the fluctuation in temperatures over time. Data obtained from Senscrop.

Figure 4 shows the mean AOI temperature over time. The x-axis represents the time from January 2022 to December 2023, while the y-axis shows the mean temperature in degrees Celsius. It is possible to observe a general seasonal pattern with higher temperatures during the summer months and lower temperatures during the winter months. There are noticeable peaks in mid-2022 and mid-2023, corresponding to the summer seasons, with temperatures reaching around 25°C. Conversely, the temperature drops to around 5°C during the winter months.

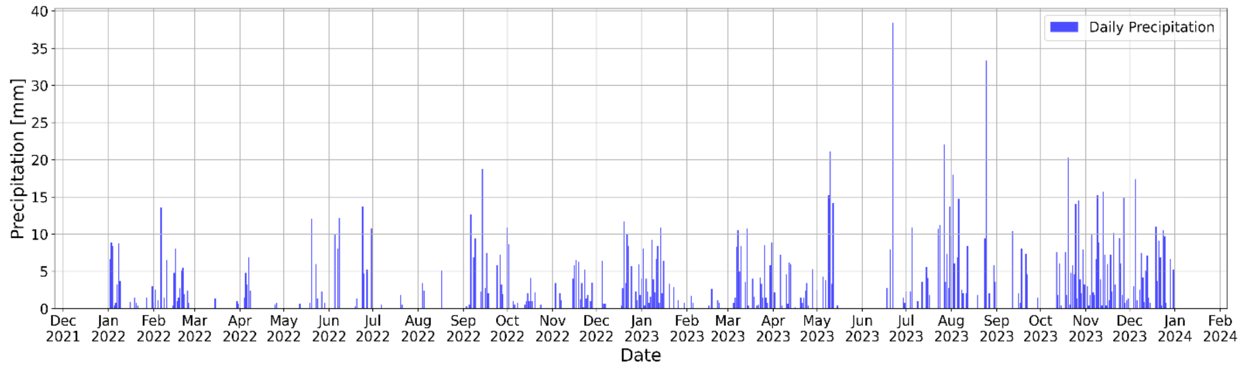

Figure 5: Precipitation over time from December 2021 to January 2024. The bar chart illustrates daily precipitation (mm). The data points, represented as vertical blue bars, show variability in precipitation levels. Data obtained from Senscrop.

Figure 5 presents precipitation on the field over time. The x-axis also represents the time from January 2022 to December 2023, and the y-axis displays the daily precipitation in millimeters. The data shows sporadic precipitation events, with some days experiencing significant rainfall exceeding 30 mm. There are periods of higher precipitation, particularly noticeable in the spring and autumn months, which suggests seasonal rainfall patterns.

5.1.2 GPR Data Preparation

To ensure accurate soil moisture estimation, the radar data was processed by the UCLouvain GPR's team using full-wave inversion techniques, as demonstrated by Wu et al. (2019). This approach is based on the radar equation formulated by Lambot et al. (2004) together with the inversion strategy of Lambot et al. (2006), focusing inversion on the surface reflection in the time domain. The radar was calibrated by performing drone-radar measurements at different heights over the lake of Grand-Leez, located a few kilometers apart from the AOI.

Following the inversion process, the data was interpolated using kriging, a geostatistical method that generates high-resolution soil moisture maps. This technique ensures spatial continuity and accuracy, resulting in soil moisture maps with a spatial resolution of approximately 1.3 meters.

5.1.3 Grid Definition

Given that the proposed methods are pixel-based, it was necessary to establish a common spatial ground, represented by grids based on the GPR soil moisture estimations. With that aim, the original soil moisture estimation maps, created with GPR, were resampled using the bilinear interpolation method in ArcGIS Pro software. Bilinear interpolation calculates the value of each pixel by averaging (weighted for distance) the values of the surrounding four pixels (Kirkland, 2010).

The resampling was performed to 20 and 30 meters to meet satellite image resolutions. The centroids of the resulting pixels were stored as a table of points, referred to as sample points in this work, enabling point-by-point or pixel-by-pixel comparisons with the proposed methodologies.

5.1.4 Sentinel-1 Data Preparation

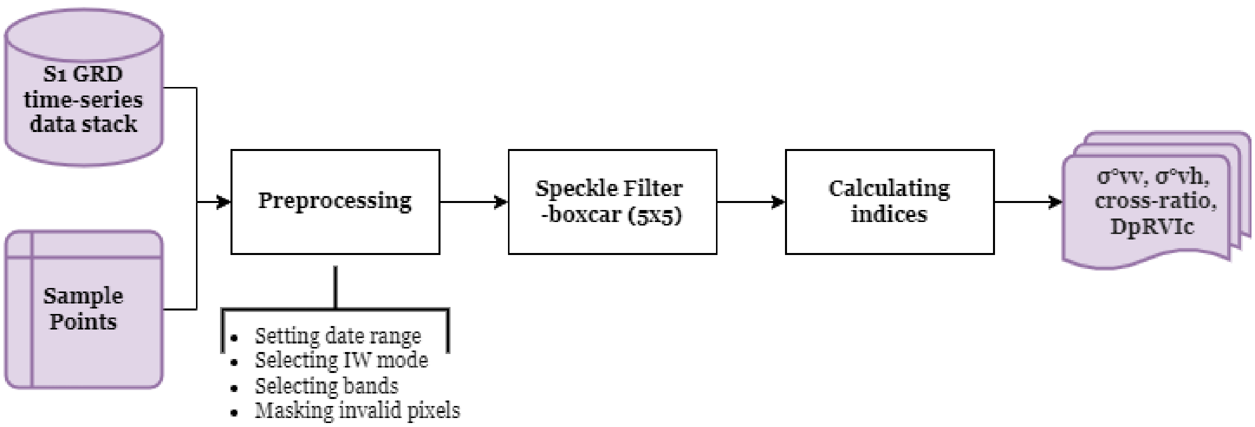

Figure 6: Sentinel-1 Data Preparation Workflow. The figure illustrates the main steps involved in preparing Sentinel-1 GRD time-series data for analysis. The process includes setting the date range, selecting IW mode, choosing specific bands, masking invalid pixels, applying a speckle filter, and calculating indices.

The Google Earth Engine platform was used to process Sentinel-1 GRD data, similarly as described by Bhogapurapu et al., (2021a). As shown in Figure 6, the sample points, as defined in Sub-Section 5.1.3 (Grid Definition), were utilized alongside the AOI's boundaries, covering a 5-year period from 2019 to 2023, to enhance dataset robustness (Bhogapurapu et al., 2021b). This period represents various field stages from bare soil to fully vegetated. An orbit selection was performed to standardize the datetime acquisition, extracting only measurements taken during the ascending orbit, which occurs in the late afternoon hours. This approach avoids dew effects commonly present in morning acquisitions from the descending orbit in this part of the planet (Jeu et al., 2005).

Moreover, invalid pixels—characterized by noise, sensor errors, or obstructions—were masked to ensure data quality. During preprocessing, georectification was performed to align the radar data with accurate geographic coordinates, ensuring that subsequent analysis is spatially accurate. The signal conversion from logarithmic to linear values was performed, when necessary, simultaneously with the application of a speckle filter. A moving window of 5x5 was used for the boxcar filter, which helps to reduce noise and improve the clarity of the signal. After preprocessing, various indices and descriptors were calculated to provide insights into vegetation morphology and soil moisture status. These include the co-pol purity parameter (*mc*), cross-ratio (*q*), and the Dual-pol Radar Vegetation Index (DpRVIc), which will be further explained in the following Sub-Sections.

Finally, the processed data, including the dual-polarimetric descriptors, were exported as Excel CSV files. This step ensured that the data could be easily accessed and analyzed in further steps.

5.1.5 Landsat 9 Data Preparation

The optical and thermal preprocessing were done in collaboration with constellr, a company specializing in Earth observation and remote sensing technologies, aiming to improve the quality of the thermal data used. Figure 7 describes the processes involved in applying a series of transformations to obtain surface reflectance and temperature values, as well as cloud and quality masks.

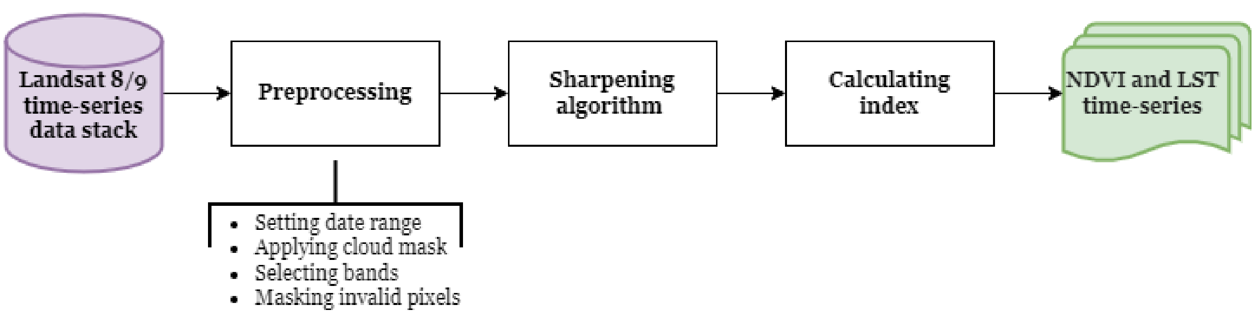

Figure 7: Landsat 8/9 Data Preparation Workflow. This figure outlines the primary steps in processing Landsat 8/9 time-series data. The process includes setting the date range, applying cloud masking, selecting bands, masking invalid pixels, applying a sharpening algorithm, and calculating indices.

The preprocessing pipeline comprises several key steps, which are general steps contained within constellr in-house algorithms. First, surface reflectance is derived from the Level 2 values using specific scaling factors provided in the Landsat 8-9 Collection 2 Level 2 Science Product Guide documentation. This involves applying a multiplication factor to the Level 2 values to convert them to surface reflectance based on predefined coefficients. Similarly, surface temperature is obtained by applying another transformation that converts the Level 2 values to temperature, using a different set of coefficients. Additionally, top of atmosphere (TOA) reflectance is calculated by adjusting the Level 2 values with multiplicative and additive scaling factors, and further normalizing these values by the sine of the sun elevation angle. TOA brightness temperature is obtained by converting the radiance values to temperature using thermal constants, which involves logarithmic transformations.

Quality assessment (QA) pixel masking involves deriving cloud and other quality masks from the QA pixel band using specific bitwise flags. Flags for dilated cloud, cirrus, cloud, and cloud shadow are applied to identify and mask out these conditions in the imagery. The combined cloud and quality masks are then applied to the reflectance and temperature bands, setting masked pixels to NaN. Images with a high proportion of masked pixels (greater than 90%) are discarded to ensure data quality.

Due to the nominal spatial resolution of 100 meters for Landsat's thermal bands (Niclòs et al., 2021), which results in a blur effect on the 30-meter spatial resolution optical bands, an in-house algorithm developed by constellr was employed. This algorithm, based on the works of Gao et al. (2012) and Guzinski et al. (2019), sharpens the thermal data to match the spatial resolution of the optical bands. The algorithm uses an ensemble of decision-tree regressors to establish statistical relationships between the low-resolution thermal infrared (TIR) data and the high-resolution shortwave reflectance data, effectively enhancing the spatial detail of the thermal imagery.

This preprocessing ensures that the data used in subsequent analyses is of high quality, with accurate surface reflectance and temperature values, and minimized cloud contamination. By replacing the Landsat resampling methodology with a method that better conserves the temperature signal when increasing the resolution, the preprocessing step further enhances the reliability of the data for analysis. As a last step, from the optical bands NDVI is calculated following Equation 1:

$$NDVI = \frac{(NIR - Red)}{(NIR + Red)} \tag{1}$$

After all this process, the final time-series dataset is ready to be integrated into the work's proposed model.

5.2 SAR-based Change Detection

The change detection approach using SAR data rests on several foundational assumptions. Firstly, it presumes that the primary source of variation in the backscattered radar signal is the local variation in soil moisture, and no other factors such as surface roughness or vegetation dynamics (Zribi et al., 2008). The usage of a radar vegetation index over the traditional NDVI mitigates issues related to cloud cover, which is a common problem in optical remote sensing. Radar sensors, unlike optical sensors, are not affected by cloud cover, making them more reliable for continuous monitoring. Gao et al. (2017) emphasize that the radar vegetation index provides a more robust dataset by reducing the influence of atmospheric conditions, which enhances the accuracy of soil moisture estimates.

Another critical assumption is the temporal stability of the radar signals' response to soil moisture changes. Bhogapurapu et al. (2021b) illustrate that by analyzing the difference in backscatter signals over time, the approach can effectively highlight soil moisture variations, assuming that other factors remain constant or are accounted for. This method relies on historical data to identify and subtract the driest signal observed for each cell, thus isolating the moisture-related changes. This temporal analysis is validated through comparisons with ground truth measurements and other models, demonstrating a strong correlation between the SAR-derived soil moisture estimates and actual soil moisture conditions (Zribi et al., 2008). Figure 8 provides a holistic view of the methodology:

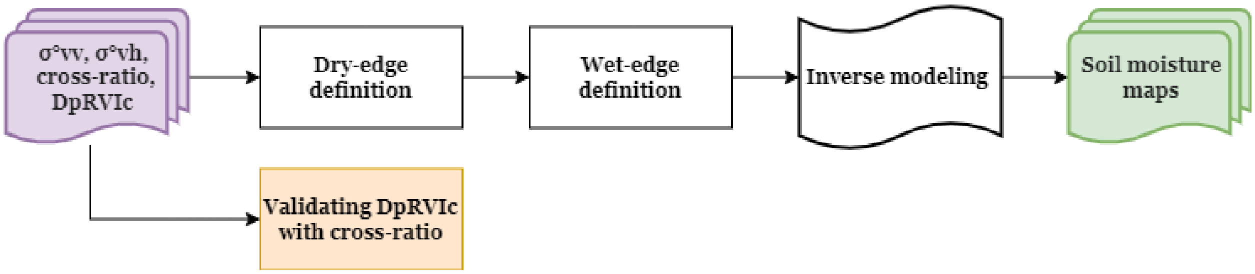

Figure 8: SAR-based Soil Moisture Estimation Workflow. The flowchart illustrates the steps used to generate soil moisture maps, beginning with the calculation of σ°VV, σ°VH, cross-ratio, and DpRVIc. The process involves defining dry and wet edges, applying inverse modeling, and validating DpRVIc using the cross-ratio as an auxiliary step.

Following, a precise explanation about the radar index and the soil estimation equations is given.

5.2.1 Radar Vegetation Index

Different SAR-derived vegetation descriptors have been used to characterize vegetation morphology, mainly based on the cross-ratio parameter (Della Vecchia et al., 2008; Homayouni et al., 2019; Vreugdenhil et al., 2018). When working with dual cross-polarimetric GRD SAR product, backscatter response can be obtained in $(\sigma°_{VV}, \sigma°_{VH})_{\mathrm{dB}}$ mode, considering a mono-static antenna configuration and a natural scene, $\sigma°_{VH} \leq \sigma°_{VV}$ can be assumed (Cloude, 2010). From that, the ratio parameter q can be expressed as seen in Equation 2. As an example, for full vegetated conditions in the field the ratio value is high.

$$0 \leq q = \frac{\sigma°_{\mathrm{VH}}}{\sigma°_{\mathrm{VV}}} \leq 1 \tag{2}$$

Bhogapurapu et al. (2021a) propose a vegetation index that is described by first exploring q purity, represented by m_c in Equation 3. In this context, for full vegetated conditions in the field, m_c is low and increases gradually with the field transforming into bare soil conditions.

$$m_{\mathrm{c}} = \frac{1 - q}{1 + q}, \quad 0 \leq m_{\mathrm{c}} \leq 1 \tag{3}$$

Moreover, the normalization of the co-polarization intensity parameter β_c can be expresses as Equation 4,

$$\beta_c = \frac{1}{1 + q}, \qquad 0.5 \leq \beta_c \leq 1 \tag{4}$$

Considering Equation 3 and Equation 4, the overall purity is given by the multiplication of m_c and β_c, and by calculating the unitary difference a quantitative measure of scattering randomness is obtained. This randomness can be linked to the presence of vegetation structures at various stages. From that, Equation. 5 shows the Dual-pol Radar Vegetation Index ($DpRVI_c$) which represents a quantification of the impurity in the co-polarization component of the scattered wave.

$$DpRVI_c = 1 - m_c\beta_c = \frac{q(q+3)}{(q+1)^2}, \qquad 0 \leq DpRVI_c \leq 1 \tag{5}$$

In practice, a naturally fully vegetated pixel would return a $DpRVI_c$ value close to 1, reflecting the high intense backscatter caused by the presence of vegetation.

After generating the filtered signals, cross-ratio, and $DpRVI_c$, all data were stored in tables to be further analyzed. The Preliminary Results under Sub-Section 6.1 presents valuable insights on the comparison of cross-ratio and $DpRVI_c$.

5.2.2 Soil Moisture Estimation

As stated in the beginning of Sub-Section 5.2, this change detection approach is based on the direct radar backscattered signal difference between subsequence dates. The changes in the backscatter signal can be defined as Equation 6:

$$\Delta\sigma = \sigma^{\circ}_{\mathrm{dB}} - \sigma^{\circ}_{\mathrm{dry}} = f(veg, \theta) \tag{6}$$

Through this equation, it is possible to derive the changes values, for each cell, by a subtraction operation between the signal being analyzed minus an estimation of the driest signal in the same cell, where $\Delta\sigma$ is a function of vegetation and soil moisture. This driest signal estimation is given by an interpolation, expressed as Equation 7:

$$\begin{aligned} \sigma°_{\text{dry}}\,(d) \;&=\; f\,(\sigma°_{\text{dry}}\,(d_{\text{k-1}}), \sigma°_{\text{dry}}\,(d_{\text{k}})),\;\; \text{if}\,(d < d_{\text{k}}\,) \\ \sigma°_{\text{dry}}\,(d) \;&=\; f\,(\sigma°_{\text{dry}}\,(d_{\text{k}}), \sigma°_{\text{dry}}\,(d_{\text{k+1}}),),\;\; \text{if}\,(d > d_{\text{k}}\,) \end{aligned} \tag{7}$$

If the day (*d*) is before the identified driest day (d_{k}) in the month (*k*), the driest signal is interpolated using a linear function (*f*) between the radar signal strengths of the driest day of the previous month ($\sigma°_{\text{dry}}$ $(d_{\text{k-1}})$,) and the driest day of the current month ($\sigma°_{\text{dry}}$ (d_{k})). On the other hand, If the day (*d*) is after the identified driest day (d_{k}) in the month (*k*), driest signal is interpolated using a linear function (*f*) between the radar signal strengths of the driest day of the current month ($\sigma°_{\text{dry}}$ (d_{k})) and the driest day of the next month ($\sigma°_{\text{dry}}$ $(d_{\text{k+1}})$).

This construction is used to reproduce a conceptual relationship, as explored by Ziribi et al. (2008) and Bhogapurapu et al. (2021b), between the change in the backscatter signal, soil moisture and vegetation, shown in Figure 9. It relies on the assumption that the variations in backscatter changes in time, observed between close days, decrease according to an increase in the vegetation development. Figure 9 shows the expected signal dynamics during the evolution of vegetation in the field, considering the dry reference (red line), which is defined by the dry signal estimated.

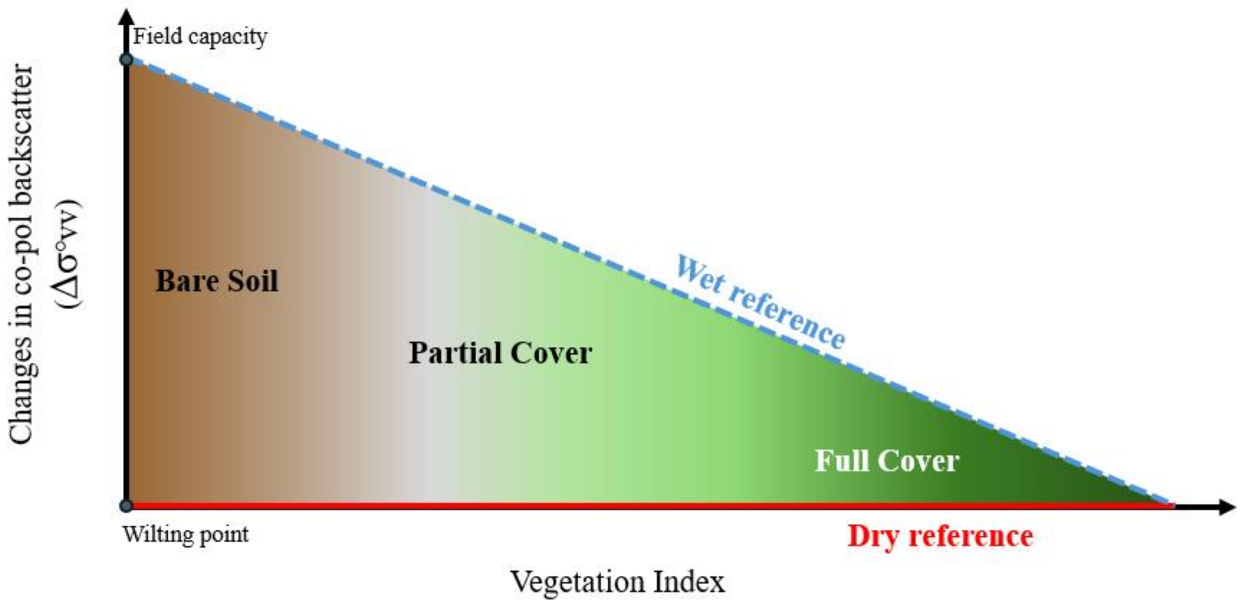

Figure 9: Relationship Between Vegetation Index and Changes in Co-Pol Backscatter. This diagram illustrates the relationship between the vegetation index and changes in co-polarized (co-pol) backscatter ($\Delta\sigma°vv$) for different ground conditions. The triangle is divided into three zones: Bare Soil, Partial Cover, and Full Cover. The vertical axis represents changes in co-pol backscatter, ranging from the wilting point to field capacity, while the horizontal axis represents the vegetation index, from the dry reference (low vegetation index) to the wet reference (high vegetation index). The gradient shading from brown to green indicates increasing vegetation cover, with corresponding changes in backscatter values. Adapted from Bhogapurapu et al. (2022).

The wet reference, on the other hand, is defined by the vegetation index. Previous studies as Ziribi et al. (2008) and Gao et al. (2017) already worked with the upper bound as a function of NDVI, considering, respectively, quadratic and linear functions to represent it. In the present work, aligned with the approach presented by Bhogapurapu et al. (2021b), a quadratic function of $DpRVI_c$ is utilized.

Now, from Figure 9 the upper bound (blue dashed line) is defined as Equation 8:

$$\Delta\sigma°_{max}(veg) = f(veg) + \Delta\sigma°(bare) \tag{8}$$

where $f(veg)$ is a function of the vegetation index ($DpRVI_c$), and $\Delta\sigma°(bare)$ is the maximum change in backscatter for bare soil surface. Finally, the relative surface soil moisture estimation can be expressed for each pixel (i,j) for a given time t and vegetation condition as Equation 9:

$$\Theta_{(i;j;t;veg)} = \frac{\Delta\sigma_{(i;j;t)}}{\Delta\sigma°_{\max}(veg)} \tag{9}$$

After the determination of the relative soil moisture for each pixel in different dates, the reconstruction of the maps was performed, representing volumetric soil moisture estimations.

5.3 Temperature-Vegetation Dryness Index (TVDI)

5.3.1 Standard TVDI

The underlying concept of TVDI is based on the observation that a scatter plot of remotely sensed surface temperature and NDVI often forms a triangular or trapezoidal shape (Carlson et al., 1994). The observed shape arises because vegetation cover and soil moisture affect surface temperature and reflectance differently. In general, areas with sufficient soil moisture and dense vegetation tend to have lower surface temperatures, which is connected to high evapotranspiration rates (de Tomás et al., 2014). In contrast, areas with low vegetation cover and low soil moisture tend to have higher surface temperatures.

As explored by Sandholt et al. (2002), the relationship between surface temperature and NDVI can be utilized for assessment of the soil moisture status. As indicated by Figure 10, the dry reference represents the maximum surface temperature for each NDVI value, indicating minimal soil moisture. Conversely, the wet reference represents the minimum surface temperature for each NDVI value, indicating sufficient soil moisture and high evapotranspiration.

TVDI requires spatial heterogeneity in vegetation and soil moisture conditions to correctly determine the dry and wet edges of the LST-VI scatterplot. This heterogeneity is challenging to ensure in small areas, leading to less accurate results. Additionally, its values are influenced by the density of vegetation. Densely vegetated areas typically exhibit lower TVDI values due to evaporative cooling effects, which reduces the index's range and resolution in these environments (Tang et al., 2010).

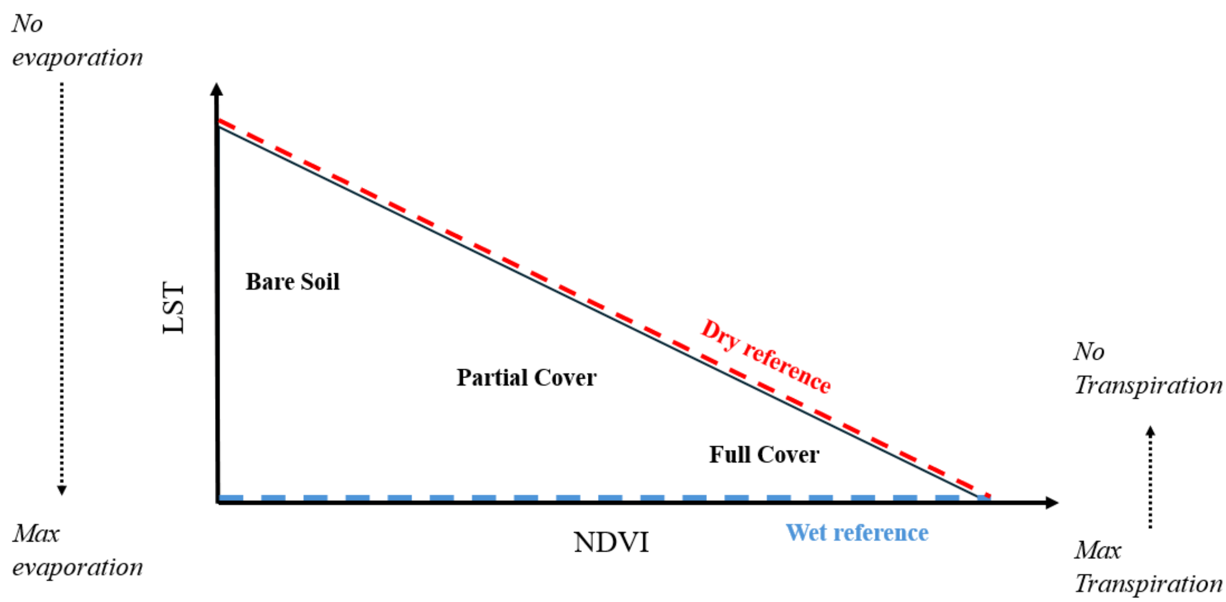

Figure 10: Relationship Between NDVI and LST with Evaporation and Transpiration Extremes. This diagram shows the relationship between the Normalized Difference Vegetation Index (NDVI) and Land Surface Temperature (LST) for different vegetation covers. The triangular area is divided into three zones: Bare Soil, Partial Cover, and Full Cover. The vertical axis represents LST, with the left side indicating evaporation (from no evaporation to maximum evaporation), while the horizontal axis represents NDVI, indicating transpiration (from maximum transpiration to no transpiration). The dry reference is indicated by a red dashed line, and the wet reference by a blue dashed line. The gradient shading illustrates changes in cover and associated evapotranspiration processes. Adapted from Sandholt et al., 2002.

Equation 10 for TVDI is defined as:

$$TVDI = \frac{LST - LST_{\min}}{a + bNDVI - LST_{\min}} \tag{10}$$

where, LST is the observed land surface temperature at a given pixel; NDVI is the normalized difference vegetation index; a and b are the intercept and slope of the dry reference calculated; and $LST_{\min}$ represents the wet reference located in the bottom limit of the scatterplot. This index ranges from 0 to 1, with values close to 0 indicating wet conditions and values close to 1 indicating dry conditions. Moreover, according to Wang et al. (2004), this range can be divided into five levels:

very wet (0.0 < TVDI≤0.2), wet (0.2 < TVDI≤0.4), water balanced (0.4 < TVDI≤0.6), dry (0.6 < TVDI≤0.8) and very dry (0.8 < TVDI≤1.0).

In the present work the following steps were undertaken to calculate the index:

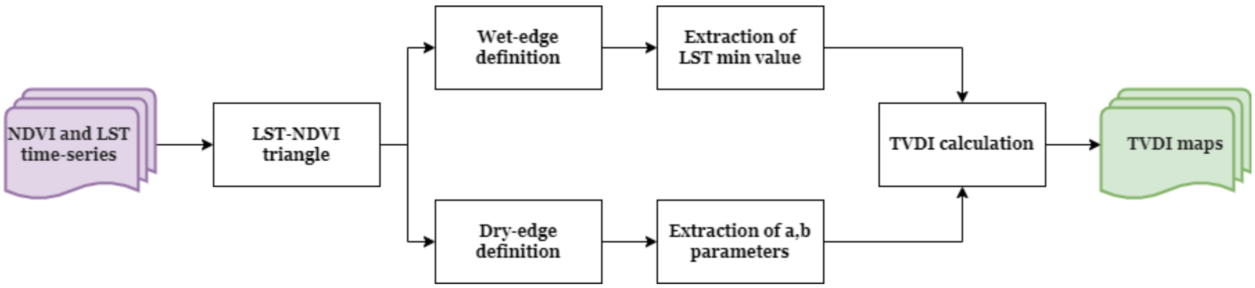

Figure 11: TVDI Methodology Workflow. The workflow begins with NDVI and LST time-series data, followed by the construction of the LST-NDVI triangle. It then defines the wet and dry edges, extracts the LST minimum value and the a,b parameters, and culminates in the calculation of TVDI to produce TVDI maps.

Figure 11 illustrates the step-by-step process involved in the calculation and mapping of TVDI. Both datasets, NDVI and LST, are crucial as they provide the necessary input variables for constructing the LST-NDVI space, which will be done for every day of data (e.g., for every day that we have NDVI and LST information, one triangle will be built). In this scatter plot, each point represents a pixel's LST and NDVI value.

The subsequent steps involve the definition of the dry and wet edges of the LST-NDVI triangle. To be able to define the dry edge, the whole range of NDVI values is divided equally into different subsets intervals of 0.01, and for each interval, the maximum value is selected, creating a cluster of points that will serve as input for a linear regression, which will provide $a + bNDVI$. The wet edge is calculated by averaging groups of points located in the lower limit of the scatterplot, taking the mean value.

With the parameters defined, the TVDI for each pixel is calculated using the Equation 10 and the pixels are reassembled creating the TVDI maps for each date where there is available data.

5.3.2 Temporal TVDI Modifications

Many authors suggested adaptations on the standard index to improve its results, or to extend its applications (Bian et al., 2023; Li et al., 2022; Rahimzadeh-Bajgiran et al., 2011). For the present work, aiming to improve the model's robustness and construct a temporal comparison between the different models, modifications proposed by Prześdziecki et al. (2023) is considered.

According to the authors, instead of relying on the spatial heterogeneity required by the index to access the variability required to define the dry and wet edges, it is proposed to use temporal variability of soil moisture conditions. This approach involves combining data from multiple satellite images taken at different times, representing a range vegetation stages, consequently a range of moisture conditions over the same area. In practice, this means that instead of creating an LST-NDVI space for each day, which wouldn't yield sufficient variability over a single field, a general scatterplot is generated, considering the entire time range. This temporal TVDI (tTVDI) model captures more variability, hence allows for a more accurate assessment of moisture conditions over time.

To accommodate the use of multiple scenes and ensure comparability across different dates, the authors replaced the LST with the difference between LST and air temperature (DT). This adjustment implements a specific type of normalization allowing a better comparison between different seasons, making the index more robust and applicable on a larger scale (Przeździecki et al., 2023).Even though Przeździecki et al. developed this approach specifically for forest areas, the principle of normalization for temporal comparison can still be applied to agricultural lands

Additionally, the authors experimented with using linear regression fit also for the wet edge of the scatterplot, in contrast to the group average suggested in the original version of the index. This modification induces the following adaptations of the main equations.

The dry edge is now based on the maximum DT, as expressed by Equation 11:

$$DT_{\max} = b_{\max} + a_{\max} NDVI \tag{11}$$

The wet edge is now based on a linear regression for the minimum values of DT, as expressed by Equation 12:

$$DT_{\min} = b_{\min} + a_{\min} NDVI \tag{12}$$

Resulting on the temporal TVDI model, described by Equation 13:

$$tTVDI = \frac{DT - DT_{\min}(NDVI)}{DT_{\max}(NDVI) - DT_{\min}(NDVI)} \tag{13}$$

Following the implementation of these modifications, normalized tTVDI maps were created for the different dates.

5.4 Qualitative Analysis

In addition to the model definition presented previously, a comprehensive qualitative analysis was conducted focusing on the behavior comparison between the different soil moisture estimations. This qualitative analysis aimed to identify and describe the relationships among the various estimations, providing deeper insights into their interdependencies and potential patterns. By examining the qualitative trends and associations, the study ensured a thorough exploration of the data, highlighting significant qualitative relationships and potential areas for further investigation.

First, the variation in soil moisture estimations over time is examined using a comprehensive time series approach. For that, the median value for the AOI was used to analyze temporal variability, providing a robust measure unaffected by outliers and extreme values, allowing for a clearer understanding of typical patterns over time (Rousseeuw and Hubert, 2018). The SAR-based soil moisture estimation, tTVDI, and GPR data are indexed and processed to align their timestamps, allowing for accurate chronological comparison. There are two specific matching dates between the SAR dataset and GPR acquisitions, which are August 25th, 2023, and September 11th, 2023. However, there is only one matching date between the optical/thermal dataset and GPR, which is September 11th, 2023, imposing limitations on the comparison. The field precipitation data is integrated into the analysis and used as a proxy, producing a multi-dimensional view of soil moisture variation. Additionally, due to the short date range for the GPR measurements, a wider temporal analysis, comprehending two years is integrated, using the precipitation data to analyze the models' sensitivity.

In addition to the temporal analysis, the spatial variation between TVDI and SAR-based estimations is also examined. By selecting the matching dates where there are both results, it is possible to identify patterns, discrepancies, and relationships in soil moisture distribution on the field, enhancing the overall understanding of spatial variability in soil moisture dynamics captured by the different models.

Finally, aiming to support the qualitative approach, the correlation between the different results were calculated. First, the Spearman correlation coefficient was selected to relate the soil moisture estimations, as it captures both linear and non-linear monotonic relationships, and is more reliable than other correlation methods when sample sizes are small, and data may not meet the assumptions required by different methods (Schober and Schwarte, 2018). Additionally, a comparison of the two models against precipitation was done, similarly as done by Zribi et al. (2008), where the occurrence or absence of precipitation was analyzed in specific results thresholds.

6 Results

In this Section, a comprehensive overview of the findings is presented, divided into two key parts: preliminary and main results. Sub-Section 6.1 (Preliminary Results) focuses on the intermediate steps of each previously described methodology, providing a detailed overview of the progress and partial outcomes observed during the data processing and analysis phases. Examining these middle steps allows for a better understanding of the intricacies and interim results that contribute to the final conclusions of the study.

Sub-Section 6.2 (Main Results) delves into the final outcomes of the analyses, including both spatiotemporal variations in soil moisture estimations. By integrating these comprehensive analyses, Section 6 offers a thorough understanding of the dynamics and patterns in soil moisture.

6.1 Preliminary Results

6.1.1 Radar Vegetation index

To verify $DpRVI_c$ behavior throughout the date range, a time-series was plotted comparing the original polarizations and its cross-ratio q. Figure 12 and Figure 13 display the mean plot for all pixels within the AOI:

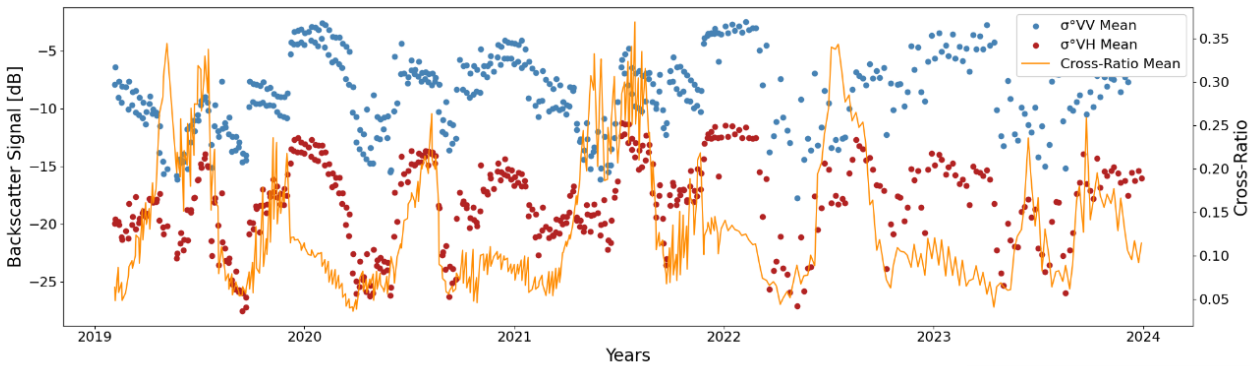

Figure 12: Cross-ratio visualization in comparison to backscatter signals from 2019 to 2023, mean representation for all pixels in the AOI.

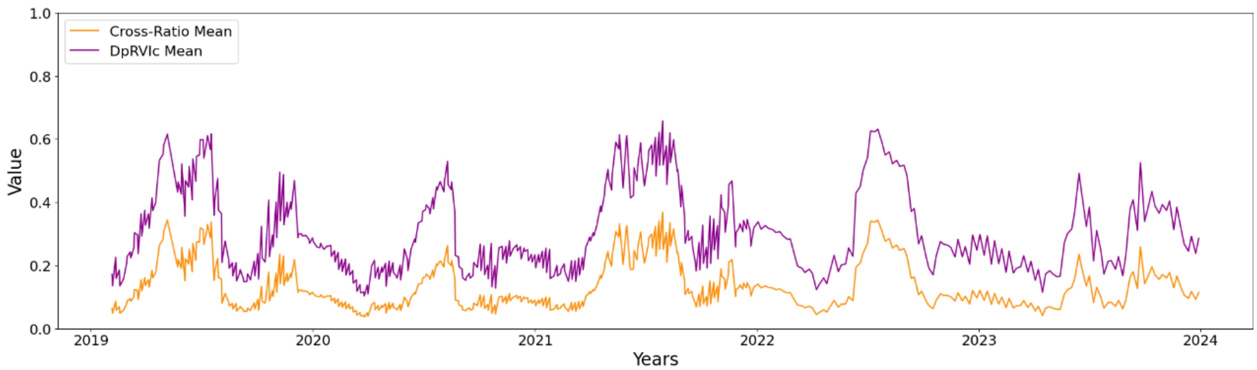

Figure 13: Cross-Ratio visualization in comparison to $DpRVI_c$ from 2019 to 2023, mean representation for all pixels in the AOI.

Figure 12, illustrates the mean cross-ratio in comparison to mean backscatter signals (σ°VV and σ°VH) from 2019 to 2023 for all pixels within the AOI. The x-axis represents the years, spanning from 2019 to 2024, while the y-axis on the left measures the backscatter signal in decibels (dB), and the y-axis on the right measures the cross-ratio value. Blue dots denote the σ°VV (vertical transmit, vertical receive) backscatter signals, and red dots represent the σ°VH (vertical transmit, horizontal receive) backscatter signals. The orange line displays the cross-ratio over time. The graph shows that both σ°VV and σ°VH backscatter signals exhibit fluctuating patterns, indicating varying backscatter characteristics over the period. Simultaneously, the cross-ratio also shows significant variation, with notable peaks and troughs that may correlate with changes in the backscatter signals. These fluctuations highlighting the dynamic nature of the radar backscatter characteristics in the AOI.

Figure 13, compares the mean cross-ratio with the mean $DpRVI_c$ index over the same time period, from 2019 to 2023, for all pixels in the AOI. The x-axis covers the years 2019 to 2024, while the y-axis measures a unitless value for the indices compared. The orange line represents the cross-ratio, and the purple line represents the $DpRVI_c$. Both indices exhibit fluctuating patterns over the years, indicating temporal variability in the radar-derived metrics. The graph shows that there are instances where peaks and troughs in $DpRVI_c$ correspond with those in the cross-ratio, suggesting a potential relationship between these indices. The simultaneous variations in both indices imply that the $DpRVI_c$ and the cross-ratio may respond similarly to underlying environmental or radar signal changes within the AOI. This comparative analysis underscores the importance of examining multiple radar-derived metrics to better understand the dynamic behaviors and interactions in the observed data.

6.1.2 SAR-based change detection - Dry edge

The following graph shows the time series of radar backscatter signals and their estimated driest signals, derived through an interpolation method. This approach calculates changes in the radar signal by subtracting the estimated driest signal from the observed signal, capturing variations due to vegetation and soil moisture dynamics. The red line represents the interpolated driest signal, that repeats itself yearly. It constitutes a baseline to highlight significant changes in the radar data over time.

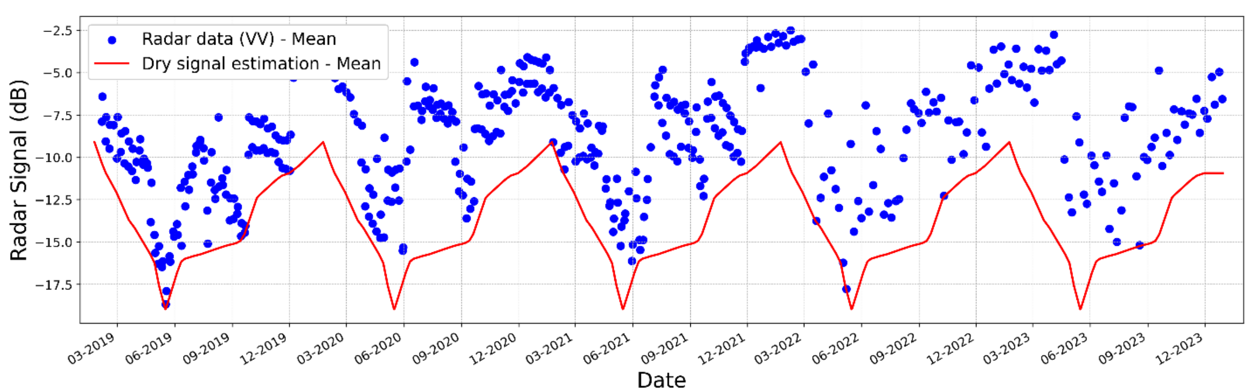

Figure 14: Mean representation of the dry signal from 2019 to 2023 for all pixels within the AOI.

Figure 14 presents a time series analysis of radar backscatter signals ($\sigma°VV$) and their estimated driest signals over a period from early 2019 to late 2023. The x-axis represents the date, ranging from March 2019 to December 2023, providing a temporal context for the radar observations. The y-axis indicates the radar signal strength in decibels (dB), spanning from -20 dB to -2.5 dB.

The blue dots depict the actual radar backscatter signal values (σ°VV) recorded at various dates. These values fluctuate significantly over time, reflecting variations likely due to changes in vegetation and soil moisture. The red line illustrates the estimated driest signal (σ°dry), which is derived through an interpolation method described previously. In practice, the driest signal is estimated for each day, and for the same day in different years the value is repeated throughout the entire date range.

6.1.3 SAR-based wet edge definition

Through the scatterplot between the changes in co-polarization backscatter (*Δσ°VV*) and DpRVIc, the conceptual relationship showed in Figure 9, is created. In the present work, as stated in the methodology Sub-Section 5.2.2, a quadratic function is selected to define the wet reference, as demonstrated by Bhogapurapu et al. (2021b).

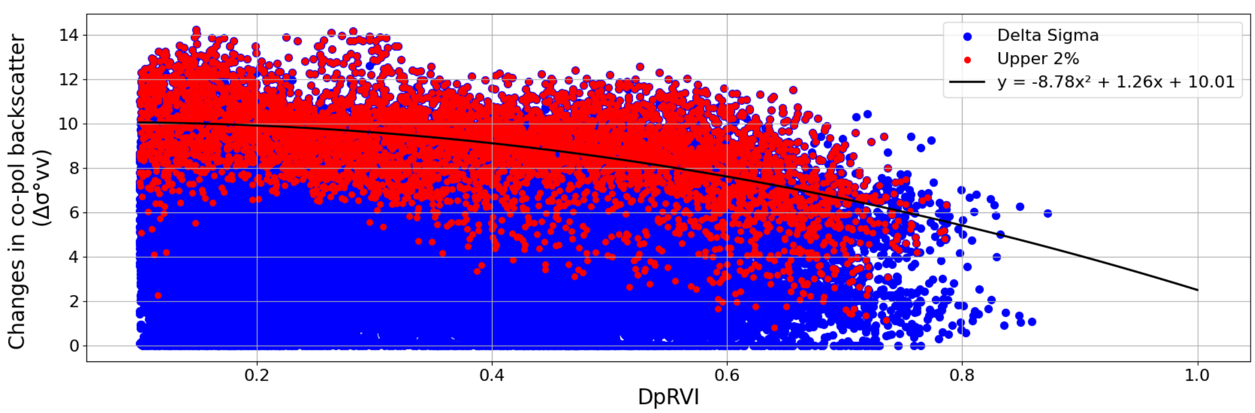

Figure 15: Relationship Between Differential Polarimetric Vegetation Index (DpRVIc) and Changes in Co-Pol Backscatter (Δσ°vv). The scatter plot shows the relationship between DpRVIc and changes in co-polarized (co-pol) backscatter (Δσ°vv). Blue dots represent the general dataset, while red dots highlight the upper 2% of the data points. The black curve represents the quadratic regression model fitted to the red dots.

Figure 15 demonstrates how backscatter variations, observed between close days, decrease with increasing vegetation development. The x-axis denotes the DpRVIc values, ranging from 0 to 1, where higher values correspond to denser vegetation. The y-axis measures changes in co-polarization backscatter (Δσ°VV) in decibels (dB), spanning from 0 to 14 dB. The blue dots on the graph depict the observed backscatter signal changes between consecutive days. These variations tend to decrease as DpRVIc increases, indicating more substantial vegetation cover. The red dots highlight the upper 2% of these changes, focusing on extreme values where the backscatter signal exhibits significant fluctuations. The black curve represents the quadratic function, presented in Equation 14:

$$y = -8.78x^2 + 1.26x + 10.01 \tag{14}$$

modeling the upper bound of the backscatter changes as a function of DpRVIc. This curve shows how the backscatter signal's dynamics evolve through different stages of vegetation growth. As DpRVIc increases, the quadratic model suggests a continuous decline in backscatter change, aligning with theoretical expectations that denser vegetation reduces backscatter variations. This detailed representation helps in understanding the interaction between soil moisture, vegetation development, and radar backscatter signals, as its changes decrease with the increase in vegetation density.

6.1.4 TVDI: LST-NDVI triangle space

In this Sub-Section, we present the initial findings of our analysis, focusing on the construction of the LST-NDVI triangle space. The methodology outlined previously allows us to generate a distinct triangle for each day, effectively capturing the relationship between LST and NDVI. This daily construction enables a dynamic and comprehensive assessment of soil moisture conditions across different vegetation covers. The following image exemplifies the LST-NDVI triangle space for four different days, demonstrating the typical formation of the dry and wet edges, which are crucial for subsequent TVDI calculations. These specific days were selected to demonstrate TVDI behavior across sequential dates. However, it is important to note that this behavior may vary on different days in other seasons.

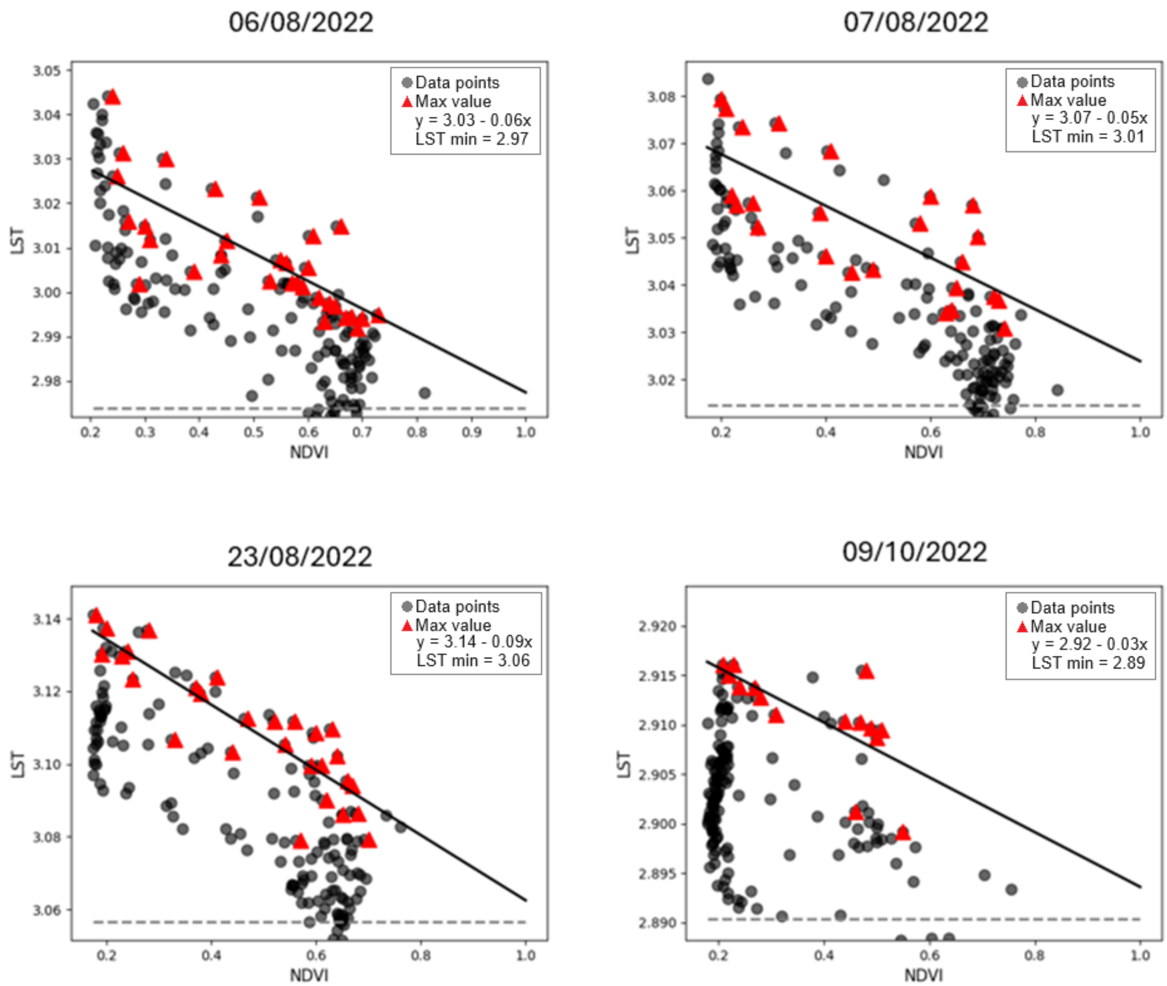

Figure 16:LST-NDVI triangle space for four different dates. Data points are represented by grey circles. The maximum values used to create the dry edge are represented by red small triangles.

Figure 16 illustrates the LST-NDVI triangle space for four distinct dates: 06/08/2022, 07/08/2022, 23/08/2022, and 09/10/2022. The red triangles represent the values considered for the establishment of the dry edge, where the maximum LST values for each NDVI are observed, indicating areas of minimal soil moisture. The grey circles denote data points, and the dashed line is created through the averaging of 15 minimum values. The LST values on the y-axis are presented divided by a hundred in order to be scalable. The x-axis is NDVI values ranging from 0.2 to 1.0.

On 06/08/2023, the scatter plot shows a well-defined triangular shape with LST values ranging from approximately 2.97 to 3.05. The linear regression line, defined by Equation 15:

$$y = 3.03 - 0.06x \tag{15}$$

with an intercept of 3.03 and a slope of -0.06, highlights the temperature gradient across the NDVI values. The minimum LST value is 2.97.

The triangle space for 07/08/2023 displays a similar pattern to the previous day, with LST values ranging from approximately 3.01 to 3.08. The regression line for this day is presented by Equation 16:

$$y = 3.07 - 0.05x \tag{16}$$

with an intercept of 3.07 and a slope of -0.05, indicating a slightly less steep gradient compared to 06/08/2023, due to more sparse maximum values in the LST range. The minimum LST value for this day is 3.01, suggesting a slight increase in overall moisture conditions.

On 23/08/2023, the scatter plot continues to exhibit the triangular shape, with LST values spanning from approximately 3.06 to 3.14. The distribution of points indicates a slight shift, with the regression line defined by Equation 17:

$$y = 3.14 - 0.09x \tag{17}$$

This regression equation, with an intercept of 3.14 and a slope of -0.09, shows a steeper gradient than the previous dates, reflecting higher temperature captured on the day, fore pixels closer to bare soil stage. The minimum LST value is 3.06, indicating a probability of wetter conditions compared to the earlier dates.

The scatter plot for 09/10/2023 presents a slightly different pattern, with LST values ranging from approximately 2.89 to 2.92. The triangular shape is still evident, although the distribution of points appears more clustered towards lower NDVI values. The regression line for this day is expressed by Equation 18:

$$y = 2.92 - 0.03x \tag{18}$$

with an intercept of 2.92 and a slope of -0.03, lower general temperature and a concentration of pixels indicating bare soil stage on the field.

This first analysis highlights the fact that each day is producing its own triangle space for the TVDI calculation and reinforces the necessity of performing the tTVDI, in order to visualize the variation in the temporal dimension.

6.1.5 Temporal TVDI: LST-NDVI triangle space

This Sub-Section focuses on the results of temporal modifications to the standard TVDI methodology. This approach leverages the temporal variability of soil moisture conditions, enabling a more accurate and comprehensive assessment. The following Figure 17 exemplifies the general DT-NDVI triangle space, illustrating how the integration of multiple scenes enhances the robustness of the model.

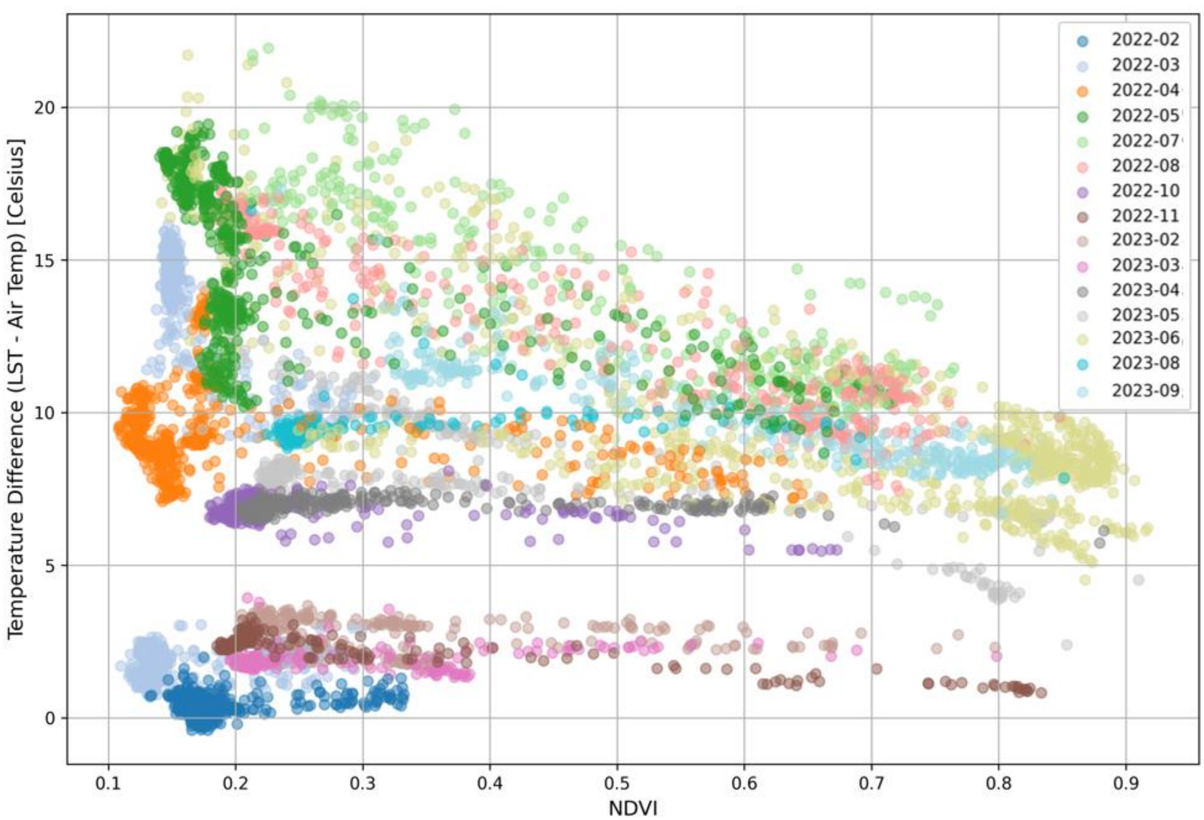

Figure 17: Relationship Between NDVI and Temperature Difference (LST - Air Temperature) Over Time. This scatter plot illustrates the relationship between the Normalized Difference Vegetation Index (NDVI) and the

temperature difference (Land Surface Temperature (LST) minus Air Temperature) across various months from February 2022 to September 2023. Each color represents data from a different month, as indicated in the legend. The data points show seasonal variations, with higher NDVI values generally associated with lower temperature differences, indicating the influence of vegetation cover on temperature regulation.

Figure 17 shows the scatter plot for all NDVI and LST pixels throughout the period analyzed, grouping data by different month-year combinations, each represented by a distinct color. The month-year combinations include 2022-02 (blue), 2022-03 (light turquoise), 2022-04 (orange), 2022-05 (dark green), 2022-07 (light green), 2022-08 (salmon), 2022-10 (purple), 2022-11 (brown), 2023-02 (light brown), 2023-03 (pink), 2023-04 (dark grey), 2023-05 (light grey), 2023-06 (olive), 2023-08 (cyan), and 2023-09 (light blue). The X-axis represents the NDVI values, which range from 0 to 1. The Y-axis shows the difference between LST and the air temperature, measured in degrees Celsius. This difference, referred to as DT, highlights the deviation of the land surface temperature from the surrounding air temperature.

It reveals clear seasonal patterns in the DT vs. NDVI relationship. For instance, data points from the colder months, such as February 2022/2023 and November 2022, tend to cluster at lower DT values, suggesting less deviation of surface temperature from air temperature. Conversely, data from warmer months, such as June 2022/2023 and August 2022/2023, show higher DT values, indicating greater differences between surface and air temperatures.

In general, there is a noticeable trend where higher NDVI values, indicating denser vegetation, correspond to lower DT values. This pattern aligns with the understanding that denser vegetation often leads to cooler surface temperatures due to higher evapotranspiration rates. The plot demonstrates temporal consistency in the data. Despite the variability in temperature differences across months, the overall pattern of lower DT values with higher NDVI remains consistent. This consistency supports the robustness of the temporal TVDI model in capturing soil moisture conditions over different periods.

The plot also reveals that months like February 2022 and November 2022 show low DT values even at low NDVI, indicating that during colder periods, even less vegetated areas do not experience high surface temperature deviations. On the other hand, during warmer months like June 2022 and August 2022, even high NDVI areas can show elevated DT values, though generally, high NDVI still moderates these values.

Figure 17 also highlights periods of extreme temperature differences. For instance, July 2022, June 2023 exhibit some of the highest DT values, suggesting significant heating of the land surface relative to the air temperature during these months. This could be indicative of periods of drought or heat waves, as supported by the high air temperature values shown in Figure 4 for these periods, which reduce soil moisture and increase surface temperatures.

This first analysis over the general scatterplot paves the way for performing the dry and wet edges definition.

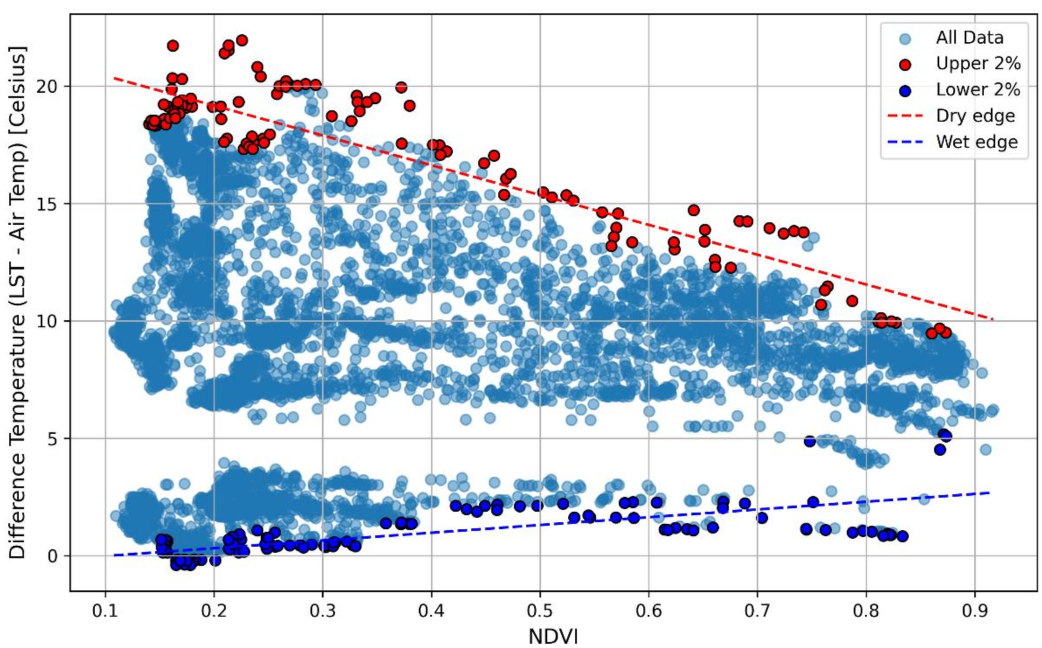

Figure 18: Relationship Between NDVI and Temperature Difference (LST - Air Temperature) with Dry and Wet Edges. This scatter plot depicts the relationship between the NDVI and the temperature difference in degrees Celsius. The light blue dots represent all data points, while the red and blue dots highlight the upper 2% and lower 2% of the data, respectively. The red dashed line represents the dry edge, showing the upper boundary of the data, and the blue dashed line represents the wet edge, showing the lower boundary. These edges illustrate the extremes of temperature differences associated with varying levels of vegetation cover.

Figure 18 provides a detailed visualization of the relationship between NDVI and DT. This analysis is crucial for defining the dry and wet edges necessary for the tTVDI calculations. The plot consists of three key data groups: all NDVI-LST pixels throughout the period analyzed (light blue dots) representing the general relationship between NDVI and temperature difference, the upper 2% of data points in terms of temperature difference (red dots) forming the dry edge, and the lower 2% of data points (blue dots) forming the wet edge.

The general distribution of all data points shows a broad scatter with a noticeable trend: higher NDVI values are generally associated with lower temperature differences. The red dots (upper 2% values of the temperature difference) are scattered towards the higher end of the temperature difference scale, indicating areas with minimal vegetation (low NDVI) and high temperature differences, representing dry conditions. The red regression line fitted to these points slopes downward, illustrating that as vegetation density increases, the maximum temperature difference decreases. Conversely, the blue dots (lower 2% values of the temperature difference) are clustered at the lower end of the temperature difference scale. The blue regression line slopes upward, albeit more gently, reflecting minimal variations in temperature difference even in densely vegetated areas. From Figure 18 is possible to derive the following linear functions:

Dry-edge, expressed by Equation 19:

$$y = -12.69x + 21.70 \tag{19}$$

Wet-edge equation, expressed by Equation 20:

$$y = 3.30x - 0.35 \tag{20}$$

This analysis provides the necessary parameters for performing the calculation of the tTVDI model.

6.2 Main Results

This Sub-Section presents a comprehensive analysis of the principal findings from the study, focusing on the spatiotemporal variability of soil moisture estimations. Therefore, the main results are divided into two key parts: the temporal variability, which examines the changes in soil moisture over time using the proposed methodologies, and the spatial variability, which compares the distribution of soil moisture over the studied field.

6.2.1 Temporal variability

The temporal variability Sub-Section explores the changes in soil moisture over time by analyzing data from the SAR-based soil moisture estimations, optical/thermal-based tTVDI, and GPR-based soil moisture estimations. By aligning the timestamps of these datasets and incorporating precipitation records, we provide a detailed examination of soil moisture trends. This analysis aims to highlight the dynamic nature of soil moisture through time, exploring how different estimation techniques capture these variations across multiple seasons and years. Is important to emphasize that for the temporal analyses, only tTVDI is being considered for the thermal based approach. Moreover, median values for the field are selected as they provide a more robust representation of the data, minimizing the impact of outliers on the analysis (Kwak and Kim, 2017).

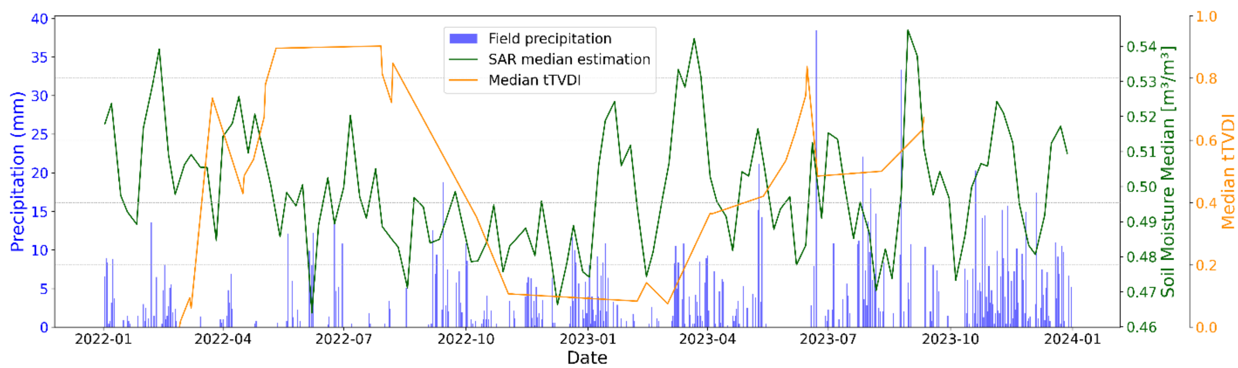

Figure 19: Comparative time series of precipitation, SAR-based soil moisture, and tTVDI. This multi-variable time series graph displays field precipitation (mm) in blue, SAR-based soil moisture median estimation (m^3/m^3) in green, and the median tTVDI in orange from January 2022 to January 2024. The precipitation data shows the daily rainfall events, while the SAR estimation indicates the field-median volumetric soil moisture, and the tTVDI values reflect the dryness of vegetation. The interplay between these variables highlights the impact of precipitation on soil moisture levels and vegetation dryness over time.

Figure 19 represents the integration of the results over the period of 2 years. The x-axis represents the date spanning from January 2022 to the end of December 2023, while the y-axes on the left and right sides correspond to precipitation in millimeters (mm) and volumetric soil moisture/tTVDI values, respectively. The blue bars represent the daily field precipitation, with values reaching up to 40 mm. The green indicates the SAR-based volumetric soil moisture field median for all pixels, ranging from 0.46 to 0.54, and the orange line shows the median tTVDI values, ranging from 0 to 1.

Regarding the SAR-based estimations, the data reveal notable seasonal patterns, with peaks and troughs corresponding to different times of the year. This trend shows periods of increased soil moisture, due to precipitation. On the other hand, the lowest values are observed during the summer months, indicating periods of reduced soil moisture. This is due to higher evapotranspiration rates, supported by Figure 25 in the Appendix which shows the median NDVI for the AOI, presenting high values during summer.

The SAR-based time-series also highlights the inter-annual variability in the median soil moisture estimations. In 2023, there are more pronounced fluctuations with higher peaks and deeper troughs compared to 2022. This variability indicates that soil moisture conditions were more extreme in 2023, reflecting the influence of differing climatic conditions (e.g. more precipitation events) and land management practices between the two years. Moreover, the graph shows the model's capability to capture both short-term and long-term variations in soil moisture.

Overall, the SAR-based estimation generally exhibits a similar pattern with precipitation events. This corresponding behavior is evident as peaks in soil moisture values often follow periods of significant rainfall. For example, substantial increases in soil moisture are observed in early 2022, mid-2022, and mid-2023, aligning with higher precipitation levels. For the 2 years being analyzed, it has been computed that 75.86% of SAR-based soil moisture values higher than 0.51 m^3/m^3 correspond to precipitation events that occurred on the same or previous day. On the other hand, 60% of the estimations, lower than 0.49 m^3/m^3, correspond to an absence of precipitation during the previous two days. These results demonstrate a good degree of correlation between precipitation and variations in SAR-based soil moisture estimations.

Regarding the tTVDI time-series, Figure 19 shows its values exhibit substantial fluctuations, with noticeable peaks and troughs over the observed period. For instance, there is a sharp increase in the index values from March to May 2022, followed by a plateau during the summer months. This is indicative of increasing dryness conditions, due to reduced soil moisture and higher evapotranspiration rates during the warmer season.

One of the notable aspects of this result is the irregular frequency of data points, which can be attributed to the influence of cloud cover. This approach relies on optical and thermal satellite data, which are susceptible to interference from clouds. Consequently, there are fewer data points available for it when compared to the SAR dataset, which is not affected by cloud cover. This discrepancy in data availability results in significant gaps in the temporal coverage, particularly evident during certain periods. For example, there is a notable gap between September 2022 and January 2023, followed by another period with sparse data points until March 2023. These gaps lead to large and abrupt differences in tTVDI values, highlighting the impact of limited data availability due to cloud cover. This effect is particularly evident in the early months of 2023, where the tTVDI values remain relatively low and stable until a sharp increase is observed in March 2023.

Overall, the pattern of tTVDI values aligns with expected seasonal variations in soil moisture and vegetation dryness. Higher tTVDI values during the summer months correspond to drier conditions, while lower values in the autumn and spring reflect wetter conditions with increased soil moisture. The tTVDI time-series shows a divergent behavior when compared to precipitation, reflecting its role in highlighting dryness. Higher tTVDI values, indicative of drier conditions, are typically observed during periods of low precipitation. For instance, the tTVDI peaks around mid-2022 and mid-2023 correspond with lower precipitation periods, emphasizing increased dryness during these times. In contrast, tTVDI values drop during wetter periods, such as early 2022 and early 2023, indicating reduced dryness due to higher soil moisture. For the 2 years being analyzed, it has been computed that 92.86% of tTVDI values higher than 0.6 correspond to an absence of precipitation during the previous two days. However, only 45.45% of tTVDI values lower than 0.4 correspond to precipitation events that occurred on the same or previous two days, which reflect the absence of proper data due to clouds in rainy periods.

The largest peak of precipitation occurs on June 22nd, 2023, with levels reaching nearly 40 mm. This significant rainfall event provides an excellent opportunity to observe how both approaches respond to substantial changes in moisture input. The peak follows an intense drought period from May 16th to June 17th, during which no precipitation was detected in the field. On June 18th and 20th, minor precipitation events of 2.8 mm and 7.9 mm, respectively, precede the main rainfall event. During this time, the SAR-based models show an increase in soil moisture from approximately 0.48 m^3/m^3 to 0.51 m^3/m^3. However, on June 21st, a day without precipitation, the soil moisture level dropped again, indicating that the soil's water content was still low and damaged from the drought period. Consequently, when the principal rainfall event occurs, the soil moisture increases, but does not exhibit, as significant increase as the event, highlighting the lingering effects of the prolonged drought.

In convergence, the tTVDI reaches one of its highest values just before the precipitation event, indicating extreme dryness. After the rainfall, the tTVDI decreases by 0.2, reflecting a reduction in water stress and improved moisture conditions.

The confirmed expectations of correlation with precipitation allow us to proceed with the analysis by incorporating GPR estimations. However, since GPR data was collected over a relatively short period, it limits the duration of the comparison, particularly affecting the tTVDI time series, which is already constrained by cloud cover. This limitation impacts our ability to perform a comprehensive long-term analysis, especially for the tTVDI, as its data points are fewer and more sporadic due to weather conditions.

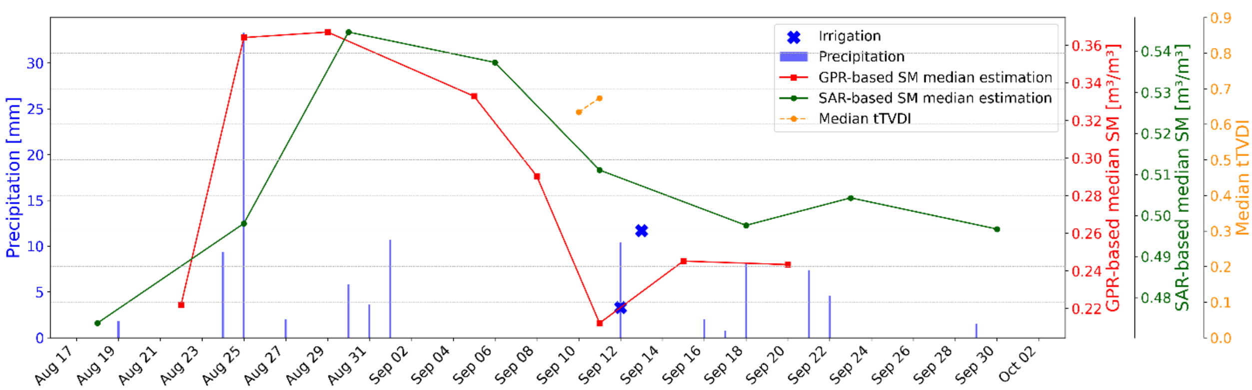

Figure 20: Comparative time series of irrigation, precipitation, SAR and GPR-based soil moisture, and tTVDI. This multi-variable time series graph displays data from August 17, 2023, to October 2, 2023. The graph includes irrigation events (blue crosses), precipitation (mm) shown as blue bars, field-median soil moisture estimated by GPR for the top 40 cm of soil (m^3/m^3) shown in red, field-median soil moisture estimated by SAR (m^3/m^3) shown in green, and the tTVDI shown in orange. The left y-axis represents precipitation, while the right y-axis represents soil moisture estimations and tTVDI.

Figure 20 presents the models comparison taking GPR-based estimations as the reference. The x-axis represents the date, covering from August 17th to October 1st, 2023. The left y-axis indicates precipitation in millimeters (mm), while the right y-axes show field-median volumetric soil moisture, for the top 40 cm of soil in the case of GPR-based estimation and for the top 10 cm for the SAR-based estimations. Besides that, the y-axes on the right also show tTVDI values.

The curve, depicted in red, shows that initially, on August 22nd, the soil water content is around 0.22 m^3/m^3. Following this, there is a sharp increase observed on August 25th, where the soil moisture peaks at approximately 0.36 m^3/m^3. This significant rise is aligned with a big precipitation event. After reaching its peak, the soil moisture begins to decline steadily. By September 5th, the value drops to about 0.33 m^3/m^3, continuing its descent to around 0.27 m^3/m^3 by September 9th. This decreasing trend indicates a reduction in soil moisture, aligned with a period without precipitation or irrigation. Interestingly, there is a slight recovery observed on September 13th, where the soil moisture increases marginally to about 0.25 m^3/m^3, reflecting the occurrence of precipitation and irrigation. However, this increase is not sustained, as the value stabilizes and slightly decreases again towards the end of the period, reaching approximately 0.24 m^3/m^3 on September 20th.

Both the SAR-based and GPR-based soil moisture estimations demonstrate good agreement over this short period, although SAR is sensitive to the few top cm of the soil while the used GPR is sensitive to the top 40 cm of the soil (wavelengths approximately 50 times larger for GPR compared to SAR). Both datasets indicate similar trends, with peaks and troughs occurring at corresponding times. This alignment suggests that both methods are capturing the soil moisture dynamics consistently, enhancing the reliability of the results. Supporting these findings, the spearman correlation calculated between SAR-based and GPR-based estimations gave a coefficient of 0.78 with a p-value of 0.02. It indicates that there is a strong positive monotonic relationship, which is statistically significant.

Moreover, there are significant precipitation events on August 25th and 29th, which correspond to increases in soil moisture levels in both the SAR and GPR datasets. Following these precipitation events, the soil moisture levels show a decline as expected, reflecting drying conditions. Irrigation events on September 6th and 12th are also critical to note. These events likely contributed to the stabilization of soil moisture levels during periods without significant rainfall.

The tTVDI values, represented by orange dots, are sparse due to the limited availability of optical/thermal data. This scarcity restricts the ability to perform a more robust comparison of soil moisture conditions over the period.

6.2.2 Spatial variability

This Sub-Section examines changes in soil moisture across the field by comparing results from three different estimation techniques: the SAR-based method, the optical/thermal-based TVDI, and GPR soil moisture estimations. Each method provides results with different sensitivities with respect to depth, highlighting the dynamic nature of soil moisture within the AOI and demonstrating how each method captures these variations differently. For this spatial comparison, we use the standard TVDI, which better represents the daily non-scaled index value. Due to limited matching dates between datasets, we compare SAR-based and GPR-based estimations on August 25th and September 11th, 2023. Only September 11th, 2023, serves as the common date for TVDI and GPR-based estimation, consequently allowing a comparison between the three results. We begin with an analysis of GPR-based soil moisture estimation.

As mentioned in Sub-Section 5.1.3 (Grid definition), to compare with the satellite data, the initial high-resolution soil moisture maps created with GPR were aggregated to match the coarser resolution of the models' results. Below are the specific maps:

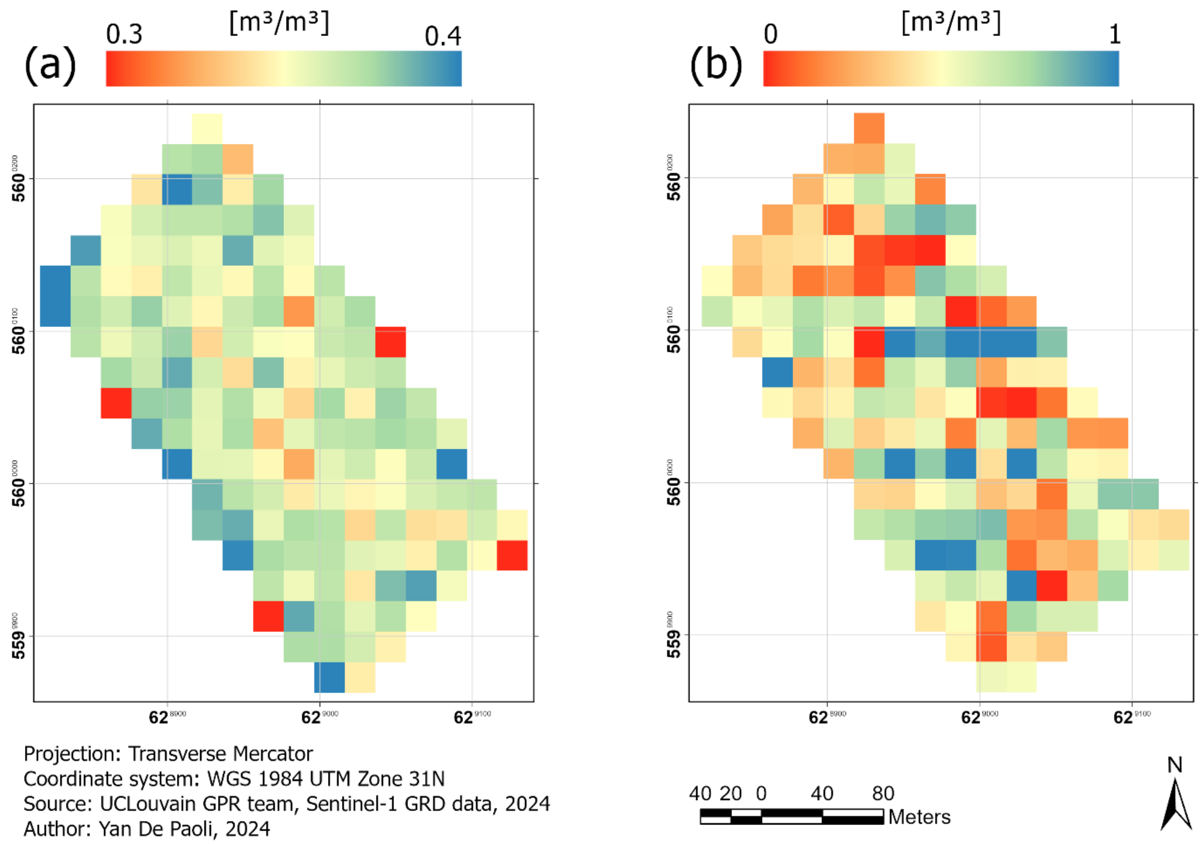

Figure 21: Comparison of soil moisture estimations between (a) GPR-based results and (b) SAR-based results, at 20-meter spatial resolution on August 25, 2023. Panel (a) shows volumetric soil moisture estimations obtained using GPR after aggregation to a spatial resolution of 20 meters. The color scale ranges from 0.3 to 0.4. Panel (b) shows volumetric soil moisture estimations obtained using SAR data at a spatial resolution of 20 meters. The color scale ranges from 0 (dry) to 1 (saturated).

Figure 21 (a) shows the GPR-based estimation of soil moisture across the field on August 25th, 2023. This map, with a spatial resolution of 20 meters, uses color coding to represent varying levels of volumetric soil moisture, ranging from 0.3 to 0.4. The map reveals a heterogeneous distribution of soil moisture, with higher moisture levels concentrated in the northwestern and middle western parts of the field, indicated by blue regions. In contrast, several patches near the southern edge of the field exhibit lower moisture levels, which corresponds with the elevation information from Figure 2 (a), showing a slope from south to north. The presence of both high and low moisture zones underscores the variability within the field.

In contrast, Figure 21 (b) presents the SAR-based soil moisture estimation for the same date, capturing moisture information from a shallower soil layer, specifically between 0 to 10 centimeters. This map, also with a 20-meter resolution, uses a color gradient to represent volumetric soil moisture levels, ranging from 0 (dry) to 1 (saturated). The image shows significant spatial variability, with high moisture areas, depicted in blue, primarily concentrated in the central parts of the field. Conversely, red areas indicate low moisture levels, representing dry surface conditions, predominantly in the southeastern and northwestern corners of the field. The map reveals distinct patterns in soil moisture distribution, with noticeable gradients transitioning from wetter to drier regions.

Comparing these two maps highlights the stratification of soil moisture at different depths. The second matching date is as follows:

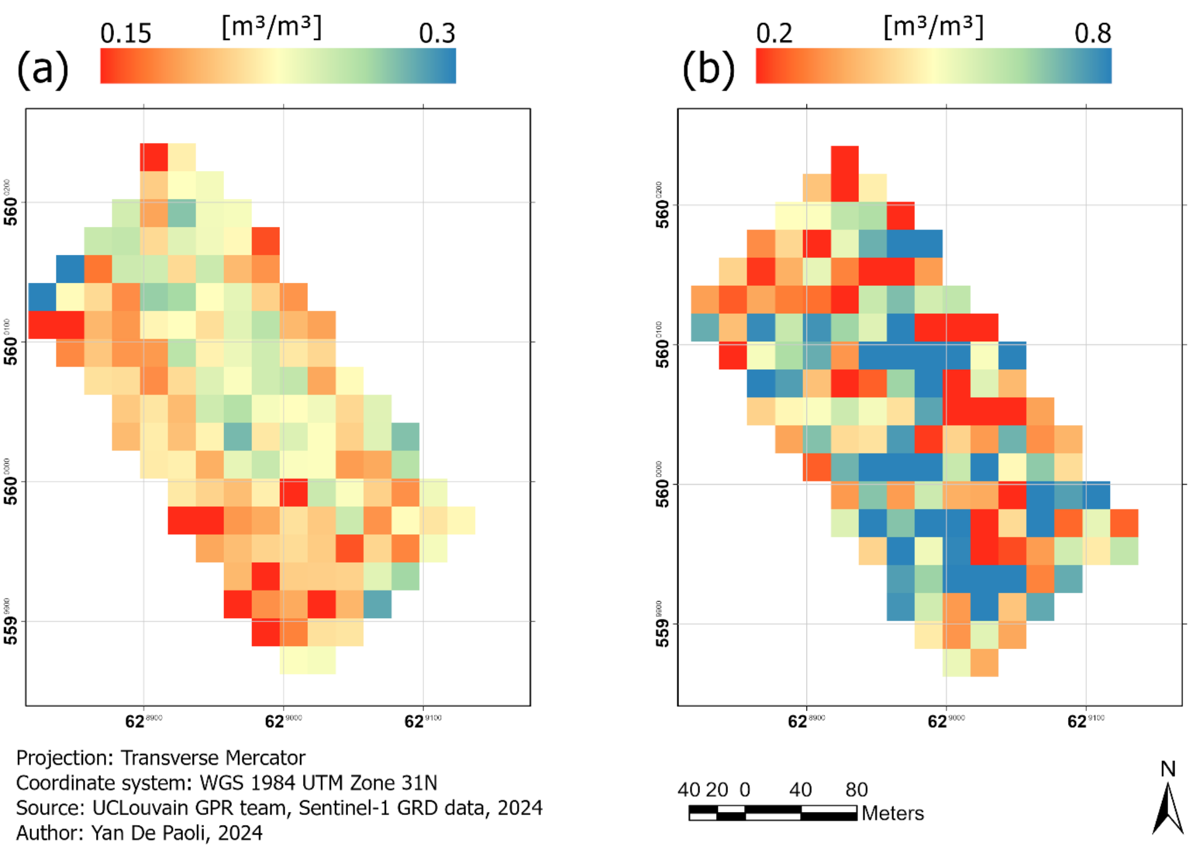

Figure 22: Comparison of soil moisture estimations between (a) GPR-based results and (b) SAR-based results, at 20-meter spatial resolution on September 11, 2023. Panel (a) shows volumetric soil moisture estimations obtained using

GPR after aggregation to a spatial resolution of 20 meters. The color scale ranges from 0.15 to 0.3. Panel (b) shows volumetric soil moisture estimations obtained using SAR data at a spatial resolution of 20 meters, with values from 0.2 to 0.8.

Figure 22 (a) shows the GPR-based soil moisture estimation on September 11th, 2023. Compared to the previous date, there is a noticeable decrease in overall moisture levels across several parts of the field, with values now ranging from 0.15 to 0.3. Despite this decrease, spatial variability remains prominent. For instance, the western part of the field appears to preserve less moisture compared to the eastern part. However, the northwest section shows a high concentration of moisture, which aligns with the elevation data from Figure 22 (a), indicating a talweg in that area

The same patterns are not as apparent in Figure 22 (b), which presents the SAR-based soil moisture estimation for the same date. In this map, high moisture areas (blue) are visible in the central and southern parts of the field, consistent with Figure 3's left panel, which indicates poor natural drainage in the center of the field. In contrast, the GPR-based map in Figure 22 (a) shows higher moisture concentrations in the northwestern part of the field, suggesting that deeper soil layers retain moisture differently. While Figure 22 (a) indicates low moisture in the southwestern part of the field, Figure 22 (b) shows drier regions predominantly in the northeastern part. Comparing the SAR-based estimations from September 11th, 2023, with those from August 25th, 2023, reveals that the central area of the field maintained high moisture concentrations, with persistent heterogeneity in the moisture distribution.

As detailed in Sub-Section 5.1.3, and due to satellite capabilities, only one TVDI result with a spatial resolution of 30 meters was produced to match the GPR-based estimations. Below is their comparison:

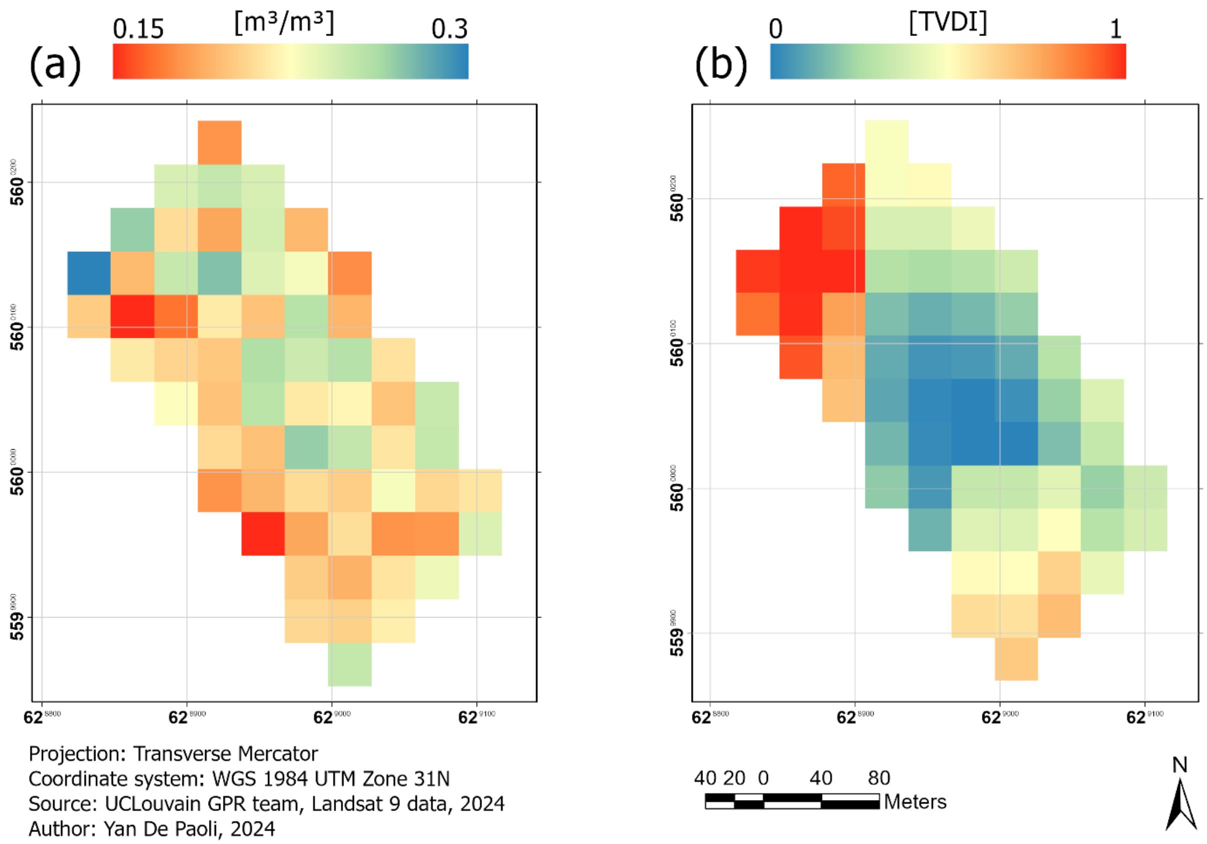

Figure 23: Comparison of soil moisture estimations assessment (a) GPR-based results and (b) TVDI results, at 30-meter spatial resolution on September 11, 2023. Panel (a) shows volumetric soil moisture estimations obtained using GPR after aggregation to a spatial resolution of 30 meters. The color scale ranges from 0.15 to 0.3. Panel (b) shows TVDI values obtained using optical/thermal data at a spatial resolution of 30 meters, with values from 0 to 1.

Figure 23 (a) illustrates the GPR-based soil moisture estimation across the AOI on September 11th, 2023, with a spatial resolution of 30 meters. This map depicts moisture levels in the top 40 cm of the soil, ranging from 0.15 to 0. The map shows a concentration of moisture in the center of the plot, similar to the 20-meter resolution map, but with less general variability due to the resampling applied. The transformation from the map constructed with kriging (1.3 meters) to 30 meters impacts the overall spatial distribution comparison, potentially masking small-scale variability and smoothing out some of the spatial patterns observed in the original high-resolution data.

Figure 23 (b) presents the TVDI estimation of soil moisture across the AOI on September 11th, 2023, also with a spatial resolution of 30 meters. The TVDI values range from 0 (wet conditions) to 1 (dry conditions). The map reveals distinct spatial variability, with higher TVDI values (red and orange) concentrated in the northwestern part of the field, suggesting drier conditions in this region. Conversely, lower TVDI values (blue and green) are observed in the central and southeastern parts, indicating wetter conditions, consistent with the poor natural drainage in the center of the field shown in Figure 3's left panel. This distribution pattern aligns with the moisture concentration observed in the GPR-based estimation for the same date. Figure 23 (a) shows some moisture concentration in the central part of the field and lower values in the northwest part, with the exception of the highest value, which is not captured by the TVDI result.

To be able to make a comparison between TVDI and SAR-based estimation having the same spatial resolution, the latter was resampled using a bilinear method.

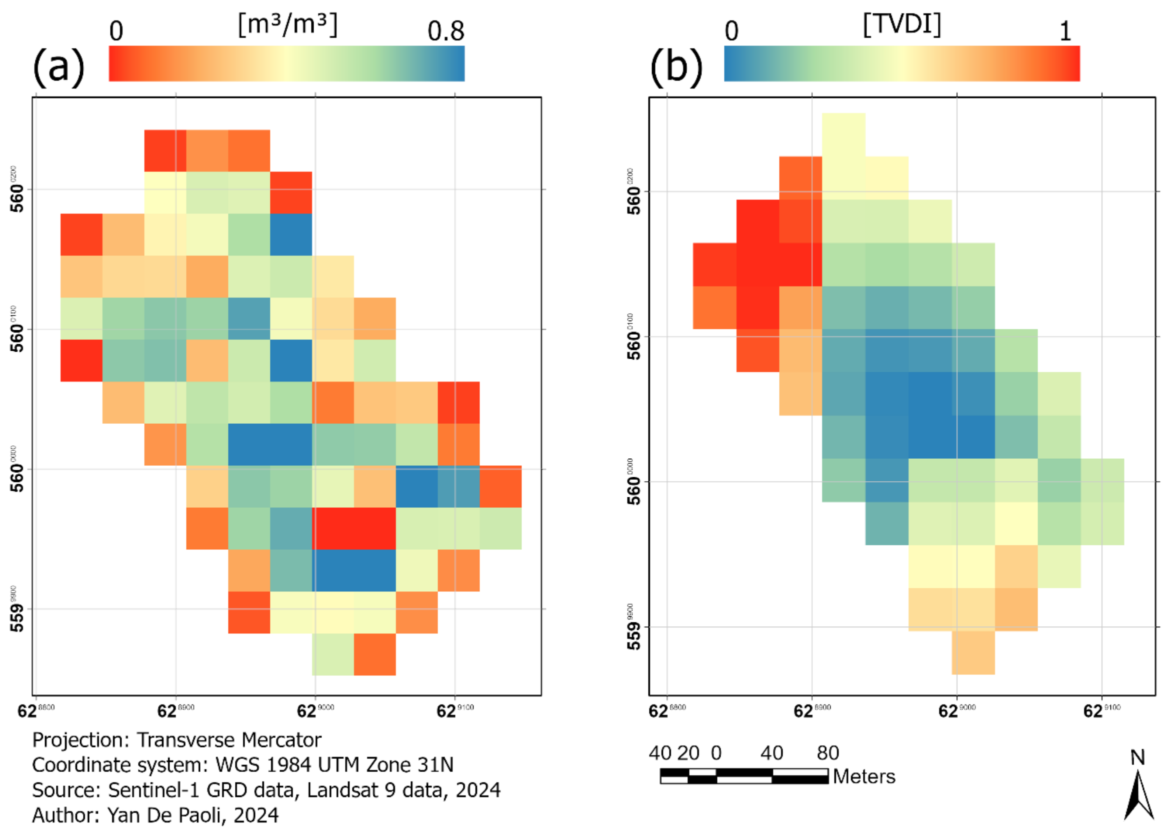

Figure 24: Comparison of soil moisture estimations assessment (a) SAR-based results and (b) TVDI results, at 30-meter spatial resolution on September 11, 2023. Panel (a) shows volumetric soil moisture estimations obtained using SAR data at a spatial resolution of 30 meters, with values ranging from 0 to 0.8. Panel (b) shows TVDI values obtained using optical/thermal data at a spatial resolution of 30 meters, with values from 0 to 1.

Figure 24 presents the results. Panel (a) displays the SAR-based estimation aggregated to a spatial resolution of 30 meters, representing volumetric soil moisture levels. The image shows significant spatial variability, indicating areas of both high and low soil moisture. Both Panel (a) and (b) show the central part of the field with a higher concentration of soil moisture, which is consistent with the poor natural drainage indicated in Figure 3's left panel, demonstrating good agreement between the soil moisture assessments. However, Panel (a) shows lower values at the borders, which might be due to error propagation from the resampling technique.

7 Discussion

This Section delves into the interpretation of the results obtained from Section 5, assessing the spatiotemporal variability observed in the field, aiming to discuss the strengths and limitations of each method. By comparing soil moisture data across different depths and timeframes, we aim to understand the dynamic nature of soil moisture distribution and its implications for agricultural practices. The discussion will also address the potential factors influencing soil moisture patterns, such as soil texture, topography, and land management. Furthermore, we explore the practical applications of these findings in optimizing irrigation strategies, enhancing crop yield, and ensuring sustainable water resource management. Through this comprehensive analysis, we aim to provide actionable insights and recommendations for improving soil moisture monitoring and management in agricultural fields. Finally, future perspectives are addressed, already drawing next steps to this research.

7.1 Key Findings

The present work examined changes in soil moisture across the field using three different estimation techniques: SAR-based method, optical/thermal-based method, and GPR soil moisture estimations. Due to their signal's nature, each technique provided insights with different characterization depth and resolution, highlighting the dynamic and heterogeneous nature of soil moisture within the AOI. The analysis demonstrated how these methods complement each other, with SAR and TVDI offering surface-level estimations, while GPR provided deeper soil moisture data.

Examining the temporal variability revealed a strong relationship between soil moisture assessment and precipitation events. Over a period of two years (2022 and 2023), the SAR and tTVDI methods showed expected positive and negative correlations with precipitation of, respectively, 75.86% and 92.86%. The combination of a precipitation peak on June 22nd, 2023, following a period of drought is particularly interesting as it can reveal hidden soil dynamics such as infiltration and retention of moisture. This aspect is further explored in the results interpretation to understand the underlying soil processes.

Regarding direct comparison, the SAR-based and GPR-based soil moisture data, for the short period of overlaying results, showed a good agreement through a spearman correlation coefficient of 0.78. Particularly for the days after rainfall it is possible to see both estimations showing high sensitivity to precipitation occurrences. For instance, following a precipitation event on August 25th, 2023, both methods captured an increase in soil moisture, though the GPR data revealed more variability. Meanwhile, the tTVDI method, despite being affected by cloud cover and data availability, mirrored these moisture trends, presenting opposite patterns with precipitation (e.g. decreasing when rainfall events), but incapable of being evaluated in the temporal dimension against GPR.

In exploring the spatial variability, the GPR estimations, with a characterization depth of about 40 cm, revealed significant differences in soil moisture across the field. Higher moisture levels were concentrated in the northwestern and middle western parts of the field, while lower levels were observed towards the southern edge. This variability was more pronounced in the high-resolution (20 meters) resampled maps, underscoring localized differences in water retention, aligning with the elevation map presented, which showed a slope from south to north in the AOI. However, the analysis of spatial variability added only a limited value to the overall work, given the different sensitivities with respect to depth of the different methods.

The SAR-based method effectively recreated the moisture condition for the top 10 cm layer of the soil. It was anticipated that the change detection approach might not show a strong spatial distribution similarity with the GPR estimation due to the different depths at which they operate. Further analysis is needed to understand how moisture transfers from the 10 cm layer to the 40 cm depth, specifically within the AOI. This process of moisture transfer and retention might hold the key to connecting SAR-based and GPR-based results. The presence of two soil types with different drainage capabilities can be affecting the distributions seen in both results with different characterization depths. The TVDI method, focusing on surface moisture (e.g. 0 to 5 cm), can be more directly related to the SAR-based method, as both assess similar soil layers. However, these two methods are affected by vegetation and roughness, while GPR was not, in this specific case, thanks to the relatively large wavelength used.

The impact of resolution on data interpretation became evident when transforming the original high-resolution GPR data (1.3 meters) to a coarser resolution (30 meters). In the Appendix is possible to see the original GPR-based maps obtained with kriging. The further resampling process led to a loss of finer details, smoothing out small-scale variability and potentially masking subtle spatial patterns. Additionally, due to cloud cover limitations, fewer days were available for TVDI data production, resulting in only one matching date between the three methods. This single matching date is insufficient for significant comparison due to the many uncertainties involved. Therefore, while the spatial variability analysis provided some insights, its contribution is constrained by different characterization between GPR and the two other models, as well as the limitations in TVDI data acquisition.

However, applying the TVDI method provided valuable insights into surface moisture conditions, distinguishing between drier and wetter areas. On September 11th, 2023, the TVDI map identified higher dryness in the northwestern part of the field and wetter conditions in the central and southeastern parts. This pattern aligned with the observations from GPR and SAR-based estimations, reinforcing TVDI's utility in detecting surface moisture variability. However, the coarser resolution of TVDI limited its capacity to capture finer spatial details compared to the high-resolution GPR data.

These findings collectively underscore the importance of integrating multiple remote sensing techniques to achieve a comprehensive understanding of soil moisture dynamics, while also highlighting the critical role of resolution in accurately capturing spatial variability.

7.2 In-depth Event Analysis

The temporal variability result showed 2 years of comparison between the SAR-based model and tTVDI, highlighting how their time-series were varying according to precipitation on the field. Figure 19 demonstrates that soil moisture levels fluctuate seasonally, with higher values in spring and autumn, correlating with increased precipitation and lower temperatures, and lower values in summer, correlating with higher temperatures and evapotranspiration rates.

Significant events, such as substantial rainfall or drought periods, cause sharp changes in soil moisture. For instance, on June 22, 2023, the AOI experienced a significant precipitation peak following a drought period. This event offers a unique opportunity to understand the impact of antecedent dry conditions on the soil's ability to absorb and retain moisture. The field received nearly 40 mm of rainfall, the highest recorded precipitation in the observed period. This event followed a dry spell from May 16 to June 17, 2023, characterized by an absence of rainfall. During this period, as shown in Figure 4, the area experienced several days of high temperatures and presented an increasing NDVI (see Figure 25) consequently having higher evapotranspiration rates, leading to significantly reduced soil moisture levels.

The extended drought resulted in the depletion of soil moisture in the surface layers. The SAR-based soil moisture estimations showed a steady decline, with volumetric soil moisture levels dropping to around 0.47 by mid-June. In contrast, the tTVDI results indicated a continuous increase until just before the event, with values above 0.8, suggesting that most of the field could be under stress.

On the major event day, the tTVDI result showed immediate sensitivity, decreasing to around 0.5. This value could also have been influenced by minor precipitation events on June 18 and 20. Interestingly, after the event on the 22nd, there were a few days without rain, and the SAR-based results rapidly decreased during this short interval.

A similar pattern was observed in the previous year between April and July when precipitation events were scarce, and the surface soil moisture began to decline as indicated by both models. During this specific period, the lack of tTVDI data points limits a deeper understanding when merging the models. However, it provides a general indication of dryness in the field.

As studied by Quintana et al. (2023) and Meza et al. (2020), drought events can significantly impact soil permeability by causing structural destabilization and changes between layers. Furthermore, while soil cracking is expected during dry periods, (Cordero et al., 2014) demonstrated that the damage can be intensified when the soil is re-wetted after a drying period. The sequence of events analyzed over these two years could lead to such soil damage.

The GPR acquisition, occurring only between August 22 and September 20, 2023, provided a shortened but insightful temporal analysis. Figure 20 shows that GPR-based soil moisture estimations present a larger range than the SAR-based model. One potential source for this difference is the origin of the measurements. As stated in Sub-Section 4.2.2, the very high-resolution data generated soil moisture maps with approximately 1.3 meters of spatial resolution, presenting finer details about spatial variability within the field. The Appendix Section shows all the GPR estimations in their original resolution. When aggregating the pixels, this variability is smoothed in the spatial dimension. However, the general trend remains evident in the time dimension, with the time-series presenting values from 0.22 to 0.36 (m^3/m^3). Despite having less variability presented in the time-series, the SAR-based estimations for the same 1-month period with GPR data show high sensitivity to precipitation and therefore a similar behavior to the GPR results curve. Taking GPR results as more accurate, it appears that the SAR-based results could present a forward time delay, raising the question of how this might occur.

An important factor to consider is the measurement depth, as there is a discrepancy between the sensor's penetration capabilities and what influences soil moisture dynamics at different depths. Although different studies (Legates et al., 2010; Tromp-van Meerveld and McDonnell, 2006) indicate a strong continuity between soil moisture concentrations across layers, many factors can impact moisture dynamics. Horton et al. (1994) pointed out that compactive processes, often related to agricultural practices, affect soil hydraulic properties, consequently influencing water retention and transport in response to changes in pore space geometry. Additionally, as Liu et al. (2019a) stated, water content concentration and plant root systems can significantly affect soil infiltration capacity, with soil moisture being the main factor influencing initial infiltration rates and below-ground biomass determining steady-state infiltration rates. Therefore, multiple reasons could explain the apparent delay between estimations, and a specific study on the interaction of soil moisture between layers in the AOI should be conducted.

In contrast to the GPR results, the SAR-based spatial distribution exhibits a randomness on both matching dates, which could be attributed to the sensitivity present in the C band to vegetation, roughness and speckle noise, which leads to poor characterization at the scale of the field analyzed in this study. These spatial discrepancies between results could be related to the models' constraints and assumptions, which will be discussed in the next Sub-Section.

7.3 Comparison with previous studies

The results of this study are compared with previous research that performed similar analyses to assess soil moisture status. Using a change detection method, Zribi et al. (2008) also observed a high agreement between their estimations and precipitation events, despite using NDVI for vegetation characterization and radar data from the ERS Scatterometer. In the present study, 75.86% of the high estimations align with precipitation events from the previous two days, which is consistent with the 92% agreement found by Zribi et al. This similarity is notable because the same metric was applied in both studies, enabling a direct comparison. However, a significant difference lies in the spatial resolution: the present study used 20m resolution, whereas Zribi et al. used 25 km. This disparity affects the comparison, as Zribi et al. analyzed a much larger area with different LULC characteristics.

Gao et al. (2017) and Bhogapurapu et al. (2021b) also used Sentinel-1 SAR data to estimate volumetric soil moisture with a 100m spatial resolution. While their studies showed good alignment with precipitation events, they did not focus on qualitative time-series comparisons as done in the present work. Instead, they compared their estimations directly with in-situ measurements over extended periods, resulting in low RMSE values—0.087 m^3/m^3 for Gao et al. and approximately 0.050 for Bhogapurapu et al. A key difference in the present study is the use of GPR-based estimations, which allow for comparisons of spatial distributions at much higher resolutions. Despite differences in characterization depth, GPR-based estimations demonstrated the potential to serve as proxies for finer soil moisture satellite estimations, both temporally and spatially.

Studies that used the TVDI to correlate surface moisture status often faced challenges related to cloud cover and coarse spatial resolution. For example, Rawat et al. (2022) found a high negative correlation (R^2 = -0.8) between in-situ soil moisture measurements and TVDI, albeit with a spatial resolution of 250m. While this supports the general approach capability, it is not suitable for small-scale farming. In contrast, the present study, using GPR-based estimations as a proxy, was able to evaluate small-scale trends in the field for the available matching dates, showing potential insights applicable for agriculture.

Finally, when comparing the tTVDI results from Przeździecki et al. (2023), which focused on forested areas and showed good agreement with evapotranspiration models, to our study, we found that our tTVDI time series also aligned well with SAR-based estimations and precipitation events in agricultural areas. This indicates that, once the issue of heterogeneity within a given area is resolved, the tTVDI approach can effectively capture general soil moisture trends in an agricultural environment, even a small scale field.

7.4 Practical implications

Translating the findings from soil moisture estimations and remote sensing data into real-life, on-farm concrete results presents several challenges. One major difficulty lies in the inherent variability and complexity of field conditions, which can differ significantly from the controlled environments in which models are often tested and validated (Visser et al., 2021). The AOI has been utilized for diverse crop rotations over recent years, reflecting a farm management approach to maintaining soil health and optimizing agricultural productivity. This variability in crop types and farming practices adds layers of complexity when it comes to directly using remote sensing data to inform on-the-ground decisions.

In 2023, spinach was cultivated in the field with two distinct sowing and harvesting periods. The first sowing took place on May 6, 2023, followed by harvesting on June 23, 2023. A second sowing occurred on August 14, 2023, with harvesting on September 23, 2023. This practice of sequential planting allows for maximizing the use of the field throughout the growing season, ensuring efficient land use and crop production. Figure 25 in the Appendix Section shows NDVI values aligning with these agricultural activities, presenting an increase starting in May 2023 and peaking in June 2023, which corresponds to the first spinach growing period. Similarly, after a dip in July 2023, the NDVI values rise again in August and September 2023, peaking before the second harvest.

The specific timing of these agricultural activities can greatly influence soil moisture dynamics, as observed in the study. In Figure 26, the SAR-based soil moisture levels show a steady decline starting in early May, just before the first sowing date, indicating pre-existing dry conditions. During the first sowing period, soil moisture fluctuates around lower values, reflecting minor precipitation events and irrigation. Leading up to the first harvest in late June, there is a noticeable increase in soil moisture levels around mid-June, corresponding to the significant rainfall event on June 22, 2023. Post-harvest, soil moisture levels drop sharply. Prior to the second sowing date in mid-August, soil moisture levels are relatively stable but on a declining trend. Following the second sowing, there is a slight increase in soil moisture, which could be due to irrigation or minor rainfall events. Leading up to the second harvest in late September, soil moisture levels show another peak in early September, followed by a decline towards the end of the month.

Figure 27 shows that the tTVDI values around early May are relatively high, indicating dry conditions. During the first sowing period, tTVDI values peak in early June, reflecting increasing dryness. Just before the first harvest in late June, tTVDI values decrease sharply, coinciding with the significant rainfall event on June 22, 2023, reducing soil dryness. Around the second sowing date in mid-August, tTVDI values drop to around 0.5, indicating some moisture in the field. During the second growing period, tTVDI values increase, reflecting growing dryness.

Relating the remote sensing results with ground-based in-situ measurements is essential for accurate irrigation and crop management. In-situ measurements can provide ground information to calibrate remote sensing models, ensuring their reliability and accuracy. However, given the inherent field variability, these sensors have limited value for validation, as they are not representative of the moisture at a larger scale.

The impact on irrigation management is substantial. The study’s results highlight the importance of understanding temporal and spatial variability in soil moisture for efficient water use. For the 2023 spinach crops, this means adjusting irrigation schedules based on the observed moisture levels and anticipated weather conditions. For instance, the period following the significant rainfall event on June 22 could benefit from reduced irrigation needs, while dry spells, such as the one from May 16 to June 17, would necessitate increased irrigation to maintain optimal soil moisture levels. This targeted approach can prevent over-irrigation, conserve water, and ensure that crops receive the right amount of moisture when they need it the most.

In terms of crop management strategies, the insights gained from the study can inform decisions on crop rotation, planting, and harvesting schedules. Understanding soil moisture dynamics helps in selecting the right crops for specific seasons, planning sowing and harvesting dates to align with favorable moisture conditions, and implementing soil health practices that enhance moisture retention (Kukal et al., 2019). For instance, the observed sensitivity of tTVDI to low temperatures and bare soil conditions during winter suggests that cover crops or mulch might be beneficial to maintain soil moisture and prevent erosion.

7.5 Limitations

The limitations of this study are primarily related to data constraints, methodological challenges, and generalizability issues. Optical and thermal data constraints, particularly cloud cover, pose significant challenges. For instance, Landsat 9 imaging is often hampered by cloud cover, which is an important issue in regions like Belgium, where cloudiness prevails most of the year. This limitation reduces the robustness of temporal comparisons, as having more frequent data points would provide a more comprehensive understanding of moisture dynamics. Additionally, the spatial resolution of 20 to 30 meters may not be fine enough to capture small-scale variations in soil moisture for fields as small as 6 hectares. As shown in the results, this spatial resolution can capture general trends on the AOI, but it would require a much larger area to identify clearer patterns. Moreover, the limited number of matching dates between datasets, such as the single TVDI result at a 30-meter resolution, further restricts detailed temporal analysis.

Methodologically, each soil moisture estimation technique has its constraints. The GPR measures soil moisture of the top 40 cm. Conversely, the SAR-based estimations provide surface soil moisture (0-10 cm), which can be highly variable and influenced by recent precipitation or irrigation. This surface-level focus might not reflect deeper soil moisture conditions, crucial for long-term water management. Additionally, TVDI, beyond capturing the surface moisture levels, relies heavily on the vegetation-evapotranspiration relationship. As observed in the 2022-2023 winter, the index's sensitivity can be impacted by seasonal variations, proving that its usage must be always contextualized.

Technical challenges also played a significant role in this study. Integrating data from different sensors and methods posed difficulties due to variations in resolution, temporal availability, and measurement principles (as it is possible to see in Sub-Section 5.1.3). Ensuring that these datasets are comparable required meticulous preprocessing and alignment, which is not always straightforward. Environmental factors such as vegetation cover, natural soil drainage, and land management practices can interfere with remote sensing measurements, leading to potential inaccuracies. For instance, dense vegetation can obscure SAR signals, making precise soil moisture readings challenging. Moreover, the short duration of GPR data collection, with only eight measurements taken within less than a month, represents a significant constraint to perform a proper validation exercise.

The scalability of the findings is another limitation. The results are specific to the study area and its unique environmental conditions, which may limit the applicability to other regions with different soil types, climatic conditions, and agricultural practices. Therefore, while the results provide valuable insights for the specific study area, they might not be directly applicable to different contexts without further validation.

7.6 Future research directions

To advance the understanding and application of soil moisture estimation methods, several future research directions are proposed. Validating these assumptions will require a comprehensive approach involving enhanced monitoring techniques, field experiments, and longitudinal studies. Enhanced monitoring techniques, such as integrating data from multiple remote sensing platforms with different spectral bands and penetration depths, can provide a more comprehensive view of soil moisture dynamics. Field experiments and in-situ measurements are essential to verify the accuracy of SAR, and TVDI estimations, particularly during significant events like substantial rainfall or drought periods.

Longitudinal studies are essential for understanding the temporal dynamics of soil moisture. Continuous monitoring over extended periods, using GPR or other technology on the field, will help identify long-term trends and seasonal variations in soil moisture levels, revealing how soil moisture responds to changing climatic conditions, irrigation practices, and land management strategies. The integration of soil properties on the moisture estimation is another important research direction, as it can bring absolute values that can be compared with more conventional ways of measuring soil moisture, which are closer to farmers' reality.

Future studies should aim to quantify the other influences mentioned in the present work (e.g. topography and pedology related factors) and incorporate them into soil moisture models to enhance the accuracy of moisture estimations and provide more reliable data aiming to understand water resources management and crop yields optimization, as stated by Holzman et al. (2014) and Bhogapuruapu et al. (2022). The use of soil hydrodynamic models and data assimilation techniques can be the bridge to connect these results to what is experienced in the field.

Given the higher number of matching dates for SAR and TVDI data over the two-year study period, there is significant potential for a strong comparative analysis between these two methods. Such a comparison can elucidate the strengths and weaknesses of each method in different conditions and depths. Ideally, the usage of C-band (and L-band) drone-borne GPR measurements would facilitate the validation, bringing more reliability to the analysis. On top of that, the integration of different radar satellites with various bands and depth penetration capabilities can provide a multi-layered understanding of soil moisture. Combining data from multiple satellites can improve the temporal resolution of soil moisture monitoring, allowing for more frequent updates and better responsiveness to changing conditions. These efforts will collectively improve the accuracy and applicability of soil moisture estimations, supporting more effective water resource management and agricultural practices.

8 Conclusion

This study evaluated the effectiveness of SAR and Optical/Thermal-based methodologies for soil moisture estimation in the Grand Villers field, Belgium, by integrating these approaches with GPR data to analyze spatiotemporal trends. The findings showed that SAR and TVDI methods effectively captured surface moisture, while GPR provided valuable insights into root-zone moisture, highlighting the complementary nature of these techniques. The research demonstrated a positive correlation between SAR-based soil moisture and precipitation, as well as a strong negative correlation between TVDI and rainfall events, though factors like cloud cover and resolution constraints affected data robustness. Additionally, SAR-based and GPR-based estimations showed a Spearman correlation of 0.78 for the overlapping period. Notably, TVDI indicated a characteristic moisture concentration in the center of the field, possibly related to varying soil drainage capacities within the AOI. Despite the challenges, the integration of these methodologies offered a comprehensive understanding of soil moisture dynamics, crucial for efficient irrigation and crop management.

The study's limitations, including data constraints and methodological challenges, underscore the need for careful contextualization and further research. Issues such as cloud cover, resolution limits, and the brief GPR data collection period highlighted the difficulties in accurately capturing small-scale moisture variations and validating results. Moreover, the unique environmental conditions of the study area may limit the generalizability of the findings, necessitating further validation in different contexts.

Future research should focus on enhancing monitoring techniques, conducting longitudinal studies, and integrating multiple remote sensing platforms to improve soil moisture estimation accuracy. Incorporating soil properties and understanding how influences like topography and pedology could be translated and assimilated into the soil moisture models would bridge the gap between remote sensing data and practical applications, ultimately supporting better water resource management and agricultural practices.

References

Al-Yaari, A., Wigneron, J.P., Ducharne, A., Kerr, Y., de Rosnay, P., de Jeu, R., Govind, A., Al Bitar, A., Albergel, C., Muñoz-Sabater, J., Richaume, P., Mialon, A., 2014. Global-scale evaluation of two satellite-based passive microwave soil moisture datasets (SMOS and AMSR-E) with respect to Land Data Assimilation System estimates. Remote Sens. Environ. 149, 181–195. https://doi.org/10.1016/J.RSE.2014.04.006

Ali, I., Greifeneder, F., Stamenkovic, J., Neumann, M., Notarnicola, C., 2015. Review of Machine Learning Approaches for Biomass and Soil Moisture Retrievals from Remote Sensing Data. Remote Sens. 2015, Vol. 7, Pages 16398-16421 7, 16398–16421. https://doi.org/10.3390/RS71215841

Amazirh, A., Merlin, O., Er-Raki, S., Gao, Q., Rivalland, V., Malbeteau, Y., Khabba, S., Escorihuela, M.J., 2018. Retrieving surface soil moisture at high spatio-temporal resolution from a synergy between Sentinel-1 radar and Landsat thermal data: A study case over bare soil. Remote Sens. Environ. 211, 321–337. https://doi.org/10.1016/J.RSE.2018.04.013

Ambrosone, M., Matese, A., Di Gennaro, S.F., Gioli, B., Tudoroiu, M., Genesio, L., Miglietta, F., Baronti, S., Maienza, A., Ungaro, F., Toscano, P., 2020. Retrieving soil moisture in rainfed and irrigated fields using Sentinel-2 observations and a modified OPTRAM approach. Int. J. Appl. Earth Obs. Geoinf. 89, 102113. https://doi.org/10.1016/J.JAG.2020.102113

Attarzadeh, R., Amini, J., Notarnicola, C., Greifeneder, F., 2018. Synergetic Use of Sentinel-1 and Sentinel-2 Data for Soil Moisture Mapping at Plot Scale. Remote Sens. 2018, Vol. 10, Page 1285 10, 1285. https://doi.org/10.3390/RS10081285

Babaeian, E., Sadeghi, M., Jones, S.B., Montzka, C., Vereecken, H., Tuller, M., 2019. Ground, Proximal, and Satellite Remote Sensing of Soil Moisture. Rev. Geophys. 57, 530–616. https://doi.org/10.1029/2018RG000618

Balenzano, A., Mattia, F., Satalino, G., Davidson, M.W.J., 2010. Dense Temporal Series of C- and L-band SAR Data for Soil Moisture Retrieval Over Agricultural Crops. IEEE J. Sel. Top. Appl. Earth Obs. Remote Sens. 4, 439–450. https://doi.org/10.1109/JSTARS.2010.2052916

Bao, Y., Lin, L., Wu, S., Kwal Deng, K.A., Petropoulos, G.P., 2018. Surface soil moisture retrievals over partially vegetated areas from the synergy of Sentinel-1 and Landsat 8 data using a modified water-cloud model. Int. J. Appl. Earth Obs. Geoinf. 72, 76–85. https://doi.org/10.1016/J.JAG.2018.05.026

Bauer-Marschallinger, B., Freeman, V., Cao, S., Paulik, C., Schaufler, S., Stachl, T., Modanesi, S., Massari, C., Ciabatta, L., Brocca, L., Wagner, W., 2018. Toward Global Soil Moisture Monitoring with Sentinel-1: Harnessing Assets and Overcoming Obstacles. IEEE Trans. Geosci. Remote Sens. 57, 520–539. https://doi.org/10.1109/TGRS.2018.2858004

Beckers, A., Dewals, B., Erpicum, S., Dujardin, S., Detrembleur, S., Teller, J., Pirotton, M., Archambeau, P., 2013. Contribution of land use changes to future flood damage along the river Meuse in the Walloon region. Nat. Hazards Earth Syst. Sci. 13, 2301–2318. https://doi.org/10.5194/NHESS-13-2301-2013

Berg, A., Sheffield, J., 2018. Climate Change and Drought: the Soil Moisture Perspective. Curr. Clim. Chang. Reports 4, 180–191. https://doi.org/10.1007/S40641-018-0095-0/METRICS

Bhogapurapu, N., Dey, S., Bhattacharya, A., Mandal, D., Lopez-Sanchez, J.M., McNairn, H., López-Martínez, C., Rao, Y.S., 2021a. Dual-polarimetric descriptors from Sentinel-1 GRD SAR data for crop growth assessment. ISPRS J. Photogramm. Remote Sens. 178, 20–35. https://doi.org/10.1016/J.ISPRSJPRS.2021.05.013

Bhogapurapu, N., Dey, S., Homayouni, S., Bhattacharya, A., Rao, Y.S., 2021b. Field-scale soil moisture estimation using sentinel-1 GRD SAR data. Adv. Sp. Res. 70, 3845–3858. https://doi.org/10.1016/J.ASR.2022.03.019

Bhogapurapu, N., Dey, S., Mandal, D., Bhattacharya, A., Karthikeyan, L., McNairn, H., Rao, Y.S., 2022. Soil moisture retrieval over croplands using dual-pol L-band GRD SAR data. Remote Sens. Environ. 271, 112900. https://doi.org/10.1016/J.RSE.2022.112900

Bian, Z., Roujean, J.L., Fan, T., Dong, Y., Hu, T., Cao, B., Li, H., Du, Y., Xiao, Q., Liu, Q., 2023. An angular normalization method for temperature vegetation dryness index (TVDI) in monitoring agricultural drought. Remote Sens. Environ. 284, 113330. https://doi.org/10.1016/J.RSE.2022.113330

Brogna, D., Dufrêne, M., Michez, A., Latli, A., Jacobs, S., Vincke, C., Dendoncker, N., 2018. Forest cover correlates with good biological water quality. Insights from a regional study (Wallonia, Belgium). J. Environ. Manage. 211, 9–21. https://doi.org/10.1016/J.JENVMAN.2018.01.017

Carlson, T.N., Gillies, R.R., Perry, E.M., 1994. A method to make use of thermal infrared temperature and NDVI measurements to infer surface soil water content and fractional vegetation cover. Remote Sens. Rev. 9, 161–173. https://doi.org/10.1080/02757259409532220

Carlson, T.N., Gillies, R.R., Schmugge, T.J., 1995. An interpretation of methodologies for indirect measurement of soil water content. Agric. For. Meteorol. 77, 191–205. https://doi.org/10.1016/0168-1923(95)02261-U

Černý, R., 2009. Time-domain reflectometry method and its application for measuring moisture content in porous materials: A review. Measurement 42, 329–336. https://doi.org/10.1016/J.MEASUREMENT.2008.08.011

Chaudhary, S.K., Srivastava, P.K., Gupta, D.K., Kumar, P., Prasad, R., Pandey, D.K., Das, A.K., Gupta, M., 2022. Machine learning algorithms for soil moisture estimation using Sentinel-1: Model development and implementation. Adv. Sp. Res. 69, 1799–1812. https://doi.org/10.1016/J.ASR.2021.08.022

Chen, S.W., Li, Y.Z., Wang, X.S., Xiao, S.P., Sato, M., 2014. Modeling and interpretation of scattering mechanisms in polarimetric synthetic aperture radar: Advances and perspectives. IEEE Signal Process. Mag. 31, 79–89. https://doi.org/10.1109/MSP.2014.2312099

Cloude, S., 2010. Polarisation: Applications in Remote Sensing, Polarisation: Applications in Remote Sensing. https://doi.org/10.1093/acprof:oso/9780199569731.001.0001

Cordero, J., Cuadrado, A., Ledesma, A., Prat, P.., 2014. Patterns of cracking in soils due to drying and wetting cycles, in: Khalili, N., Russel, A., Khoshghalb, A. (Eds.), Unsaturated Soils: Research & Applications. CRC Press, pp. 1–8.

Das, K., Paul, P.K., 2015. Present status of soil moisture estimation by microwave remote sensing. Cogent Geosci. 1, 1084669. https://doi.org/10.1080/23312041.2015.1084669

Datta, S., Das, P., Dutta, D., Giri, R.K., 2021. Estimation of Surface Moisture Content using Sentinel-1 C-band SAR Data Through Machine Learning Models. J. Indian Soc. Remote Sens. 49, 887–896. https://doi.org/10.1007/S12524-020-01261-X/METRICS

de Tomás, A., Nieto, H., Guzinski, R., Salas, J., Sandholt, I., Berliner, P., 2014. Validation and scale dependencies of the triangle method for the evaporative fraction estimation over heterogeneous areas. Remote Sens. Environ. 152, 493–511. https://doi.org/10.1016/J.RSE.2014.06.028

Della Vecchia, A., Ferrazzoli, P., Guerriero, L., Ninivaggi, L., Strozzi, T., Wegmüller, U., 2008. Observing and modeling multifrequency scattering of maize during the whole growth cycle. IEEE Trans. Geosci. Remote Sens. 46, 3709–3718. https://doi.org/10.1109/TGRS.2008.2001885

Entekhabi, D., Njoku, E.G., O'Neill, P.E., Kellogg, K.H., Crow, W.T., Edelstein, W.N., Entin, J.K., Goodman, S.D., Jackson, T.J., Johnson, J., Kimball, J., Piepmeier, J.R., Koster, R.D., Martin, N., McDonald, K.C., Moghaddam, M., Moran, S., Reichle, R., Shi, J.C., Spencer, M.W., Thurman, S.W., Tsang, L., Van Zyl, J., 2010. The soil moisture active passive (SMAP) mission. Proc. IEEE 98, 704–716. https://doi.org/10.1109/JPROC.2010.2043918

État de l'environnement Wallon, 2018. Principaux types de sols, État de l'environnement wallon.

Ferguson, J.E., Gunn, G.E., 2022. Polarimetric decomposition of microwave-band freshwater ice SAR data: Review, analysis, and future directions. Remote Sens. Environ. 280, 113176. https://doi.org/10.1016/J.RSE.2022.113176

Filipponi, F., 2019. Sentinel-1 GRD Preprocessing Workflow. Proc. 2019, Vol. 18, Page 11 18, 11. https://doi.org/10.3390/ECRS-3-06201

Franz, T.E., Wang, T., Avery, W., Finkenbiner, C., Brocca, L., 2015. Combined analysis of soil moisture measurements from roving and fixed cosmic ray neutron probes for multiscale real-time monitoring. Geophys. Res. Lett. 42, 3389–3396. https://doi.org/10.1002/2015GL063963

Gao, Q., Zribi, M., Escorihuela, M.J., Baghdadi, N., 2017. Synergetic Use of Sentinel-1 and Sentinel-2 Data for Soil Moisture Mapping at 100 m Resolution. Sensors 2017, Vol. 17, Page 1966 17, 1966. https://doi.org/10.3390/S17091966

Gardner, C.M.K., Dean, T.J., Cooper, J.D., 1998. Soil Water Content Measurement with a High-Frequency Capacitance Sensor. J. Agric. Eng. Res. 71, 395–403. https://doi.org/10.1006/JAER.1998.0338

Hajnsek, I., Jagdhuber, T., Schön, H., Papathanassiou, K.P., 2009. Potential of estimating soil moisture under vegetation cover by means of PolSAR. IEEE Trans. Geosci. Remote Sens. 47, 442–454. https://doi.org/10.1109/TGRS.2008.2009642

Han, L., Wang, P., Yang, H., Liu, S., Wang, J., 2006. Study on NDVI-Ts space by combining LAI and evapotranspiration. Sci. China, Ser. D Earth Sci. 49, 747–754. https://doi.org/10.1007/S11430-006-0747-0/METRICS

Holzman, M.E., Rivas, R., Piccolo, M.C., 2014. Estimating soil moisture and the relationship with crop yield using surface temperature and vegetation index. Int. J. Appl. Earth Obs. Geoinf. 28, 181–192. https://doi.org/10.1016/J.JAG.2013.12.006

Homayouni, S., McNairn, H., Hosseini, M., Jiao, X., Powers, J., 2019. Quad and compact multitemporal C-band PolSAR observations for crop characterization and monitoring. Int. J. Appl. Earth Obs. Geoinf. 74, 78–87.

https://doi.org/10.1016/J.JAG.2018.09.009

Hornáček, M., Wagner, W., Sabel, D., Truong, H.L., Snoeij, P., Hahmann, T., Diedrich, E., Doubková, M., 2012. Potential for high resolution systematic global surface soil moisture retrieval via change detection using sentinel-1. IEEE J. Sel. Top. Appl. Earth Obs. Remote Sens. 5, 1303–1311. https://doi.org/10.1109/JSTARS.2012.2190136

Horton, R., Ankeny, M.D., Allmaras, R.R., 1994. Effects of Compaction on Soil Hydraulic Properties. Dev. Agric. Eng. 11, 141–165. https://doi.org/10.1016/B978-0-444-88286-8.50015-5

Huisman, J.A., Hubbard, S.S., Redman, J.D., Annan, A.P., 2003. Measuring Soil Water Content with Ground Penetrating Radar: A Review. Vadose Zo. J. 2, 476–491. https://doi.org/10.2136/VZJ2003.4760

Jagdhuber, T., Hajnsek, I., Bronstert, A., Papathanassiou, K.P., 2012. Soil moisture estimation under low vegetation cover using a multi-angular polarimetric decomposition. IEEE Trans. Geosci. Remote Sens. 51, 2201–2215. https://doi.org/10.1109/TGRS.2012.2209433

Jeu, R.A.M. De, Holmes, T.R.H., Owe, M., 2005. Determination of the effect of dew on passive microwave observations from space. https://doi.org/10.1117/12.627919 5976, 51–59. https://doi.org/10.1117/12.627919

Karthikeyan, L., Chawla, I., Mishra, A.K., 2020. A review of remote sensing applications in agriculture for food security: Crop growth and yield, irrigation, and crop losses. J. Hydrol. 586, 124905. https://doi.org/10.1016/J.JHYDROL.2020.124905

Karthikeyan, L., Pan, M., Wanders, N., Kumar, D.N., Wood, E.F., 2017. Four decades of microwave satellite soil moisture observations: Part 1. A review of retrieval algorithms. Adv. Water Resour. 109, 106–120. https://doi.org/10.1016/J.ADVWATRES.2017.09.006

Kirkland, E.J., 2010. Bilinear Interpolation. Adv. Comput. Electron Microsc. 261–263. https://doi.org/10.1007/978-1-4419-6533-2_12

Klotzsche, A., Jonard, F., Looms, M.C., Kruk, J. van der, Huisman, J.A., 2018. Measuring Soil Water Content with Ground Penetrating Radar: A Decade of Progress. Vadose Zo. J. 17, 1–9. https://doi.org/10.2136/VZJ2018.03.0052

Koley, S., Jeganathan, C., 2020. Estimation and evaluation of high spatial resolution surface soil moisture using multi-sensor multi-resolution approach. Geoderma 378, 114618. https://doi.org/10.1016/J.GEODERMA.2020.114618

Kwak, S.K., Kim, J.H., 2017. Statistical data preparation: management of missing values and outliers. Korean J. Anesthesiol. 70, 407–411. https://doi.org/10.4097/KJAE.2017.70.4.407

Lambot, S., Andre, F., 2014. Full-wave modeling of near-field radar data for planar layered media reconstruction.

IEEE Trans. Geosci. Remote Sens. 52, 2295–2303. https://doi.org/10.1109/TGRS.2013.2259243

Lambot, S., Slob, E.C., Van Bosch, I. Den, Stockbroeckx, B., Vanclooster, M., 2004. Modeling of ground-penetrating radar for accurate characterization of subsurface electric properties. IEEE Trans. Geosci. Remote Sens. 42, 2555–2568. https://doi.org/10.1109/TGRS.2004.834800

Lambot, S., Weihermüller, L., Huisman, J.A., Vereecken, H., Vanclooster, M., Slob, E.C., 2006. Analysis of air-launched ground-penetrating radar techniques to measure the soil surface water content. Water Resour. Res. 42, 1–12. https://doi.org/10.1029/2006WR005097

Legates, D.R., Mahmood, R., Levia, D.F., DeLiberty, T.L., Quiring, S.M., Houser, C., Nelson, F.E., 2010. Soil moisture: A central and unifying theme in physical geography. http://dx.doi.org/10.1177/0309133310386514 35, 65–86. https://doi.org/10.1177/0309133310386514

Li, C., Adu, B., Wu, J., Qin, G., Li, H., Han, Y., 2022. Spatial and temporal variations of drought in Sichuan Province from 2001 to 2020 based on modified temperature vegetation dryness index (TVDI). Ecol. Indic. 139, 108883. https://doi.org/10.1016/J.ECOLIND.2022.108883

Linde, N., Vrugt, J.A., 2013. Distributed Soil Moisture from Crosshole Ground-Penetrating Radar Travel Times using Stochastic Inversion. Vadose Zo. J. 12, 1–16. https://doi.org/10.2136/VZJ2012.0101/111685

Liu, X., Chen, J., Cui, X., Liu, Q., Cao, X., Chen, X., 2019a. Measurement of soil water content using ground-penetrating radar: a review of current methods. Int. J. Digit. Earth 12, 95–118. https://doi.org/10.1080/17538947.2017.1412520

Liu, X., Cui, X., Guo, L., Chen, J., Li, W., Yang, D., Cao, X., Chen, X., Liu, Q., Lin, H., 2019b. Non-invasive estimation of root zone soil moisture from coarse root reflections in ground-penetrating radar images. Plant Soil 436, 623–639. https://doi.org/10.1007/S11104-018-03919-5/METRICS

Liu, Y., Yue, H., 2018. The Temperature Vegetation Dryness Index (TVDI) Based on Bi-Parabolic NDVI-Ts Space and Gradient-Based Structural Similarity (GSSIM) for Long-Term Drought Assessment Across Shaanxi Province, China (2000–2016). Remote Sens. 2018, Vol. 10, Page 959 10, 959. https://doi.org/10.3390/RS10060959

Lunt, I.A., Hubbard, S.S., Rubin, Y., 2005. Soil moisture content estimation using ground-penetrating radar reflection data. J. Hydrol. 307, 254–269. https://doi.org/10.1016/j.jhydrol.2004.10.014

Luo, D., Wen, X., He, P., 2023. Surface Soil Moisture Estimation Using a Neural Network Model in Bare Land and Vegetated Areas. J. Spectrosc. 2023, 5887177. https://doi.org/10.1155/2023/5887177

Ma, C., Li, X., McCabe, M.F., 2020. Retrieval of High-Resolution Soil Moisture through Combination of Sentinel-1 and Sentinel-2 Data. Remote Sens. 2020, Vol. 12, Page 2303 12, 2303. https://doi.org/10.3390/RS12142303

Mantas, C.J., Castellano, J.G., Moral-García, S., Abellán, J., 2019. A comparison of random forest based algorithms: random credal random forest versus oblique random forest. Soft Comput. 23, 10739–10754. https://doi.org/10.1007/S00500-018-3628-5/TABLES/15

Masek, J.G., Wulder, M.A., Markham, B., McCorkel, J., Crawford, C.J., Storey, J., Jenstrom, D.T., 2020. Landsat 9: Empowering open science and applications through continuity. Remote Sens. Environ. 248, 111968. https://doi.org/10.1016/J.RSE.2020.111968

Massari, C., Camici, S., Ciabatta, L., Brocca, L., 2018. Exploiting Satellite-Based Surface Soil Moisture for Flood Forecasting in the Mediterranean Area: State Update Versus Rainfall Correction. Remote Sens. 2018, Vol. 10, Page 292 10, 292. https://doi.org/10.3390/RS10020292

Matsushima, D., Kimura, R., Shinoda, M., 2012. Soil Moisture Estimation Using Thermal Inertia: Potential and Sensitivity to Data Conditions. J. Hydrometeorol. 13, 638–648. https://doi.org/10.1175/JHM-D-10-05024.1

Meza, I., Siebert, S., Döll, P., Kusche, J., Herbert, C., Rezaei, E.E., Nouri, H., Gerdener, H., Popat, E., Frischen, J., Naumann, G., Vogt, J. V., Walz, Y., Sebesvari, Z., Hagenlocher, M., 2020. Global-scale drought risk assessment for agricultural systems. Nat. Hazards Earth Syst. Sci. 20, 695–712. https://doi.org/10.5194/NHESS-20-695-2020

Minet, J., Bogaert, P., Vanclooster, M., Lambot, S., 2012. Validation of ground penetrating radar full-waveform inversion for field scale soil moisture mapping. J. Hydrol. 424–425, 112–123. https://doi.org/10.1016/j.jhydrol.2011.12.034

Misra, G., Cawkwell, F., Wingler, A., 2020. Status of Phenological Research Using Sentinel-2 Data: A Review. Remote Sens. 2020, Vol. 12, Page 2760 12, 2760. https://doi.org/10.3390/RS12172760

Paloscia, S., Pettinato, S., Santi, E., Notarnicola, C., Pasolli, L., Reppucci, A., 2013. Soil moisture mapping using Sentinel-1 images: Algorithm and preliminary validation. Remote Sens. Environ. 134, 234–248. https://doi.org/10.1016/J.RSE.2013.02.027

Pandit, A., Sawant, S., Mohite, J., Pappula, S., 2022. A data-driven approach for bare surface soil moisture estimation using Sentinel-1 SAR data and ground observations. Geocarto Int. 37, 1919–1948. https://doi.org/10.1080/10106049.2020.1805028

Pauwels, V.R.N., De Lannoy, G.J.M., 2006. Improvement of Modeled Soil Wetness Conditions and Turbulent Fluxes through the Assimilation of Observed Discharge. J. Hydrometeorol. 7, 458–477. https://doi.org/10.1175/JHM490.1

Przeździecki, K., Zawadzki, J.J., Urbaniak, M., Ziemblińska, K., Miatkowski, Z., 2023. Using temporal variability of land surface temperature and normalized vegetation index to estimate soil moisture condition on forest areas by means of remote sensing. Ecol. Indic. 148, 110088. https://doi.org/10.1016/J.ECOLIND.2023.110088

Quintana, J.R., Martín-Sanz, J.P., Valverde-Asenjo, I., Molina, J.A., 2023. Drought differently destabilizes soil structure in a chronosequence of abandoned agricultural lands. CATENA 222, 106871. https://doi.org/10.1016/J.CATENA.2022.106871

Rahimzadeh-Bajgiran, P., Omasa, K., Shimizu, Y., 2011. Comparative evaluation of the Vegetation Dryness Index (VDI), the Temperature Vegetation Dryness Index (TVDI) and the improved TVDI (iTVDI) for water stress detection in semi-arid regions of Iran. https://doi.org/10.1016/j.isprsjprs.2011.10.009

Rawat, K.S., Sehgal, V.K., Singh, S.K., Ray, S.S., 2022. Soil moisture estimation using triangular method at higher resolution from MODIS products. Phys. Chem. Earth, Parts A/B/C 126, 103051. https://doi.org/10.1016/J.PCE.2021.103051

Robinson, D.A., Campbell, C.S., Hopmans, J.W., Hornbuckle, B.K., Jones, S.B., Knight, R., Ogden, F., Selker, J., Wendroth, O., 2008. Soil Moisture Measurement for Ecological and Hydrological Watershed-Scale Observatories: A Review. Vadose Zo. J. 7, 358–389. https://doi.org/10.2136/VZJ2007.0143

Rousseeuw, P.J., Hubert, M., 2018. Anomaly detection by robust statistics. Wiley Interdiscip. Rev. Data Min. Knowl. Discov. 8, e1236. https://doi.org/10.1002/WIDM.1236

Sandholt, I., Rasmussen, K., Andersen, J., 2002. A simple interpretation of the surface temperature/vegetation index space for assessment of surface moisture status. Remote Sens. Environ. 79, 213–224. https://doi.org/10.1016/S0034-4257(01)00274-7

Santi, E., Dabboor, M., Pettinato, S., Paloscia, S., 2019. Combining Machine Learning and Compact Polarimetry for Estimating Soil Moisture from C-Band SAR Data. Remote Sens. 2019, Vol. 11, Page 2451 11, 2451. https://doi.org/10.3390/RS11202451

Schober, P., Schwarte, L.A., 2018. Correlation coefficients: Appropriate use and interpretation. Anesth. Analg. 126, 1763–1768. https://doi.org/10.1213/ANE.0000000000002864

Scipal, K., Drusch, M., Wagner, W., 2008. Assimilation of a ERS scatterometer derived soil moisture index in the ECMWF numerical weather prediction system. Adv. Water Resour. 31, 1101–1112. https://doi.org/10.1016/J.ADVWATRES.2008.04.013

Seneviratne, S.I., Corti, T., Davin, E.L., Hirschi, M., Jaeger, E.B., Lehner, I., Orlowsky, B., Teuling, A.J., 2010. Investigating soil moisture–climate interactions in a changing climate: A review. Earth-Science Rev. 99, 125–161. https://doi.org/10.1016/J.EARSCIREV.2010.02.004

Shi, J., Wang, J., Hsu, A.Y., O'Neill, P.E., Engman, E.T., 1997. Estimation of bare surface soil moisture and surface roughness parameter using L-band SAR image data. IEEE Trans. Geosci. Remote Sens. 35, 1254–1266. https://doi.org/10.1109/36.628792

Singh, A., Gaurav, K., Sonkar, G.K., Lee, C.C., 2023. Strategies to Measure Soil Moisture Using Traditional Methods, Automated Sensors, Remote Sensing, and Machine Learning Techniques: Review, Bibliometric Analysis, Applications, Research Findings, and Future Directions. IEEE Access 11, 13605–13635. https://doi.org/10.1109/ACCESS.2023.3243635

SPW Agriculture, R.N. et E., 2023. Observatoire du Foncier Agricole Wallon - Rapport 2023.

Stisen, S., Sandholt, I., Nørgaard, A., Fensholt, R., Jensen, K.H., 2008. Combining the triangle method with thermal inertia to estimate regional evapotranspiration — Applied to MSG-SEVIRI data in the Senegal River basin. Remote Sens. Environ. 112, 1242–1255. https://doi.org/10.1016/J.RSE.2007.08.013

Susha Lekshmi, S.U., Singh, D.N., Shojaei Baghini, M., 2014. A critical review of soil moisture measurement. Measurement 54, 92–105. https://doi.org/10.1016/J.MEASUREMENT.2014.04.007

Tang, R., Li, Z.L., Tang, B., 2010. An application of the Ts–VI triangle method with enhanced edges determination for evapotranspiration estimation from MODIS data in arid and semi-arid regions: Implementation and validation. Remote Sens. Environ. 114, 540–551. https://doi.org/10.1016/J.RSE.2009.10.012

Tao, L., Ryu, D., Western, A., Boyd, D., 2020. A New Drought Index for Soil Moisture Monitoring Based on MPDI-NDVI Trapezoid Space Using MODIS Data. Remote Sens. 2021, Vol. 13, Page 122 13, 122. https://doi.org/10.3390/RS13010122

Touzi, R., 2016. Polarimetric target scattering decomposition: A review. Int. Geosci. Remote Sens. Symp. 2016-November, 5658–5661. https://doi.org/10.1109/IGARSS.2016.7730478

Tromp-van Meerveld, H.J., McDonnell, J.J., 2006. On the interrelations between topography, soil depth, soil moisture, transpiration rates and species distribution at the hillslope scale. Adv. Water Resour. 29, 293–310. https://doi.org/10.1016/J.ADVWATRES.2005.02.016

Tsang, L., Liao, T.H., Gao, R., Xu, H., Gu, W., Zhu, J., 2022. Theory of Microwave Remote Sensing of Vegetation Effects, SoOp and Rough Soil Surface Backscattering. Remote Sens. 2022, Vol. 14, Page 3640 14, 3640. https://doi.org/10.3390/RS14153640

Visser, O., Sippel, S.R., Thiemann, L., 2021. Imprecision farming? Examining the (in)accuracy and risks of digital agriculture. J. Rural Stud. 86, 623–632. https://doi.org/10.1016/J.JRURSTUD.2021.07.024

Vreugdenhil, M., Wagner, W., Bauer-Marschallinger, B., Pfeil, I., Teubner, I., Rüdiger, C., Strauss, P., 2018. Sensitivity of Sentinel-1 Backscatter to Vegetation Dynamics: An Austrian Case Study. Remote Sens. 2018, Vol. 10, Page 1396 10, 1396. https://doi.org/10.3390/RS10091396

Wagner, W., Noll, J., Borgeaud, M., Rott, H., 1999. Monitoring soil moisture over the canadian prairies with the ERS scatterometer. IEEE Trans. Geosci. Remote Sens. 37, 206–216. https://doi.org/10.1109/36.739155

Walker, J.P., Willgoose, G.R., Kalma, J.D., 2004. In situ measurement of soil moisture: a comparison of techniques.

J. Hydrol. 293, 85–99. https://doi.org/10.1016/J.JHYDROL.2004.01.008

Wallonie Service Public SPW, 2023. Rapport d'activités 2023.

Wang, C., Qi, S., Niu, Z., Wang, J., 2004. Evaluating soil moisture status in China using the temperature–vegetation dryness index (TVDI). Can. J. Remote Sens. 30, 671–679. https://doi.org/10.5589/M04-029

Wu, K., Rodriguez, G.A., Zajc, M., Jacquemin, E., Clément, M., De Coster, A., Lambot, S., 2019. A new drone-borne GPR for soil moisture mapping. Remote Sens. Environ. 235, 111456. https://doi.org/10.1016/j.rse.2019.111456

Zhang, D., Zhou, G., 2016. Estimation of Soil Moisture from Optical and Thermal Remote Sensing: A Review. Sensors 2016, Vol. 16, Page 1308 16, 1308. https://doi.org/10.3390/S16081308

Zribi, M., André, C., Decharme, B., 2008. A method for soil moisture estimation in Western Africa based on the ERS scatterometer. IEEE Trans. Geosci. Remote Sens. 46, 438–448. https://doi.org/10.1109/TGRS.2007.904582

Appendix

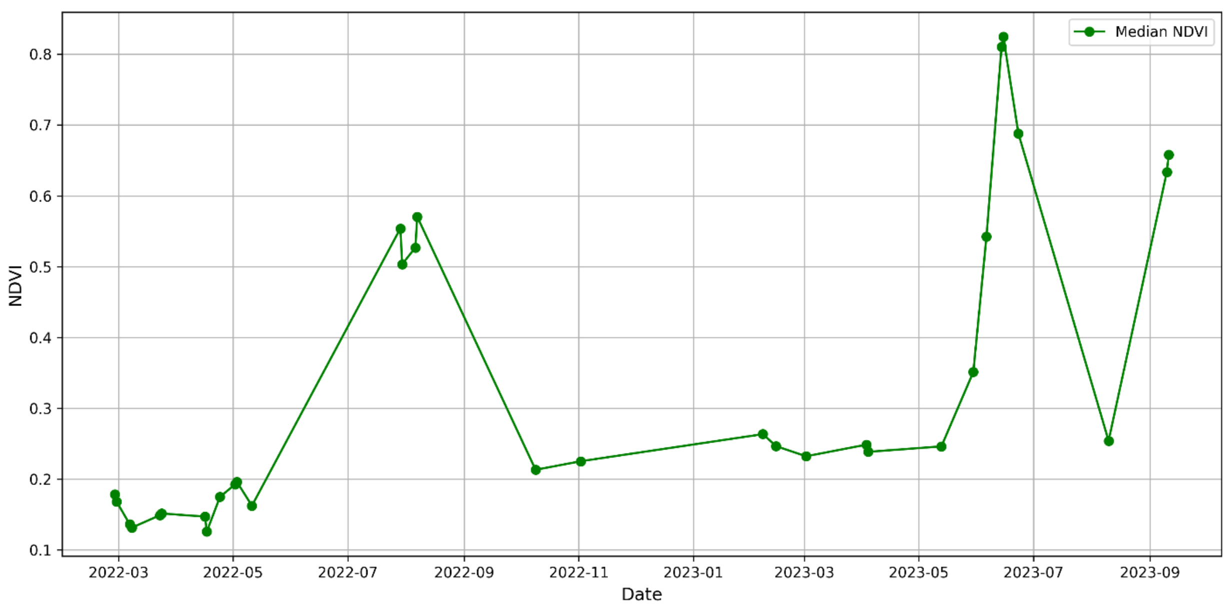

Figure 25: Time series of median NDVI from March 2022 to September 2023. The graph presents the median NDVI values over time, from March 2022 to September 2023. The green line with circular markers shows the temporal variation in NDVI, indicating changes in vegetation health and density. Peaks in the graph correspond to periods of higher vegetation activity, while troughs indicate lower vegetation activity.

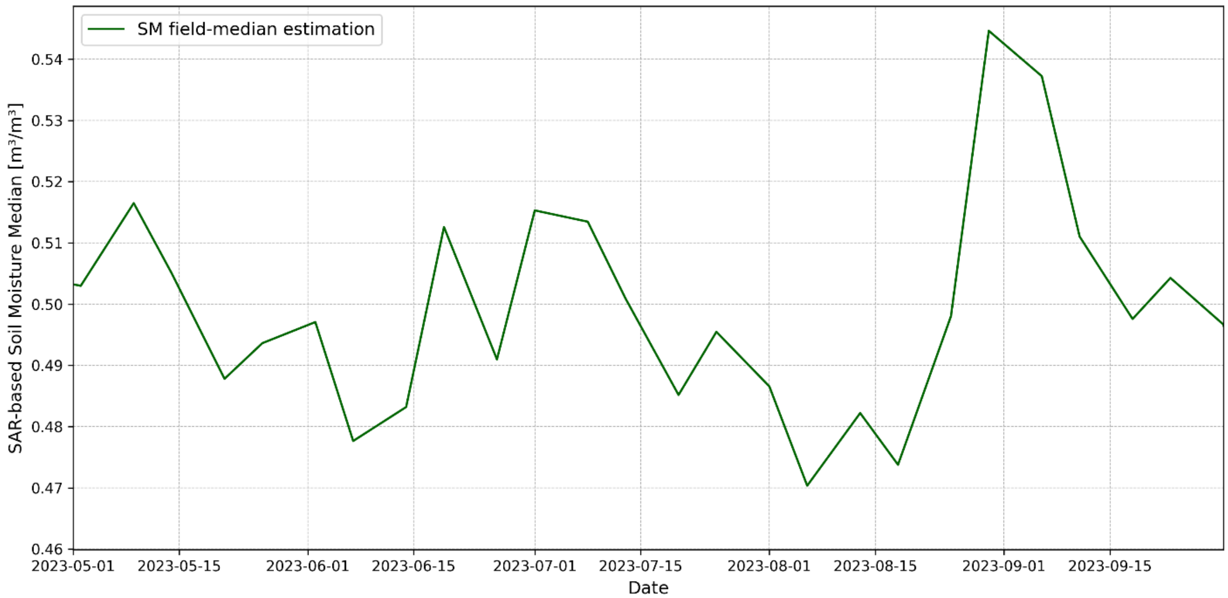

Figure 26: Time series of SAR-based soil moisture median estimation from May 2023 to September 2023. The graph shows the volumetric field-median soil moisture estimation obtained using SAR from May 2023 to September 2023. The green line indicates the temporal variation in soil moisture levels, highlighting fluctuations and trends over the period. Notable peaks and troughs reflect changes in soil moisture conditions influenced by environmental factors.

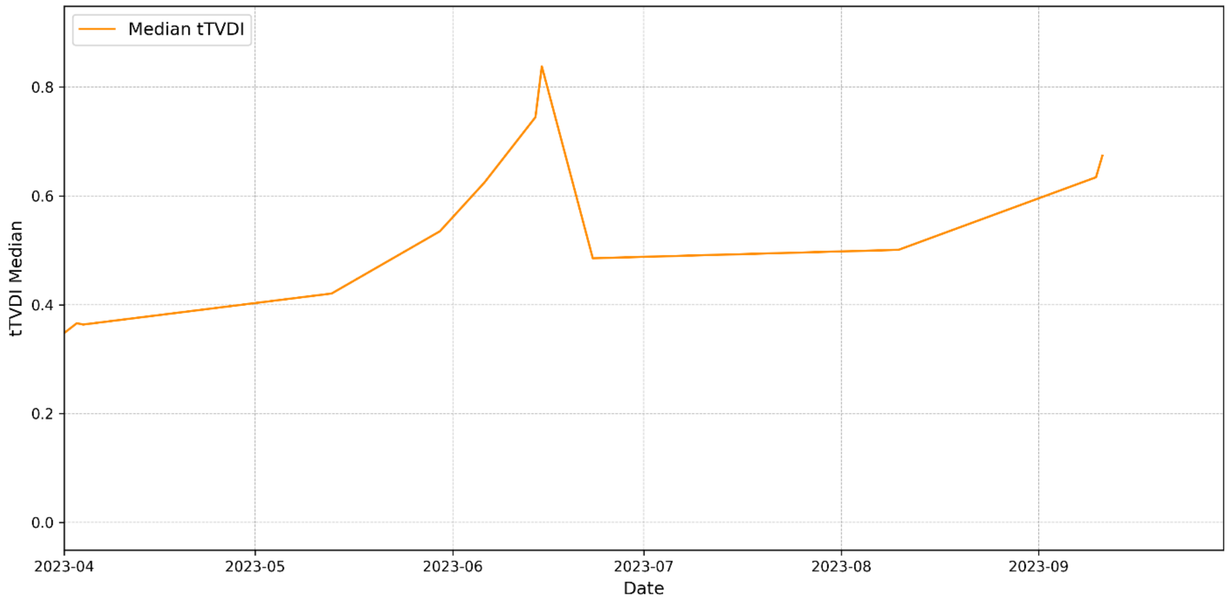

Figure 27: Time series of median tTVDI from April 2023 to September 2023. The graph presents the median tTVDI values over time, from April 2023 to September 2023. The orange line shows the temporal variation in tTVDI, indicating changes in vegetation dryness. Peaks in the graph correspond to periods of higher dryness, while troughs indicate periods of lower dryness.

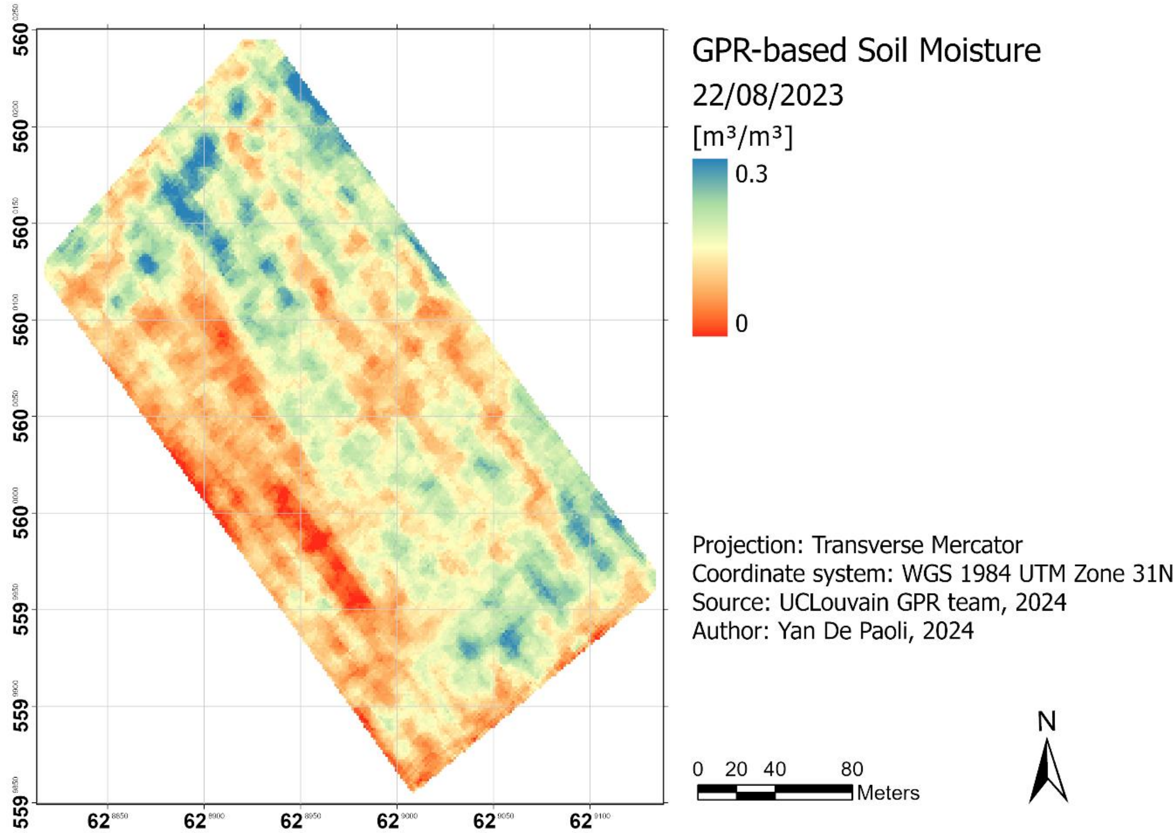

Figure 28: GPR-based soil moisture estimation obtained with kriging interpolation results and at 1.3-meter spatial resolution on August 22, 2023. The map shows volumetric soil moisture estimations created by UCLouvain GPR team. The color scale ranges from 0 to 0.3

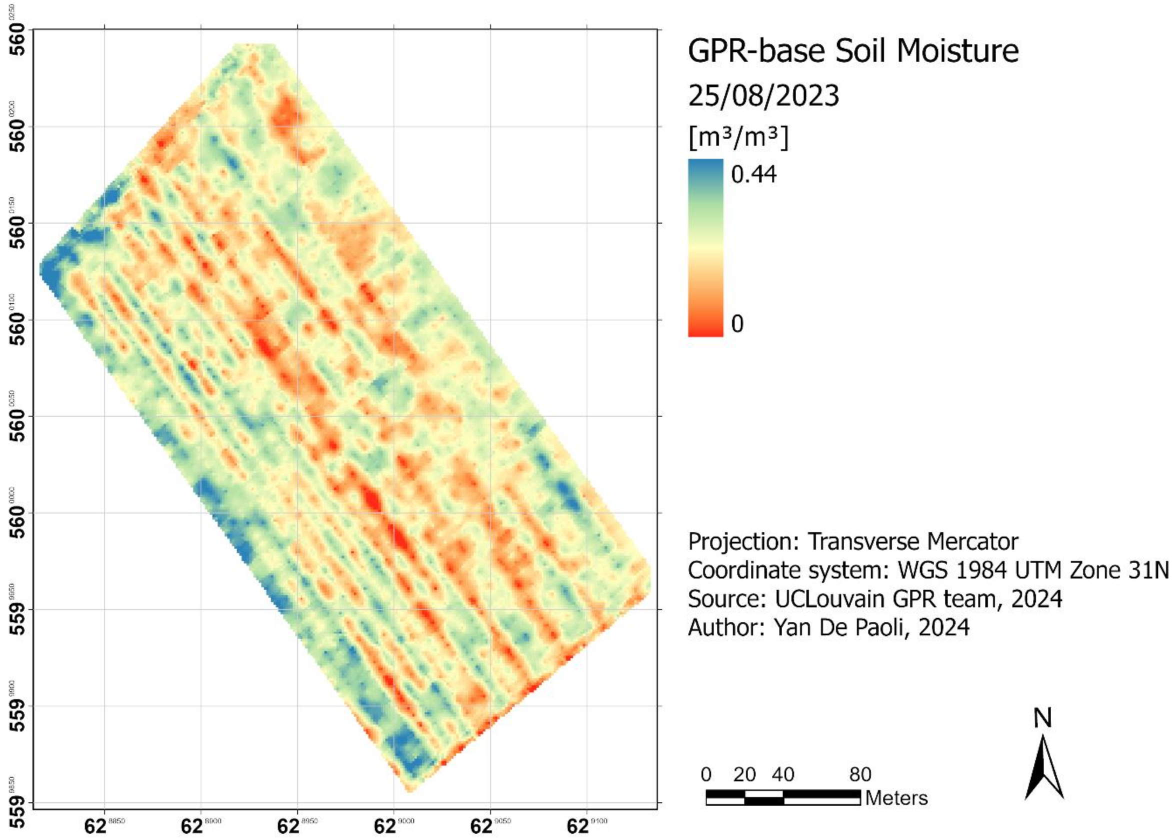

Figure 29: GPR-based soil moisture estimation obtained with kriging interpolation results and at 1.3-meter spatial resolution on August 25, 2023. The map shows volumetric soil moisture estimations created by UCLouvain GPR team. The color scale ranges from 0 to 0.44.

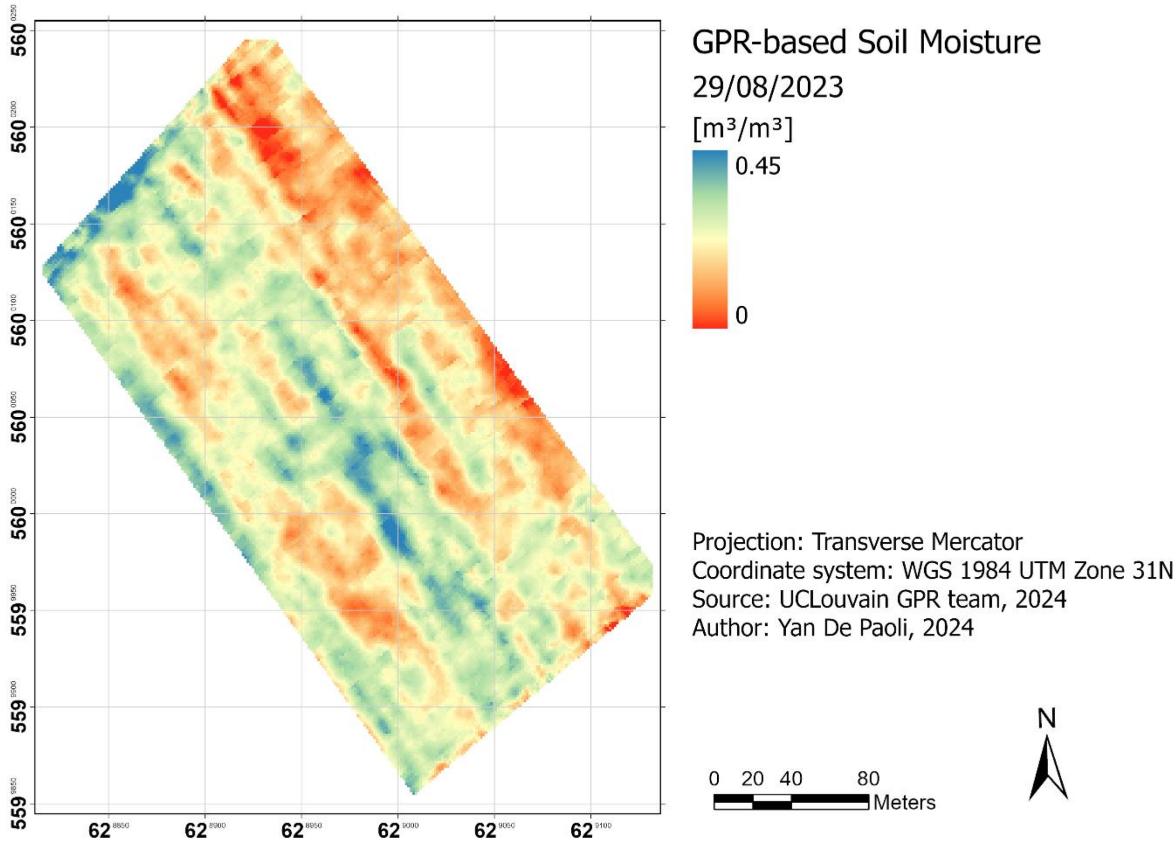

Figure 30: GPR-based soil moisture estimation obtained with kriging interpolation results and at 1.3-meter spatial resolution on August 29, 2023. The map shows volumetric soil moisture estimations created by UCLouvain GPR team. The color scale ranges from 0 to 0.45.

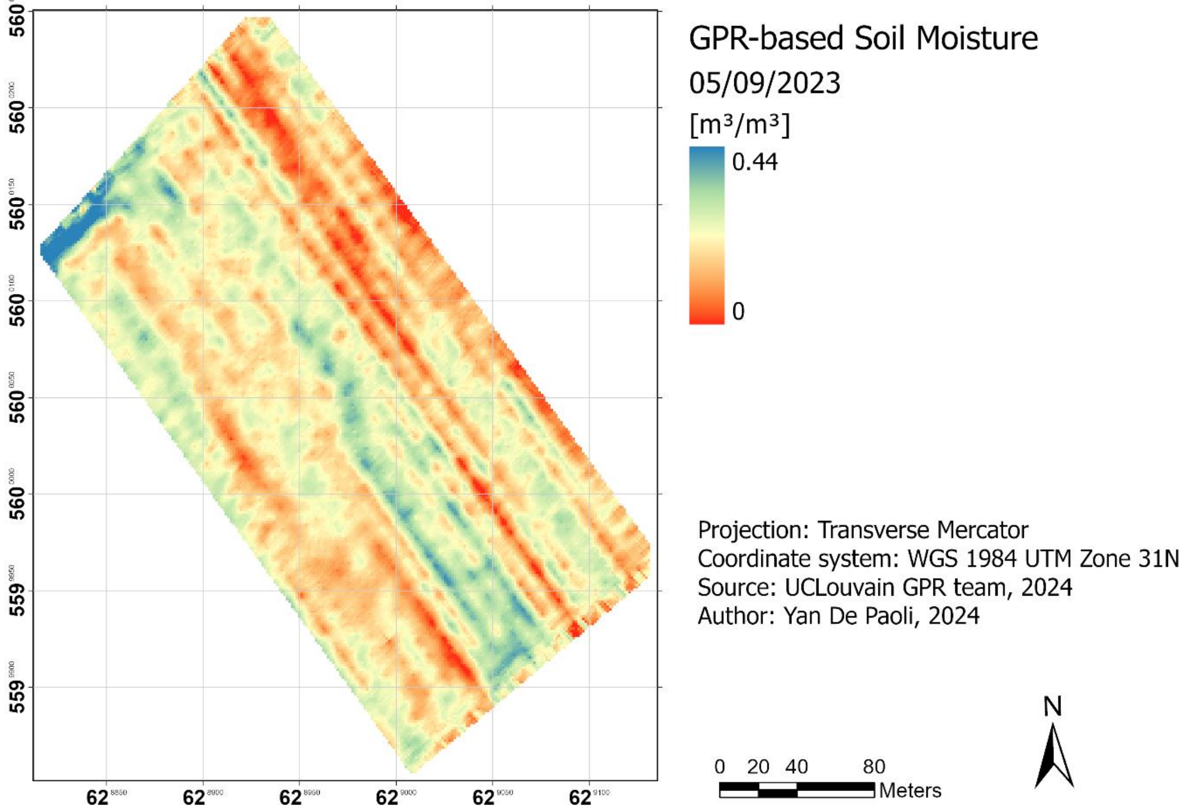

Figure 31: GPR-based soil moisture estimation obtained with kriging interpolation results and at 1.3-meter spatial resolution on September 05, 2023. The map shows volumetric soil moisture estimations created by UCLouvain GPR team. The color scale ranges from 0 to 0.44.

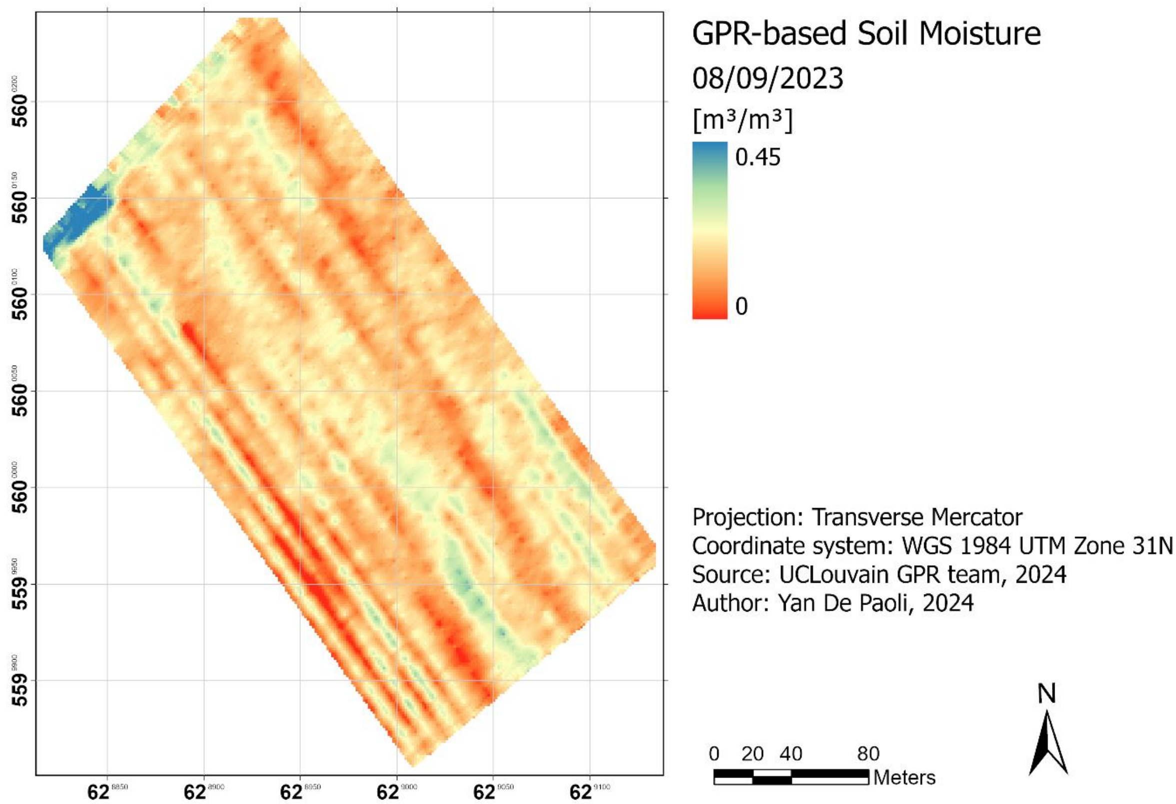

Figure 32: GPR-based soil moisture estimation obtained with kriging interpolation results and at 1.3-meter spatial resolution on September 08, 2023. The map shows volumetric soil moisture estimations created by UCLouvain GPR team. The color scale ranges from 0 to 0.45.

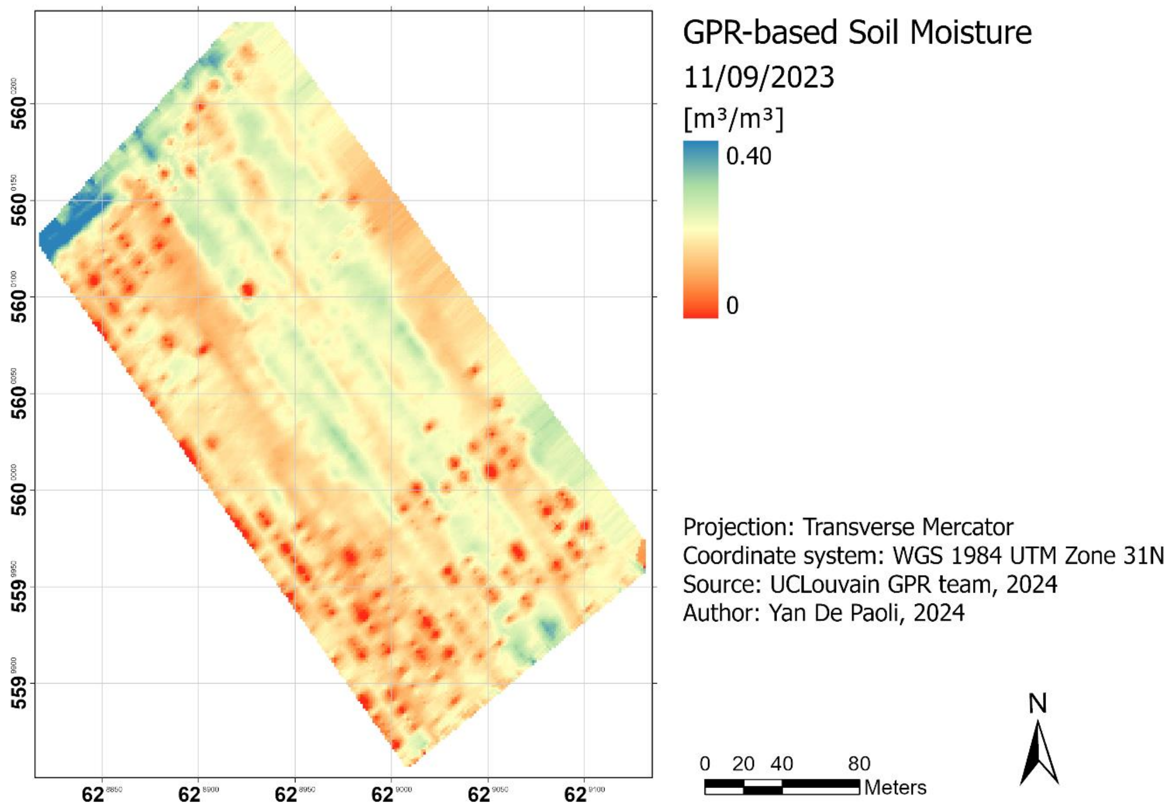

Figure 33: GPR-based soil moisture estimation obtained with kriging interpolation results and at 1.3-meter spatial resolution on September 11, 2023. The map shows volumetric soil moisture estimations created by UCLouvain GPR team. The color scale ranges from 0 to 0.40.

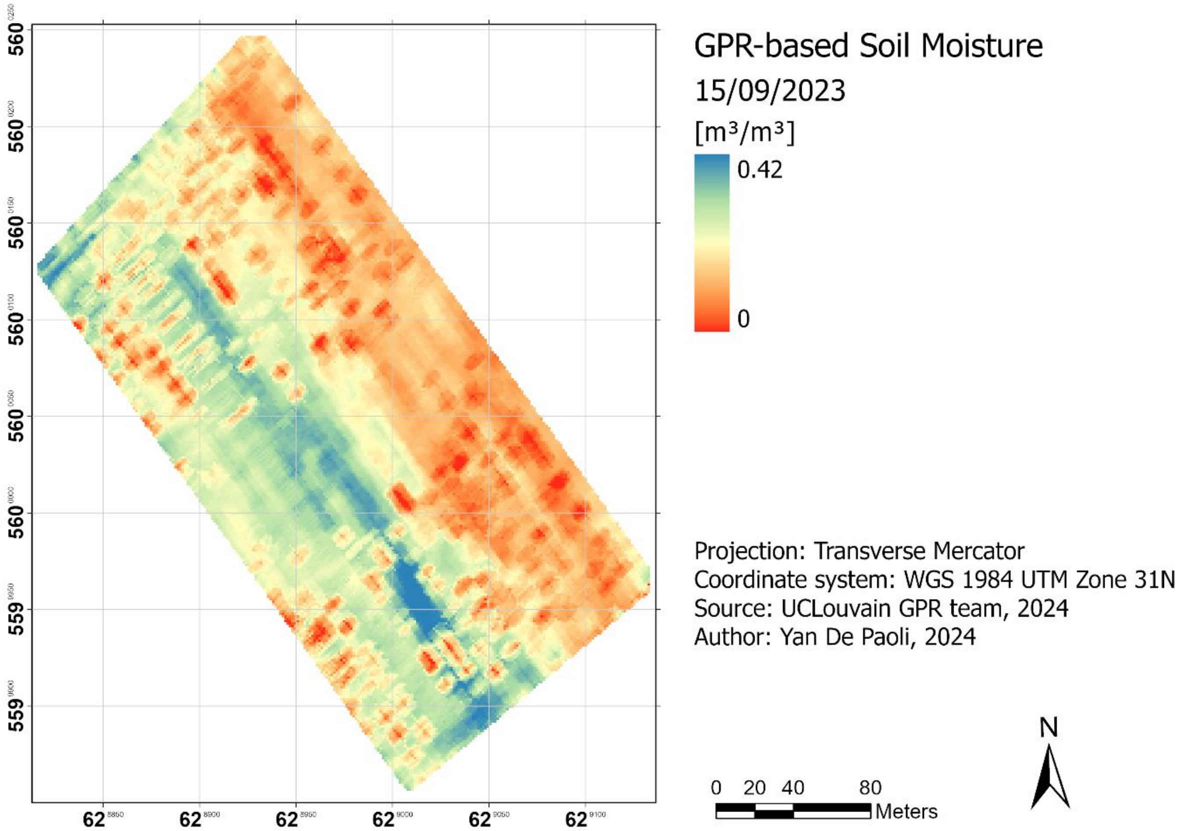

Figure 34: GPR-based soil moisture estimation obtained with kriging interpolation results and at 1.3-meter spatial resolution on September 15, 2023. The map shows volumetric soil moisture estimations created by UCLouvain GPR team. The color scale ranges from 0 to 0.42.

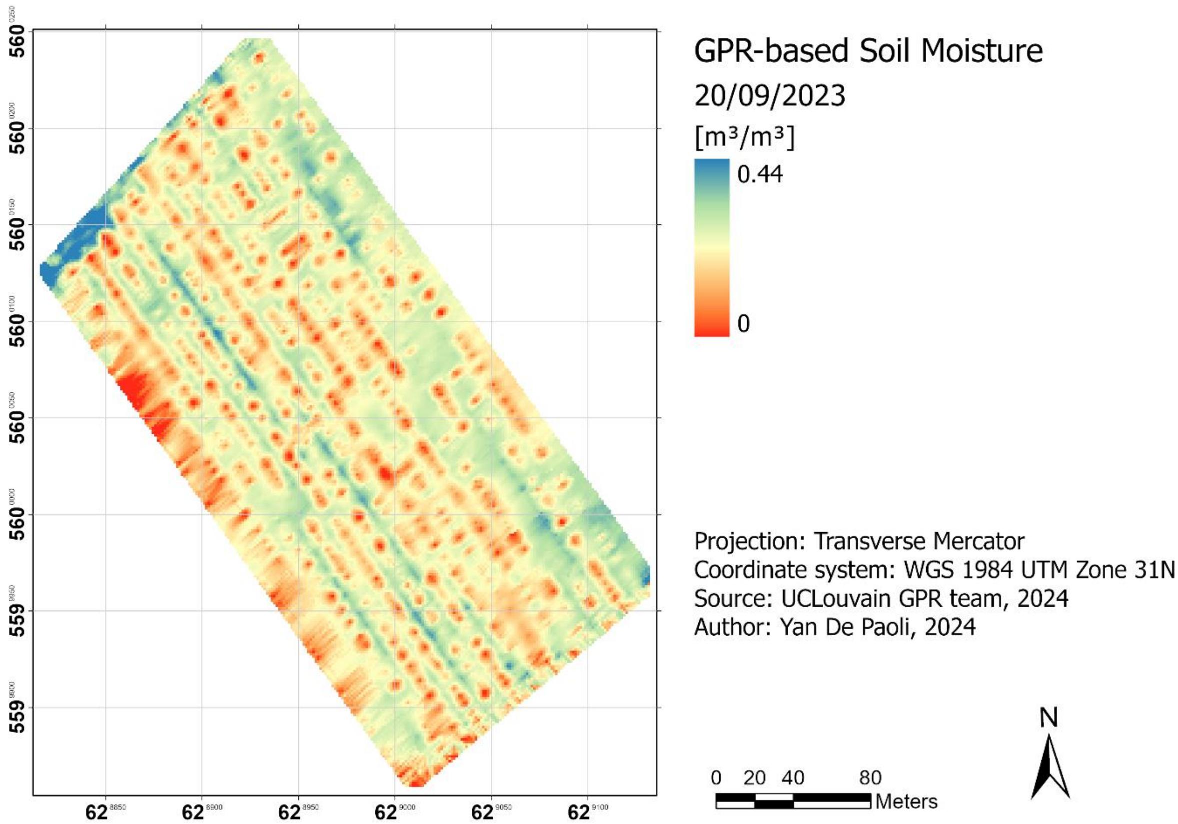

Figure 35: GPR-based soil moisture estimation obtained with kriging interpolation results and at 1.3-meter spatial resolution on September 20, 2023. The map shows volumetric soil moisture estimations created by UCLouvain GPR team. The color scale ranges from 0 to 0.44.

Soil Moisture Estimation: A Comparative Analysis of Remote Sensing Methods Using Ground Penetrating Radar

Yan Cesar Lima Ferro De Paoli

Accurately estimating soil moisture is essential for effective water resource management, crop production, and environmental monitoring, especially in the context of climate change and increasing drought conditions. This study evaluates the qualitative performance of two approaches to access soil moisture information, using Synthetic Aperture Radar (SAR) data and optical/thermal data sources. Specifically, a SAR-based change detection and the Temperature-Vegetation Dryness Index (TVDI) are selected and benchmarked against Ground Penetrating Radar (GPR)-based estimations, which are known for their high spatial resolution. The research is conducted on the Grand Villers field, part of the DuraTechFarm project in Wallonia, Belgium, with GPR measurements taken between August and September 2023. Additionally, a two-year comparison (2022-2023) between the SAR-based and TVDI methods is performed. The findings reveal a strong correlation (75.86%) between recent precipitation events (within the last two days) and high values estimated by the SAR-based approach. For the TVDI, 92.86% of high values correspond to the absence of rainfall within the last two days. When comparing the SAR-based with the GPR-based estimation, a good alignment between them is observed, with a Spearman correlation of 0.78 and a p-value of 0.02. In terms of spatial distribution, both TVDI and GPR-based results indicate similar patterns, showing a concentration of moisture in the center of the field on September 11th. This study highlights the challenges of validating satellite-based soil moisture estimations and underscores the need for more high-resolution, time-continuous measurements to bridge the gap between remote sensing data and ground truth.

UNIVERSITE CATHOLIQUE DE LOUVAIN

Faculté des bioingénieurs

Croix du Sud, 2bte L7.05.01, 1348 Louvain-La-Neuve, Belgique | www.uclouvain.be/agro